# Information Fusion of Magnetic Resonance Images and Mammographic Scans for Improved Diagnostic Management of Breast Cancer

by

Hossein Soleimani

A thesis
presented to the University of Waterloo
in fulfillment of the
thesis requirement for the degree of
Doctor of Philosophy
in
Electrical Engineering

Waterloo, Ontario, Canada, 2021

**Examining Committee Membership**

The following served on the Examining Committee for this thesis. The decision of the Examining Committee is by majority vote.

| | |
|---|---|
| External Examiner: | Javad Alirezaie<br>Professor<br>Dept. of Electrical, Computer, and Biomedical Engineering<br>Ryerson University |
| Internal-External Member: | Giang Tran<br>Assistance Professor<br>Dept. of Applied Mathematics<br>University of Waterloo |
| Internal Member: | Zhou Wang<br>Professor<br>Dept. of Electrical & Computer Engineering<br>University of Toronto |
| Internal Member: | William Bishop<br>Continuing Lecturer<br>Dept. of Electrical & Computer Engineering<br>University of Waterloo |
| Supervisor(s): | Oleg V. Michailovich<br>Associated Professor<br>Dept. of Electrical & Computer Engineering<br>University of Waterloo |

I hereby declare that I am the sole author of this thesis. This is a true copy of the thesis, including any required final revisions, as accepted by my examiners.

I understand that my thesis may be made electronically available to the public.

**Abstract**

Medical imaging is critical to non-invasive diagnosis and treatment of a wide spectrum of medical conditions. However, different modalities of medical imaging employ/apply different contrast mechanisms and, consequently, provide different depictions of bodily anatomy. As a result, there is a frequent problem where the same pathology can be detected by one type of medical imaging while being missed by others. This problem brings forward the importance of the development of image processing tools for integrating the information provided by different imaging modalities via the process of *information fusion*. One particularly important example of clinical application of such tools is in the diagnostic management of breast cancer, which is a prevailing cause of cancer-related mortality in women. Currently, the diagnosis of breast cancer relies mainly on X-ray mammography and Magnetic Resonance Imaging (MRI), which are both important throughout different stages of detection, localization, and treatment of the disease. The sensitivity of mammography, however, is known to be limited in the case of relatively dense breasts, while contrast-enhanced MRI tends to yield frequent "false alarms" due to its high sensitivity. Given this situation, it is critical to find reliable ways of fusing the mammography and MRI scans in order to improve the sensitivity of the former while boosting the specificity of the latter.

Unfortunately, fusing the above types of medical images is known to be a difficult computational problem. Indeed, while MRI scans are usually volumetric (i.e., 3-D), digital mammograms are always planar (2-D). Moreover, mammograms are invariably acquired under the force of compression paddles, thus making the breast anatomy undergo sizeable deformations. In the case of MRI, on the other hand, the breast is rarely constrained and imaged in a pendulous state. Finally, X-ray mammography and MRI exploit two completely different physical mechanisms, which produce distinct diagnostic contrasts which are related in a non-trivial way. Under such conditions, the success of information fusion depends on one's ability to establish spatial correspondences between mammograms and their related MRI volumes in a cross-modal cross-dimensional (CMCD) setting in the presence of spatial deformations (+SD). Solving the problem of information fusion in the CMCD+SD setting is a very challenging analytical/computational problem, still in need of efficient solutions.

In the literature, there is a lack of a generic and consistent solution to the problem of fusing mammograms and breast MRIs and using their complementary information. Most of the existing MRI to mammogram registration techniques are based on a biomechanical approach which builds a specific model for each patient to simulate the effect of mammographic compression. The biomechanical model is not optimal as it ignores the common characteristics of breast deformation across different cases. Breast deformation is essen-

tially the planarization of a 3-D volume between two paddles, which is common in all patients. Regardless of the size, shape, or internal configuration of the breast tissue, one can predict the major part of the deformation only by considering the geometry of the breast tissue. In contrast with complex standard methods relying on patient-specific biomechanical modeling, we developed a new and relatively simple approach to estimate the deformation and find the correspondences. We consider the total deformation to consist of two components: a large-magnitude *global* deformation due to mammographic compression and a residual deformation of relatively smaller amplitude. We propose a much simpler way of predicting the global deformation which compares favorably to FEM in terms of its accuracy. The residual deformation, on the other hand, is recovered in a variational framework using an elastic transformation model.

The proposed algorithm provides us with a computational pipeline that takes breast MRIs and mammograms as inputs and returns the spatial transformation which establishes the correspondences between them. This spatial transformation can be applied in different applications, e.g., producing "MRI-enhanced" mammograms (which is capable of improving the quality of surgical care) and correlating between different types of mammograms. We investigate the performance of our proposed pipeline on the application of enhancing mammograms by means of MRIs and we have shown improvements over the state of the art.

**Acknowledgements**

I would like to thank all the people who made this thesis possible.

First and foremost, I wish to thank my adviser Professor Oleg V. Michailovich whose insight and knowledge into the subject matter steered me through this research. Through more than 1000 emails and many hours of meetings over the four years, Oleg taught me the fundamentals of good research, writing, and presentation. He provided me with the full freedom to explore research topics that both of us would be interested in. It has been a privilege working with him. I am also honored to have Professor Javad Alirezaie, Professor Zhou Wang, Professor Gian Tran, and William D. Bishop on my thesis committee.

In our lab, I've had the opportunity to work with many amazing labmates. These include Rinat, Rui, Jose, Amir and George. I am also grateful to my dear friends and housemate including Hamid, Daniel, Amir, Ali and Milad. From the bottom of my heart, I thank every single one of you, if not for which, this thesis would never have been complete.

Last but not least, I would like to thank my parents and siblings, for their love and support.

## Dedication

For my parents, always and forever.
Without you, I'd never have made it.

# Table of Contents

# List of Tables

# List of Figures

# Abbreviations

**2-D** Two Dimensional xii, 2, 6, 12, 13, 17, 20, 21, 30, 31, 33, 37, 43, 66, 71, 86, 102

**3-D** Three Dimensional 2, 5, 6, 9, 11–13, 19, 20, 29, 30, 33, 34, 37, 38, 43, 46, 61, 66, 72, 85, 86, 96, 99, 102

**ACC** Accuracy 26, 55, 56, 129

**ADMM** Alternating Directions Method of Multipliers 131, 132

**CAD** Computer-Aided Diagnosis 29

**CAR** Clip-And-Restore xi, xiv, xv, 75, 78–80, 86, 90, 93–95, 99, 103

**CC** Cranial-Caudal xi, xii, xiv, xv, 7, 8, 12, 15, 27–30, 35, 36, 47, 66, 68, 69, 85, 87–94, 96, 97, 100, 102, 103

**CMCD** Cross Modal Cross Domain 12, 13

**CNN** Convolutional Neural Network xi, xiii, 38, 45, 47, 49–51, 56, 63, 124

**CPD** Coherent Point Drift xiv, 72–74

**CPU** Central Processing Unit 97, 98

**CT** Computerized Tomography xiv, 81

**DCE** Dynamic Contrast-Enhanced 5, 10, 27, 28, 103

**DL** Deep Learning 14, 38, 49, 56, 57, 125

**DSC** Dice Similarity Coefficient xi, 26, 45, 47, 55, 56, 62, 63, 129, 130

**EM** Expectation Maximization 57, 73

**EXR** Emulated" X-ray xi, xiv, xv, 86–95

**FE** Finite Element 32, 33

**FEM** Finite Element Model xi, xii, 31, 32, 34–36, 71, 85, 89, 91, 92, 96, 98–100

**FFD** Free From Deformation xii, xiii, 14, 19, 20, 65, 67, 84, 89

**FFDM** Full-Field Digital Mammography xv, 4, 51, 92

**FN** False Negative 26

**FNR** False Negative Rate xi, 26, 55, 56, 129

**FP** False Positive 26

**FPR** False Positive Rate xi, 26, 55, 56, 129

**GMM** Gaussian Mixture Model xiii, 57, 61, 62, 72

**GPU** Graphics Processing Unit 47, 98

**HED** Hierarchical Edge Detection 49, 50

**JAC** Jaccard Coefficient 26, 55, 56, 129, 130

**JE** Joint Entropy 22, 23

**JPDF** Joint Probability Distribution Function 23

**LSA** Left-Anterior-Superior 66

**MI** Mutual Information 23, 24, 82, 86, 90–92, 94, 95

**MLO** Mediolateral-Oblique x–xiii, xv, 7, 8, 12, 15, 27–30, 35–37, 47, 48, 50, 52, 54, 55, 63, 66, 68, 85, 90–97, 100, 102, 103, 124, 128

**MRI** Magnetic Resonance Imaging viii, ix, xii–xv, 2, 4, 5, 8–16, 27, 28, 30–41, 43, 47, 56, 57, 59, 61–70, 72–74, 80, 81, 85–87, 89–93, 95, 96, 99, 100, 102–104, 133

**MRS** Magnetic Resonance Spectroscopy 5

**NCC** Normalized Cross Correlation 22, 35

**NMI** Normalized Mutual Information 23

**NMR** Nuclear Magnetic Resonance 8

**RMM** Rician Mixture Modeling 57

**ROI** Region Of Interest 29

**RPCA** Robust Principal Component Analysis 27

**SD** Spatial Deformation 12, 13

**SDD** Source-Detector Distance 7

**SDF** Signed Distance Function 75

**SEN** Sensitivity xi, 26, 45, 47, 55, 56, 129

**SNR** Signal to Noise Ratio 9, 57, 62–64, 100

**SOD** Source-Object Distance 7

**SPE** Spesificity xi, 26, 45, 47, 55, 56, 129

**SSD** Sum of Squared Difference xv, 22, 24, 82, 86, 90–96, 98, 100

**TDT** Thickness of the Dense Tissue xi, xiv, xv, 86–96, 98, 100

**TN** True Negative 26

**TP** True Positive 26

**TPS** Thin Plate Spline 73, 79

**TRE** Target Registration Error xi, xv, 86, 88, 89, 91, 92, 94–98, 100, 102

# Chapter 1

# Introduction

Breast cancer is the most common malignancy diagnosed in women worldwide. Approximately 1.1 million cases of breast cancer are globally diagnosed each year, with annual fatalities exceeding 400,000 lives worldwide. In Canada, breast cancer accounts for 13% of all cancers[1]. It is the most commonly diagnosed cancer, accounting for 25% of all cancers among female patients. Over the past 25 years, the incidence of breast cancer has essentially increased with associated lifetime diagnosis going from 1-in-12 to 1-in-8, and at the same time the absolute risk of dying from breast cancer has remained somewhat the same [2].

As in the case of many major disorders, early detection has a critical impact on the outcomes of treatment of breast cancer. Accordingly, many diagnostic instruments have been introduced for diagnosing breast disease in its earliest possible stages. Among these tools, medical imaging provides a non-invasive analysis of internal anatomy and pathology. Different imaging modalities provide different presentations of breast tissue. In this way, they often provide physicians with a different source of information which is used differently through clinical treatments.

Due to the complementary nature of the information provided by imaging modalities, it is often useful to fuse them, or equivalently, transfer contrast from one modality to another modality. To fuse the information, one would need to establish spatial correspondences between two images coming from different modalities, which technically can be defined by a geometric transformation between the domains of these two images. Therefore, given two source images, the problem is mainly to estimate this geometric transformation which

[1] 2018 Canadian Cancer Statistics - Canadian Cancer Society: https://www.cancer.ca/en/cancer-information/cancer-101/canadian-cancer-statistics-publication/?region=on

turns out to be a non-trivial problem in the case of images being used in the diagnosis of breast disease. This is mostly due to the different dimensionality and contrast mechanism of the breast imaging modalities. Our goal, in this work, is to transfer contrast from breast Magnetic Resonance Imaging (MRI) to mammography.

The result of our research is a computational pipeline that takes breast MRIs and mammograms as inputs and returns the spatial correspondences between them. This spatial transformation can be used in many applications, but in particular, we are interested in projecting the geometrical locations and shapes of breast lesions detected by MRI to mammography. This helps to reveal cancers which are mammographically occult (not seen in mammograms). But in this case, the former is 3-D while the latter is 2-D, they use different contrast mechanisms, and on top of that, there is also an additional compression component in mammography which makes this problem to be extremely ill-posed. In this work, we propose a practical tool to establish correspondences between the breast MRI and the mammogram, which improves the efficiency over standard methods.

Below, we provide some principles of breast anatomy and mention common breast malignancies. Then we provide basic information on breast MRI and mammography along with briefly mentioning some other breast imaging techniques which are sometimes involved. The chapter is concluded with a formal definition of our research problem, its challenges, as well as our solutions associated with it.

## 1.1 Breast Anatomy

Breast tissue is part of the anatomy which mainly consists of adipose, i.e., fat, and fibroglandular, i.e., dense, tissue. A healthy breast is composed of 12 to 20 compartments called *lobes*. Each of these lobes is made up of several smaller *lobules* which are the glands that produce milk. Both the lobes and lobules are connected by *milk ducts* which gradually converge towards the nipple (see Figure 1.1 for more details). The breast tissue is separated from the ribs by two pectoral muscles. The lobules and the ducts are surrounded with adipose tissue along with other types of supportive structures such as Cooper ligaments which determines the shape of the breast tissue.

Broadly speaking, breast lesions are divided into benign and malignant neoplasm subtypes [58]. For example, the most common types of benign neoplasm are breast cysts. On the other hand, we have malignant neoplasm that combinedly is called breast cancer, which can come in a variety of shapes, sizes and can grow at different parts of the breast tissue. It can also spread outside the breast through blood vessels and lymph vessels, where it is said to have metastasized.

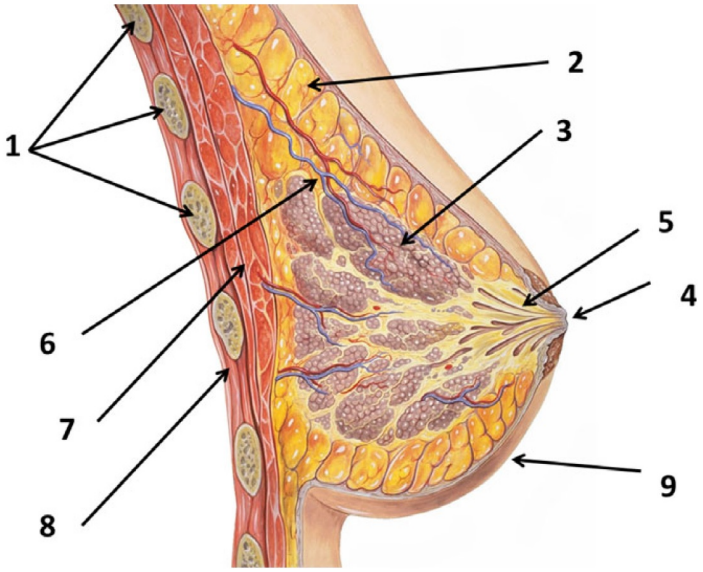


Figure 1.1: Breast anatomy: (1) ribs, (2) adipose tissue, (3) lobules, (4) nipple, (5) lactiferous duct, (6) blood vessels, (7) chest wall, (8) pectoral muscle, and (9) skin [41].

Breast cancer can be categorized as invasive (if it is spread) and non-invasive (if it is not spread) types. In situ breast cancer (ductal carcinoma in situ) is a common example of non-invasive breast cancer which starts and grows in milk ducts. It is the earliest stage (known as stage one) at which breast cancer can be diagnosed. The vast majority of women diagnosed with it can be cured. If it is not diagnosed on time, it can lead to invasive cancer[2]. Invasive breast cancers, which are generally detected in higher stages, are divided into two common groups:

- **Invasive ductal carcinoma**: The cancer cells grow outside the ducts into other parts of the breast tissue. Invasive cancer cells can also spread, or metastasize, to other parts of the body.
- **Invasive lobular carcinoma:** Cancer cells spread from the lobules to the breast tissues that are close by. These invasive cancer cells can also spread to other parts of the body.

There are many risk factors for breast cancer, and cancer might be due to a combination of factors which include age, family history, medical history, genetic information, etc. In

[2]https://www.webmd.com/breast-cancer/guide/ductal-carcinoma-invasive-in-situ

addition to that, there are other quantitative measures of risk such as breast density which is defined as the ratio of fibroglandular tissue to the total breast volume. In particular, it has been shown that higher breast density is strongly related to a higher risk of developing cancer [115]. The proportion of the fibroglandular and fat tissues varies across time as it is affected by hormonal changes, such as childbirth or by the process of involution, which results in time-variant breast density. Therefore, for an individual, risk factors vary by time due to aging, involution process and hormonal changes.

## 1.2 Breast Imaging

The practice of breast imaging has transitioned through a wide variety of technological advances from the early days of direct-exposure film mammography to xeromammography to screen-film mammography to the current era of digital mammography and digital breast tomosynthesis. Besides X-ray, other techniques like MRI and ultrasound have long been the principal imaging modalities used throughout various stages of diagnosis and treatment of breast cancer [16].

In the 1960's, it was common to use X-ray tubes with direct exposure film in breast diagnosis, which was originally designed for other medical imaging procedures such as chest radiography [54]. Later on, the technology developed enough to become safer in terms of exposure to radiation, where an improvement over direct exposure film mammography came in the form of xeroradiography [63]. The major technological advance in mammography came with the development of screen-film (analog) mammography and uniform-thickness breast compression [113]. Since then screen-film mammography has allowed acquiring images in a safer and efficient manner.

X-ray mammography plays a central role in the radiological management of breast cancer. It is used in many clinical workflows for diagnosis, tumor localization as well as prescreening, presurgical planning, and interoperation guidance. For women at average risk, a screening mammogram is normally performed annually (beginning at the age of 50 in Canada) to reveal early signs of breast cancer. For the patients at a higher risk of breast cancer (due to, e.g., family history or genetic predisposition) an early exam is usually warranted. In past decades, conventional analog mammography has been replaced by Full-Filled Digital Mammography (FFDM) in which the X-ray film is replaced by solid-state detectors that convert X-rays into electrical signals. Most radiology practices use digital mammography because compared to analog film, it provides better quality images with improved tissue contrast. Studies have shown that digital mammography is particularly better than film mammography for dense breasts, as well as for younger patients,

who tend to have denser breasts than older patients. Digital mammography also has the added benefit of lower radiation dose compared to traditional analog mammography. In recent years, some prestigious hospitals have opted for tomosynthesis scanning, which is an extension of mammography and allows 3-D reconstruction of the breast based on multiple projections [99]. These three-dimensional image sets help to minimize the tissue overlap that can hide cancers or make it difficult to distinguish normal overlapping breast tissue from tumors [142].

MRI has been utilized for a long time and breast imaging was among the first applications of it. In particular, modern clinical workflows require using a particular version of MRI which is called Dynamic Contrast-Enhanced MRI (DCE-MRI). In this type of MRI, a contrast agent is injected into the subject and images acquired along a timeline providing us with information of how this contrast agent is absorbed by different tissue types (it will be explained later). It provides a 3-D image of the breast tissue and functional information showing the areas in the breast with increased blood flow. This type of imaging removes any ambiguity caused by the projective nature of mammography and also tends to show both malignant and benign lesions which takes a radiologist to sort them by their properties.

There are other methods like ultrasound which is often used as a second look imaging modality to confirm what has been seen before. In addition, it is routinely used for wire localization which is done before breast cancer surgery to find where the breast abnormality is. Since it does not expose the patient to any radiation, ultrasound imaging is safer in comparison to mammography [10]. However, diagnostic information of ultrasound is difficult to interpret due to its relatively low spatial resolution, noise, and contrast.

Another common type of breast imaging is optical molecular modality which uses exogenous fluorescent probes as additional contrast agents that target molecules relevant to breast cancer [43]. By providing detailed pictures of internal structures of the breast at the molecular and cellular level, it creates a potential for early breast cancer detection. Furthermore, it has an application in biopsy where it is utilized to guide a needle to remove a sample of the tissue. Magnetic Resonance Spectroscopy (MRS) is another imaging modality focusing on diagnosis and staging. It indicates biochemical, rather than structural, composition of a lesion[8].

Among all breast imaging modalities, X-ray mammography and MRI remain the main principal medical imaging modalities in breast cancer diagnosis and treatment. In the next section, we describe these imaging modalities in more detail.

### 1.2.1 X-ray Mammography

As it was mentioned in previous sections, X-ray mammography is the gold standard in early detection of breast disease in screening programs. During examination the breast is compressed between two plates, compression paddles, and it is exposed to X-ray radiation. Figure 1.2 shows a schematic representation of the mammographic imaging system. In mammography, the breast tissue is compressed (planarized) which is one of the essentials of effective mammography (and a common source of patient discomfort and concern). Potential benefits derived from breast compression includes: a more uniform breast thickness resulting in a better fit of the exposure into the film latitude or dynamic range, reduced blurring from patient motion, reduced scattered radiation and improved contrast sensitivity, reduced radiation dose, and better visualization of tissues near the chest wall.

As it is seen in Figure 1.2, in addition to compression paddles, there is a source of X-ray radiation (X-ray tube) which is focused on the compressed breast tissue. The produced X-rays pass through the tissue and are absorbed on the film producing a 2-D mammogram. As the X-rays penetrate the breast tissue, they are attenuated by the tissues they have passed. In other words, depending on the attenuation properties of the tissues and their thickness, some energy of each X-rays is absorbed in the path. Note that X-rays are composed of radiations with different energy levels.

Let $I(\mathbf{r})$ be the image intensity at point $\mathbf{r}$ in the 2-D imaging plane, $\mu(\mathbf{r}, z, E)$ be the linear attenuation coefficient of tissue at $(\mathbf{r}, z)$ (in the 3-D domain of the breast), and $h(\mathbf{r})$ be the thickness of the breast tissue at $\mathbf{r}$ and in the direction of mammographic projection. Based on Beer-Lambert's law, $I(\mathbf{r})$ can be defined as follows [158]

$$I(\mathbf{r}) = I_0 \int_{E=0}^{\infty} p(E)^{-\int_{z=0}^{h(\mathbf{r})} \mu(\mathbf{r},z;E)dz} dE \tag{1.1}$$

where $p(E)$ is the normalized photon energy spectrum at energy $E$, and $I_0$ indicates the incident photon energy. The attenuation coefficient of a tissue not only depends on its properties but it also is a function of photon energy $E$, and that is why the integration goes over entire range of energy.

Generally speaking, the contrast in mammograms is due to the different attenuation coefficients of fat and fibroglandular tissues. The attenuation coefficient of fibroglandular tissue is higher than that of adipose tissue, and hence, the former is seen brighter in X-ray images [64]. On the other hand, the attenuation coefficient of any fibroglandular (e.g., ducts, carcinoma, glandular) and tumor are similar and, as a result, they look like each other in X-ray mammography. Consequently, interpreting the mammographic findings in dense breasts is challenging.

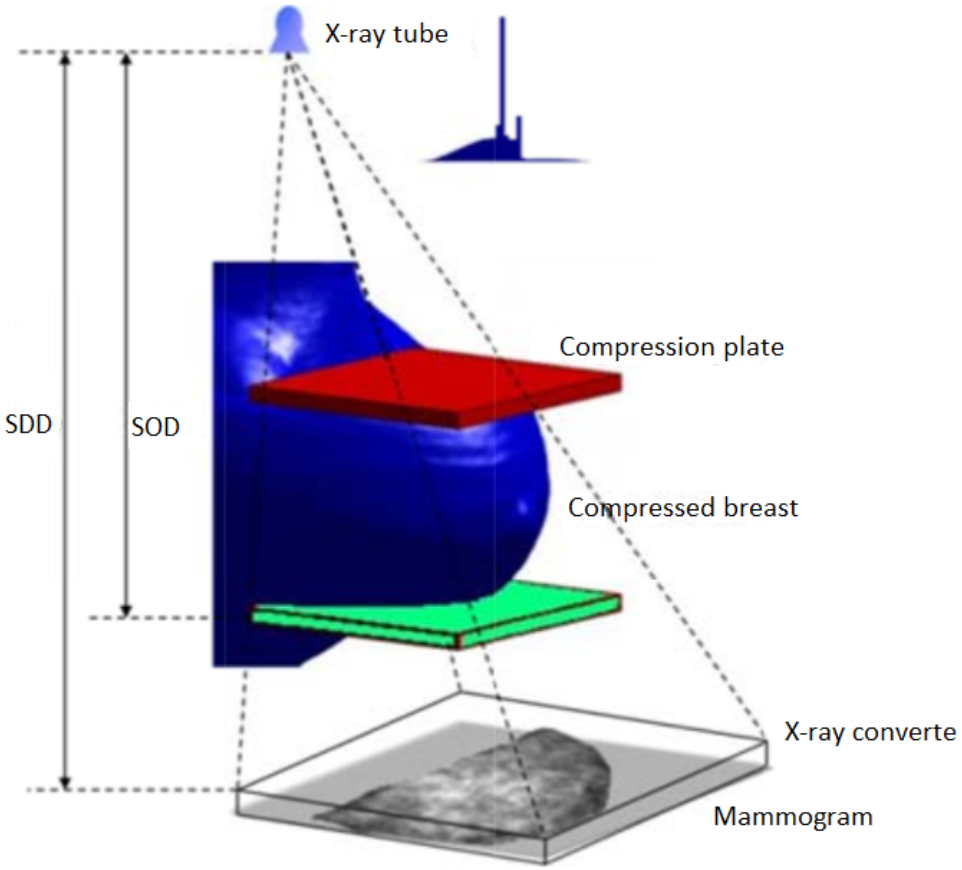


Figure 1.2: X-ray mammography system [131]

In mammography, the position of the patient is defined by two terms: Source-Object Distance (SOD), where the object represents the patient); and Source-Detector Distance (SDD). The distance between two paddles is indicated by "body-thickness" which is relatively much smaller than SOD and SDD. Depending on the direction of breast compression, digital mammograms are standardly acquired in two projected views called Cranial-Caudal (CC) and Mediolateral-Oblique (MLO), examples of which are depicted in Figure 1.3. Another point deserving to be mentioned is that the resolution of X-ray images is typically higher with respect to other modalities.

With all the advantages offered by mammography, it is known to have a lower success rate in certain patients. More specifically, when it goes to radiological breast tissue cate-

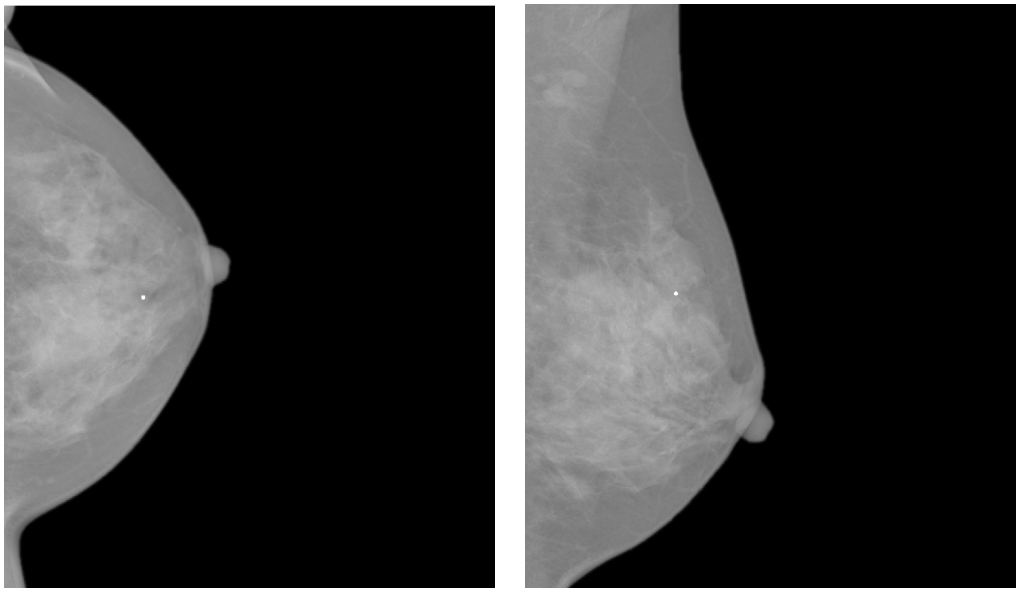

(a) (b)

Figure 1.3: X-ray mammogram: (a) CC view; (b) MLO view

gories known as "extremely dense" and "heterogeneously dense" it fails to reveal malignant lesions. In these cases, lesions are obscured by dense tissues and technically we say lesions are *mammographically occult* [17]. To locate these lesions we use information from MRI, and throughout this thesis, we will call it "MRI-enhanced mammograms". Such application is particularly important in breast surgery to localize multi-centric and multi-focal lesions.

### 1.2.2 Breast MRI Imaging

MRI relies on the phenomenon of Nuclear Magnetic Resonance (NMR) resulting in a spectroscopic technique that we use to obtain physical information about molecules. Although NMR can be applied on a range of nuclei, in MRI, medical MRI targets hydrogen due to the abundance of water molecules in our body. It uses a constant large-amplitude magnetic field (typically around 1.5 to 3 T) to align the spins of the protons in water molecules. Subsequently, using external electromagnetic pulses (time-varying electromagnetic field) the spins are selectively forced to steer from the alignment. Then, by switching off the electromagnetic field, the spins go back to the equilibrium through the process of *precession*. As

the spins return to the alignment with the magnetic field, they emit electromagnetic energy that can be measured. Using the technique of tomographic construction, this emitted electromagnetic energy is processed and used to build 3-D grey-scale MRI images.

The precession is described by two characteristic times, T1 (also called spin-lattice) and T2 (also called spin-spin). In particular, T1 is the time required for the net magnetization vector to realign itself with the constant magnetic field, and T2 is the time required for the signal (produced in the precession process from a given tissue type) to decay. These times are strictly dependent on the properties of the tissue at molecular level. Different tissues, with normal or abnormal states, have different T1 and T2. In the MRI system, the contrast is created by applying different imaging protocols that have been designed to outline the differences in T1, T2, and spin density.

Breast MRI acquisition is standardly performed with women lying on their stomachs, with their face turned down. This anatomical position is referred to as prone (see Figure 1.4a). The prone position makes it possible to place the breast as close as possible of an array of MRI receiving antennas. It is not only to increase the Signal-to-Noise Ratio (SNR), but also to reduce the frequency and phase contributions from tissues other than the breast [49]. Moreover, the uncompressed and pendulous state of the breast tissue helps to avoid tissue folding, thus further maximizing the accuracy of detection and localization of breast lesions. In comparison to mammography, MRI exhibits coarser resolution with typical voxel size of $0.7\,\text{mm} \times 0.7\,\text{mm} \times 2\,\text{mm}$. Figure 1.4b illustrates a typical axial slice

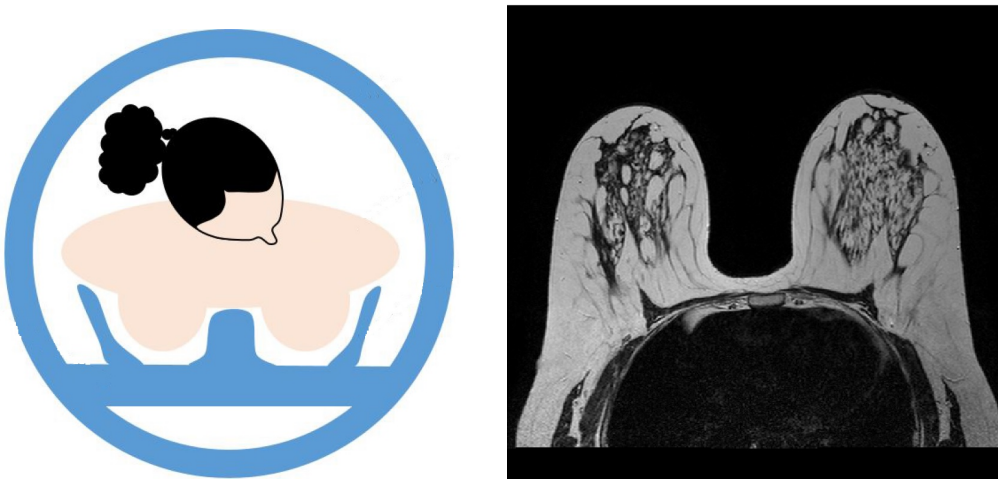

(a) (b)

Figure 1.4: (a) Prone position during MRI [131]; (b) pre-contrast (axial slice) MRI slice

from a T1-weighted breast MRI .

Unfortunately, the quality of MRI image declines due to the differences between resonance frequencies of fat and water, chemical-shift effect, etc. This issue is of a particular concern in breast imaging where most part of the breast is composed of fat. To solve this, DCE-MRI in which multiphase MRI scans are taken following the intravenous injection of a contrast agent, gadolinium$^{TM}$ in most cases, has been widely used in clinical practice. These agents change the relaxation times of tissues. In the tumor neighborhood, the vascular system is larger in comparison to other regions causing the accumulation of blood, or equivalently water, in the area. Therefore, in vicinity of the lesions, the relaxation time will change dramatically with respect to the other part of the breast tissue. By taking more images as the agent passes through the vascular system and computing some parameters from these images, radiologists are able to locate the tumor [71]. Also by having several post-contrast MRI images and subtracting the pre-contrast image from them, it becomes possible to track changes at each region of the image, and consequently recognize any abnormality in the breast tissue.

Thanks to the possibility of visualizing three-dimensional dynamic information and its high sensitivity, the DCE-MRI has demonstrated a great potential for screening high-risk women and staging newly diagnosed breast cancers. Therefore, DCE-MRI is becoming more popular as an important tool for breast cancer diagnosis. In addition, DCE-MRI sequences are used to extract the washout pattern of the contrast agent. Washout is defined as a visually assessed temporal reduction in enhancement relative to the surrounding liver from an earlier to a later phase [24]. By plotting the MR signal of a region of interest over time, it is possible to distinguish between a tumor and healthy tissue. Malignant lesions usually show early enhancement with rapid washout, whereas benign lesions typically show a increase followed by persistent enhancement [62].

Despite many advantages offered by breast MRI, it shows a higher rate of false-positive or a small value of specificity. In other words, it detects all benign and malignant at the same time which may lead to over-treatment. One possible way to increase the specificity of DCE-MRI is to combine it with information from mammography.

## 1.3 Importance of Fusing Information from Mammography and MRI

Depending on the type of the cancer and the stage of the disease, usually two types of treatments are considered; mastectomy and lumpectomy. Mastectomy is a surgery

to remove all breast tissue from the body as a way to treat or prevent breast cancer. Lumpectomy is a breast-conserving surgery in which only the tumor is removed from the breast, and treatment is done with the smallest possible change in the organ. Women who have surgery as part of their breast cancer treatment may choose breast reconstruction surgery to rebuild the shape and look of the breast. Therefore, preserving the breast tissue as much as possible is of the great importance, which demands early-stage detection and accurate localization of the lesions.

Breast surgeons usually rely on physical examination of the breast to locate the tumors, and in cases where it is not applicable, they often prefer mammography. However, the applicability of mammography for non-palpable breast malignancies has been limited to the cases when the latter are visible on mammograms. At the same time, the situations in which the non-palpable lesions are occult to mammography such that the surgeon could no longer use the mammograms or the physical exam to localize lesions - the situation is particularly aggravated in the presence of multifocality. In these cases it is common to take breast MRI for better localization of the tumor. However, usually it is hard to interpret 3-D images. Therefore, the availability of "MRI-enhanced" mammograms could substantially improve the quality of surgical care, reducing the risk of postoperative complications as well as precluding the need for repeated surgical interventions. Accordingly, to assist the surgeon in choosing an optimal surgical plan and for breast lesion detection and localization, it is necessary to use mammograms and MRIs together, which possibly results in better treatment of breast diseases [89].

MRI and mammography are complementary and not exclusive; none of them can be substituted by the other. On one hand, mammography is low-cost and provides a projective image of the compressed breast. The relatively low sensitivity of mammography limits its efficacy in patients with a relatively dense composition of breast tissue, which tends to be mammographically occult. On the other hand, MRI gives a 3-D representation of the disease and does not miss any possible tumor. However, despite MRI's high sensitivity (reported as 93% to 100% [84]) and high negative predictive value, it shows variable and generally lower specificity (ranging from 37% to 97%) in comparison to mammography and breast ultrasound. Moreover, despite the superb ability of preoperative MRI to delineate the spatial extent of multi-focal and multi-center disease, its use does not guarantee a reduction in the rate of positive margins and hence does not always lead to an improvement in surgical outcomes. However, if it was possible to automatically determine a spatial correlation between MRI scans and their corresponding mammograms, one could augment the mammograms with information on the location and shape of MRI-detected lesions.

In addition, transferring contrast from breast MRI to mammogram can be used to assist radiologists in automatically correlating temporal mammographic images of the same

view, or when they relate findings from the CC and the MLO view mammograms. Screening with two mammographic views improves the detection accuracy of abnormalities in the breast, where two projections allow a better estimation of the conspicuity of lesions. Establishing such correspondences can reveal lesions hidden by glandular tissue in one projection, decreasing the chance of missing subtle cancers [11].

In conclusion, to improve the specificity of MRI and sensitivity of mammography findings as well as to facilitate biopsy, these imaging modalities should be used together. In other words, it is necessary to fuse their information by transferring dynamic contrast from one modality to the other one. This diagnostic fusion helps to locate the *same* lesion in the MRI and mammography scans concurrently.

## 1.4 Problem Statement

Establishing correspondences between a breast MRI and a mammogram requires one to find a spatial transformation that relates the coordinates of breast tissue in its pendulous and compressed states based on the imaging data alone. This problem can be conveniently formulated as problems of *image registration*, which, in the case at hand, can be further characterized as being both Cross-Modal and Cross Dimensional (CMCD). Moreover, the expected ill-posedness of CMCD formulation is further exacerbated by the effect of mechanical compression of the breast during mammography examination along with the fact that, as opposed to MRI scans, mammographic images are, in fact, projective. Hence, it hardly comes as a surprise that the range of approaches to the problem of 3-D breast MRI to 2-D mammography registration remains comparatively limited, while the drawbacks of existing solutions hamper their widespread adoption into clinical practice. As a result, achieving an accurate alignment is challenging and difficult. Even though alignment may not be perfect, bringing the correspondences of two images close enough to each other, e.g., under 10 mm, would provide valuable information by decreasing the size of the region of interest.

The goal of this research is to develop a theoretical framework and algorithmic methods for information fusion of digital mammograms with their associated MRI scans in CMCD+ Spatial Deformation (SD) setting. In other words, the aim is to find the correspondences between 3-D breast MRI and 2-D-mammogram. Given two real-valued images $f$ (3-D MRI) and $g$ (2-D-mammogram) defined over some (typically rectangular) domain $\Omega \subset \mathbb{R}^3$, our problem consists in finding a spatial transformation $\varphi : \Omega \longrightarrow \Omega$ that is capable of bringing $f$ into close correspondence with $g$. To find the optimal $\varphi$, a similarity measure

between $g$ and projected-deformed version of $f$ should be maximized. The registration task can be formulated as an optimization problem

$$\varphi^* = \arg\max_{\varphi \in \Phi} \quad \mathcal{S}\big(\mathcal{P}(f \circ \varphi), g\big) \tag{1.2}$$

where $(f \circ \varphi)(\mathbf{r}) = f(\mathbf{r} + \varphi(\mathbf{r}))$, $\mathbf{r} \in \Omega$, and $\mathcal{P}(f \circ \varphi)$ indicates the projection of $f \circ \varphi$ onto 2-D plane of $g$. $\mathcal{S}$ is a similarity measure between $g$ and $f \circ \varphi$, and $\Phi$ is a set of acceptable spatial transformations, e.g., topology preserving homeomorphism transformation. As it is seen from this equation, we are looking for a spatial deformation which brings two images from two different modalities and different domains to spatial alignment, i.e. we want to find a solution to a CMCD+ SD problem. Note that $f \circ \varphi$ is in 3-D but $\mathcal{P}(f \circ \varphi)$ is in 2-D just like $g$ which makes their alignment possible.

## 1.5 Main Contributions

In the literature, there is a lack of a generic and consistent solution to the problem of fusing mammograms and breast MRI images and using their complementary information. Most of the existing MRI to mammogram registration techniques are based on a biomechanical approach that builds a specific model for each patient to simulate the breast deformation. Bio-mechanical approaches are user-dependent and their results vary with initial conditions. For example, for the same subject, if the position of the patient or the initial configuration of the model changes slightly, the registration results will be different. Besides this, bio-mechanical methods need a third-party solver to numerically estimate the breast deformation.

In contrast with complex standard methods relying on patient-specific bio-mechanical modeling, we developed a new method which offers substantial improvement in computational complexity, independence of commercial software packages and ability to generalize to multiple sides and patient groups. While traditionally the breast deformation was estimated in a single stage, we came with the idea of splitting the total deformation into two parts, namely the global and the residual deformation. The global deformation, which is the significant part of the deformation, is almost common among all patient with much less inter-patient variability, and consequently it is *predictable*. In this thesis, we use a mathematical formulation to predict the value of global deformation followed by estimating the residual part. Predicting the global part of the deformation takes us close enough to the solution so that the residual part goes into the category of small magnitude, which makes it easier to compute from numerical point of view. In this way, our proposed physical-aware

mathematical solution offers computationally simple and standardizable means of prediction, while being dependent neither on excessive image preprocessing nor on the knowledge of any physical properties of the breast.

Estimating a geometric transformation that aligns MRIs and mammograms is a very challenging problem, and consequently, before approaching it, one needs to solve a scope of many sub-problems. To estimate the residual deformation, it is quite essential to synthesize a mammogram from the MRI volume, which requires extracting the geometry of the breast, isolating the breast tissue from the body and segmenting the breast voxels either as adipose or fibroglandular. We will discuss the preprocessing steps in more detail.

The main contributions of this work can be summarized as follows,

- Developing a new mathematical approach toward the alignment between breast MRIs and mammograms. This method does not require any biomechanical model and is capable of being standardized.
- Proposing two new algorithms to predict the breast motion in mammography. I used only the geometry and surface of the MRI volume to establish the shape of the deformed breast, and consequently, the breast deformation.
- Refinement of the results of the proposed alignment methods through an intensity-based Free Form Deformation (FFD) Model. I have also explored two similarity measures, namely mutual information and sum of square distance, to check the quality of the registration.
- Developing two novel approaches to do whole breast segmentation in both mammogram and MRI. In these methods, I take advantage of Deep Learning (DL) and graph search techniques to find the boundary between the breast tissue and body.
- Presenting a novel approach to segment the breast MRI to fibroglandular and adipose tissue. This is necessary for registration refinement by the FFD model.
- I validated the developed registration framework with a clinical dataset, using cases with identified lesions in both modalities, annotated by experts.

## 1.6 Outline

The remainder of the thesis is organized as follows. Chapter 2 provides a literature review and presents some technical preliminaries, including the FFD model and X-ray mammo-

gram simulation from MRI, necessary for the presentation of our results.

Chapter 3 discuss the details of three pre-processing steps: a) segmentation of the breast tissue from background in MRI scans, b) separating breast tissue from pectoralis major in MLO mammograms and c) classifying the internal structures of the breast to adipose and fibroglandular in MRI scans.

In Chapter 4, two new global deformation estimation algorithms along with details of residual deformation estimation are proposed. These g methods are based on superquadratic function model and MRI surface evolving.

In Chapter 5, the proposed registration framework on a clinical dataset is evaluated by registering MRI images to CC and MLO mammograms.

Finally, Chapter 6 includes conclusions, possible application of proposed framework and potential directions for future research.

# Chapter 2

# Background and Literature Review

In this chapter, the main concepts of image registration along with different types of registration algorithms will be reviewed. Basic definition of image registration and some general image registering methods are discussed in Section 2.1. Different factors of registration (e.g., transformation types, optimization methods, similarity measures and validation) are explained. In Sections 2.2 and 2.3, registration techniques which are applied to different types of breast images, e.g., MRI and X-ray, are presented.

## 2.1 Image Registration

Image registration (aka alignment), is one of the key tasks in image processing and in medical imaging in particular. Given two digital images defined over a shared spatial domain, the most quintessential task of image registration is to find a spatial transformation which brings them to the same coordinate system. These images could be taken from a different angle with one or two different sensors, and consequently they have different coordinate systems. The transformation aligns the two images so that the local intensities and features of corresponding structures can be compared directly. Consequently, it becomes possible to combine information about the scene that is captured by these two images. Figure 2.1 illustrates the general idea of image registration.

Formally, the goal of image registration is finding a spatial transformation function or geometric model $\mathcal{T}$ that maps two images to each other. Given the transformation $\mathcal{T}$, the coordinate $\mathbf{r}_2$ is computed as

$$\mathbf{r}_2 = \mathcal{T}(\mathbf{r}_1) \tag{2.1}$$

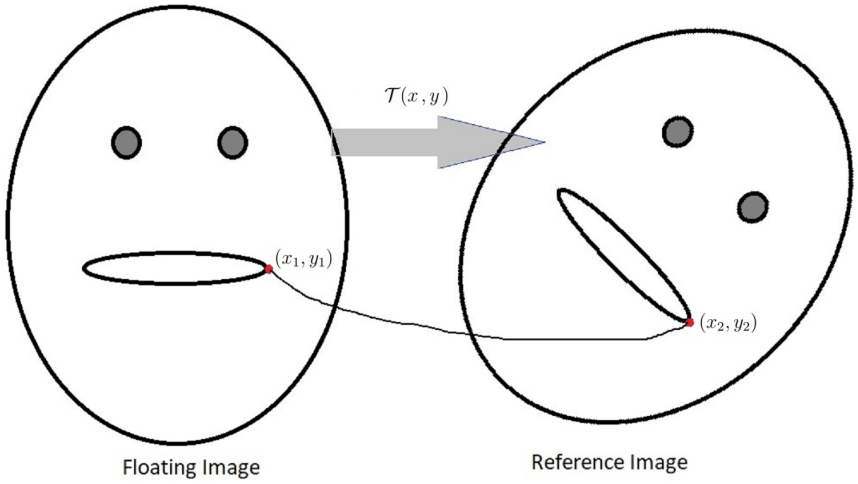


Figure 2.1: Illustration of image registration task.

Transformation $\mathcal{T}$ is applied to one of the images, which is called the moving or floating image, while the other one remains unchanged and it is called the fixed or reference image. Therefore, the intensity value of the warped floating image at point $\mathbf{r}_2$ is equal to its value at point $\mathbf{r}_1$. Depending on the problem in hand, the choice of geometric transformation $\mathcal{T}$ is critical. To compute this transformation, often, a similarity measure is maximized between the fixed and the floating images. As it is shown in Figure 2.2, the main components of a registration task are floating and reference images, transformation function, searching strategy (optimization) and similarity measure, which is discussed in the next sections. In this figure, images are 2-D, thus, $\mathbf{r}_1 = (x_1, y_1)$ and $\mathbf{r}_2 = (x_2, y_2)$.

It deserves noting that images are essentially discrete representations of a continuous scene, and the intensities at the pixel positions form a grid of the continuous space. Hence, by applying a transformation at a point in one of the images, the new transformed position may not coincide with a pixel center in the other image. To solve this problem, it is often necessary to find the intensity values at a off-grid coordinates which necessitates image interpolation.

We can categorize image registration algorithms based on the properties which they use to do the alignment:

- **Feature based**: In this type of registration, some features or landmarks are found from reference and floating images. Using these common points in two images, the corresponding transformation for each pixel in the floating image is calculated. Find-

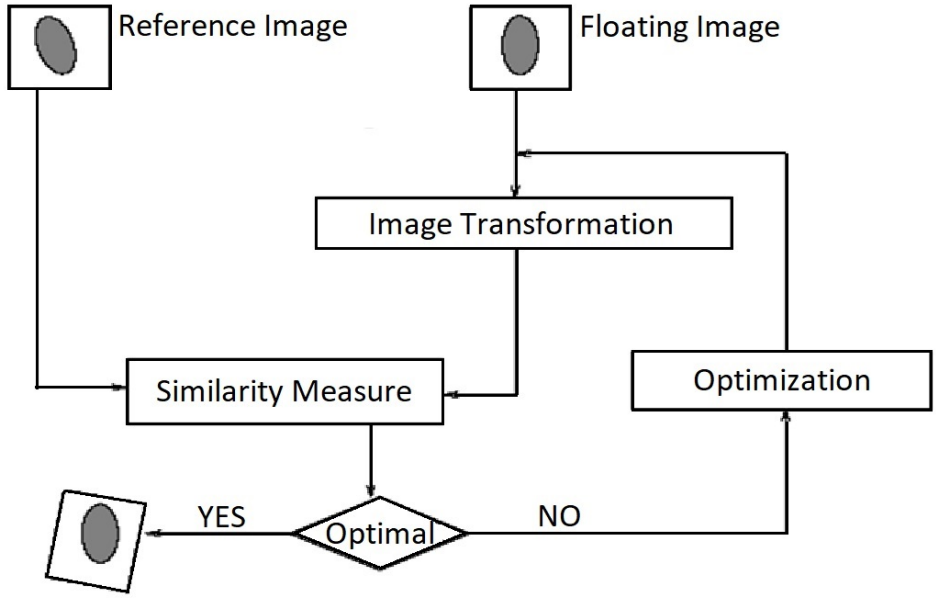


Figure 2.2: Main components and steps of image registration.

ing these points is the most difficult and critical step of this type of registration technique. Finding corresponding features or landmarks can be done automatically or manually. Automatic algorithms are not accurate enough, and manual extraction is laborious and subjective, while the use of markers is not always applicable. However, these type of registration algorithms are fast in comparison to other types of registration methods as they use a few points to find the displacement vector of each pixel.

- **Intensity based**: Rather than relying on the features, the methods of this group use image intensities directly. The critical factor of intensity based registration algorithms is the similarity measure that they use as a criterion to judge how well two images are registered. The similarity measure is iteratively maximized between the two images by updating the parameters of the transformation function. Since these methods use the intensity of all pixels in the image they are generally more robust than feature-based techniques.

### 2.1.1 Geometric Transformation Function

The key in image registration is to find the best geometric transformation which brings floating and reference images into alignment. Also, it is necessary to restrict it to a set of possible geometric transformations. The transformation function can be either parametric or non-parametric. The former is defined by a small set of parameters while the latter satisfies certain regularity conditions, e.g., bounded gradient or a smooth function with continuous first or higher-order derivatives. The most used transformation functions are *rigid*, *affine* and *elastic* (non-rigid) which will be explained next.

- **Rigid**: The transformation function is rigid-body, where it is assumed that the floating image is only rotated and displaced with respect to the reference image. The transformation function is defined as follows:

$$\mathcal{T}(\mathbf{r}) = \mathcal{R}\,\mathbf{r} + \mathbf{t} \tag{2.2}$$

  where $\mathcal{R}$ denotes the rotation matrix and $\mathbf{t}$ is a constant vector giving the translation of the origin. Thus, in order to align the two images, one only needs to estimate $\mathcal{R}$ and $\mathbf{t}$. For the 3-D case, the number of parameters is six (3 Euler angles to construct the rotation matrix $\mathcal{R}$ and 3 displacements in each direction $x$, $y$ and $z$).

- **Affine** : This transformation composed of a rigid transformation along with scaling and shearing in each direction. Affine transformation is formulated as follows:

$$\mathcal{T}(\mathbf{r}) = \mathcal{A}\,\mathbf{r} + \mathbf{t} \tag{2.3}$$

  where the scaling, shearing and rotations are included in $\mathcal{A}$. For 3-D images, the degree of freedom is 12, where one needs to estimate 9 elements of matrix $\mathcal{A}$ along with three values of $\mathbf{t}$. The main property of an affine transformation is that it preserves parallelism; so parallel lines are still parallel after transformation.

- **Non-rigid or Deformable** : This type of transformation allows complex deformation with a large degree of freedom. It usually is applied in medical image registration, especially in the case of organs with a highly deforming nature. This type of registration is not as tractable as affine or rigid transformations, and thus far, a plethora of approaches have been proposed to address this issue. One of the most popular non-rigid transformations is FFD which is based on B-splines curves [136]. A mesh is applied to one of the images and the points of this mesh are considered as control points of a B-splines equation. By moving these points, the other pixels will lie on the

B-spline curve, and the deformation in each pixel will be known. B-splines can capture complex, local, and non-rigid deformations. Hence, it is common to use a global transformation (such as rigid or affine) before applying the FFD. In other words, first, the general transformation between two images is compensated, and then the FFD method is applied to refine the transformation for each pixel. There are some other non-rigid registrations techniques which are also popular, including but not limited to optical flow [72], poly-affine transformation [3] and curvature-based scheme [35]. In this work, we focus on FFD transformation model which is explained next.

**Registration Using FFD:** A Free form deformation model is utilized to capture the local displacement of every single pixel (in 2-D) or voxel (in 3-D). Transformation, at each point $\mathbf{r} \in \mathbb{R}^n$ (where $n$ is the dimension), between two input images is parametrized as a linear combination of B-spline curves. Figure 2.3 illustrates the main steps of this method.

For a given three-dimensional reference image $g$, with voxel coordinate $\mathbf{r} = (x, y, z)$ and voxel intensity of $g(\mathbf{r})$, and floating image $f$, with voxel intensity of $f(\mathbf{r})$, a voxel-wise displacement vector $\varphi(\mathbf{r}) = \varphi^x(\mathbf{r})\mathbf{i} + \varphi^y(\mathbf{r})\mathbf{j} + \varphi^z(\mathbf{r})\mathbf{k}$, providing an anatomical mapping from $f$ to $g$, can be derived by maximizing the similarity measure $\mathcal{S}$. Note that in this case, $\mathcal{T}(\mathbf{r}) = \mathbf{r} + \varphi(\mathbf{r})$. The deformation $\varphi^l(\mathbf{r})$ (where $l \in \{x, y, z\}$) is parameterized using the uniform cubic B-spline basis, which provides a sparse representation of $\varphi^l(\mathbf{r})$ in terms of the B-spline basis coefficients $C^l = \left\{c_i^l\right\}_{i=1}^{M}$ ($M$ is the number of the control point in

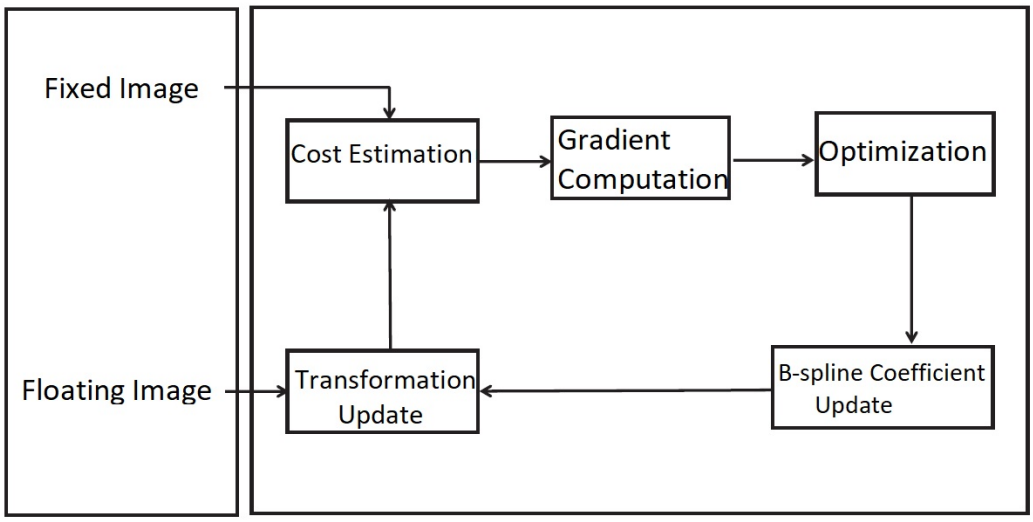


Figure 2.3: The registration framework based on FFD model.

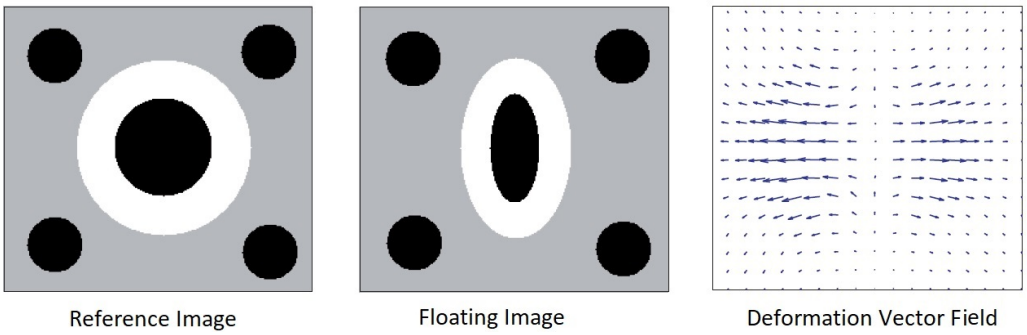


Figure 2.4: Example of 2-D deformation field

the domain) while introducing continuity into the deformation model. Therefore, one can formulate the deformation $\varphi^l(\mathbf{r})$ at any coordinate $\mathbf{r}$ as follows [92],

$$\varphi^l(\mathbf{r}) = \sum_{i=1}^{M} c_i^l \boldsymbol{\beta}\left(\frac{\mathbf{r}}{\Delta} - \boldsymbol{\lambda}_i\right) \tag{2.4}$$

where $\boldsymbol{\lambda}_i$ is the coordinate vector of a lattice point (control point's locations which are uniformly distributed over $\Omega$ with a predefined distance $\Delta$ from each other), and $\boldsymbol{\beta}(\mathbf{r}) = \beta(x)\beta(y)\beta(z)$ is a separable convolution kernel, where $\beta(x)$ is a cubic B-spline function defined as below.

$$\beta(x) = \begin{cases} \frac{1}{6}\left(4 - 6x^2 + 3|x|^3\right), & 0 \le |x| < 1 \\ \frac{1}{6}(2 - |x|)^3, & 1 \le |x| < 2 \\ 0, & 2 \le |x| \end{cases} \tag{2.5}$$

Since the support of $\beta(x)$ is 4, hence, only those $c_i^l$s corresponding to the $4 \times 4 \times 4 = 64$ nearest control points (which are referred to as a tile of voxels within the volume) to $\boldsymbol{\lambda}_i$ contribute to the sum in (2.4). The coefficients of B-splines ($c_i^l$, $i = 1, 2, 3, ..., M$ and $l \in \{x, y, z\}$) are computed by solving the following optimization problem,

$$C^* = \arg\max_{C} \mathcal{S}\left(g(\mathbf{r}), f \circ \varphi(\mathbf{r})\right) \tag{2.6}$$

where $C = \{C^x, C^y, C^z\}$ and $f \circ \varphi(\mathbf{r})$ represents the image $f(\mathbf{r})$ transformed into the coordinate system of $g$ by displacement vector field of $\varphi(\mathbf{r})$, i.e., $f(\mathbf{r} + \varphi(\mathbf{r}))$. A 2-D example of a displacement vector field is illustrated in Figure 2.4.

### 2.1.2 Similarity Measures

To check the quality of registration, it is common to compute the similarity between the reference and the warped image. Similarity measures can be both applied in intensity-based and feature-based registration methods to show how well two images are aligned. Intensity-based measures do not require any particular pre-processing and, consequently, are more popular and widely used. We will only consider intensity-based similarity measures in this work.

There is a wide range of intensity-based similarity measures that can be used for image registration. The most straight forward similarity measure consists of searching for a direct relationship between the images' intensities and is known as Sum of Squared Difference (SSD) which is formulated as follows [4],

$$\text{SSD} = \int_{\mathbf{r}\in\Omega} |g(\mathbf{r}) - f_{\mathcal{T}}(\mathbf{r})|^2 d\mathbf{r} \tag{2.7}$$

where $f_{\mathcal{T}}$ is the floating image $f$ warped by transformation $\mathcal{T}$, and $\Omega$ denotes the domain of the reference image $g$. This measure requires both images to have a one-to-one relationship in terms of intensities. However, while dealing with images from the same object in different modality or even with identical modality but different scanners, images can have different intensity distributions. Although it is simple and easy to implement, this measure is not suitable for images with a significant difference in their intensity distribution.

To address the issue with SSD, Normalized Cross Correlation (NCC) is frequently applied in image registration. This measure computes the linear correlation between two images, even-though their intensity differs significantly. NCC is computed as follows [86],

$$\text{NCC} = \int_{\mathbf{r}\in\Omega} \frac{\big(g(\mathbf{r}) - \bar{g}\big)\big(f_{\mathcal{T}}(\mathbf{r}) - \bar{f_{\mathcal{T}}}\big)}{\sigma_g\, \sigma_{f_{\mathcal{T}}}} d\mathbf{r} \tag{2.8}$$

where $\bar{g}$ and $\bar{f_{\mathcal{T}}}$ represent the average intensity value of $g$ and $f_{\mathcal{T}}$, respectively while $\sigma_g$ and $\sigma_{f_{\mathcal{T}}}$ are the standard deviations of intensities of $g$ and $f_{\mathcal{T}}$. Still, this measure is not suitable for multi-modal image registration where the relation between intensities of two images may not be linear.

There are measures from information theory that are more suitable for multi-modal image registration. These measures are usually based on the distribution and entropy of the image intensities. To compute any entropy-based measure, one needs to build a joint histogram and Joint Entropy (JE) of the images. The joint histogram contains the occurrence of each combination of paired intensities and is normalized in order to compute

the Joint Probability Distribution Function (JPDF). JE of the reference and the floating image can be computed as follows [139]:

$$\mathrm{H}(g, f_{\mathcal{T}}) = -\int_0^1\!\!\int p(r,s)\log\big(p(r,s)\big)ds\,dr \tag{2.9}$$

where $p(r,s)$ stands for the probability of co-occurrence of intensity $r$ from image $g$ to intensity $s$ from image $f_{\mathcal{T}}$. Note that the image intensity is normalized to $[0,1]$. The application of this type of measure can be complicated by the need for computing the joint probability distributions. For instance, it may require interpolation or any partial volume approach. Using interpolation, the floating image is first resampled and then each occurrence is added as one into the histogram. The partial volume approach consists of adding a weight value, between zero and one, to the joint histogram according to the transformation [144]. Another strategy to compute the joint histogram is the Parzen window solution, where it adds weight to the histogram in the neighborhood of the voxel intensities [145]. Experiments have indicated that JE was promising, yet no rigorous theoretical derivation was provided.

Mutual Information (MI) is the most popular measure from information theory which considers the common information between the reference and warped image. By maximizing this information, the alignment quality will increase [150]. Collignon et al. [88] and Viola et al. [162] introduced MI as an alignment measure which is defined as follows,

$$\mathrm{MI} = -\int_0^1\!\!\int p(r,s)\log\left(\frac{p(r,s)}{p_g(r)p_f(s)}\right)ds\,dr \tag{2.10}$$

where $p_g(r) = \int p(r,s)\,ds$ and $p_f(s) = \int p(r,s)\,dr$ denote the marginal intensity probabilities of images $g$ and $f_{\mathcal{T}}$, respectively. The use of marginal probabilities makes mutual information a more suitable alignment measure where there's limited scene overlap between images. Mutual information takes its maximum value when the underlying images are absolutely dependent (one of them is a function of the other one). In such cases, the joint probability matrix (or joint histogram matrix) is diagonal. Conversely, if the images are independent of each other, then the mutual information takes its minimum value, i.e. zero [144].

In [151], Normalized Mutual Information (NMI) has been introduced, and it has been shown that it is more robust to the overlap between images than MI. It is defined as ratio between sum of entropies of two images and their joint entropy.

$$\mathrm{NMI} = \frac{\mathrm{H}(g) + \mathrm{H}(f_{\mathcal{T}})}{\mathrm{H}(g, f_{\mathcal{T}})} \tag{2.11}$$

where

$$\mathrm{H}(g) = -\int_0^1 p_g(r) \log\big(p_g(r)\big)\, dr$$

and

$$\mathrm{H}(f_{\mathcal{T}}) = -\int_0^1 p_f(s) \log\big(p_f(s)\big)\, ds.$$

The problem with most of the intensity-based methods, especially those from information theory, is that they do not consider spatial information at all. Recently, a few numbers of studies attempted to combine the spatial information with the pixel's intensity to create a robust measure. In particular, a new computational pipeline has been proposed in [82] using a conditional MI which takes into account spatial information using a weighting strategy based on the voxel positions. Zhuang et al. [175] modified this algorithm and introduced spatial MI. In [174], spatially encoded mutual information has been proposed which is achieved by introducing a spatial variable and computing the associated entropy measures according to the spatial coordinates of the sample points.

There are many other similarity measures from information theory (e.g., $I^{\alpha}$ information, $M_{\alpha}$ information, cross-entropy, and Rényi entropy [121]) which are used in image registration, but they are not as common as the measures were mentioned above.

### 2.1.3 Optimization

Optimization algorithms in image registration are not specific to the field, and they are common in other applications as well [123]. Depending on the transformation function type, different optimization strategies might be used. For instance, the Powell optimization method [123] is suitable for registering medical images while the transformation $\mathcal{T}$ is supposed to be rigid or affine. On the other hand, for non-rigid registration methods where the number of parameters is much more in comparison to rigid transformations, methods like gradient descent [136] or Gauss-Newton like approaches [160] are proper. To apply the nonrigid registration method it is often required to compute the first-order and the second-order derivative of the similarity function respect to transformation parameters. Therefore, the choice of similarity measure is critical. For example, computation of the derivative of SSD is much simpler than that of MI. Furthermore, to avoid local optima, the similarity measure (or objective function) should vary smoothly by chaining the transformation parameter.

To improve the convergence properties of the algorithm, a multi-resolution strategy is often used in the literature [38]. A Gaussian pyramid is generated that contains resampled versions of the images at decreasing resolutions. Starting with the pair of floating and fixed images at the lowest resolution, registration is performed using a coarse grid of control points. The registration results are transferred from one resolution level to the next higher level, and registration is run again, up to full resolution. This approach ensures that large deformations can be recovered early at a low resolution and more detailed deformations are accounted for at increasingly fine resolutions.

Notice that all types of deformation are not physically plausible and, consequently, often a regularisation term is added to the objective function to penalize any irregular transform. Practical regularization approaches usually rely on rather simple mathematical properties of deformations that are suitable from a physiological point of view. For example, the smoothness of displacement fields is one of the important regularizations being considered in most of the non-rigid transformations.

### 2.1.4 Validation

The purpose of validation is to quantitatively assess the final alignment, and show how well the algorithm has performed. In other words, besides the visual assessment, a numerical value of the registration's performance is assigned. If the ground truth transformation between the two images is available, one can easily compute the error as the average distance of pixels of the transformed image with pixels in the ground truth image, which is obtained by applying ground truth transformation to the floating image.

$$\mathcal{E} = \int_{\mathbf{r}\in\Omega} |f_{\mathcal{T}}(\mathbf{r}) - \tilde{f}(\mathbf{r})|\, d\mathbf{r} \tag{2.12}$$

where $f_{\mathcal{T}}$ denotes the floating image warped by the transformation function $\mathcal{T}$ and $\tilde{f}$ represents the same image deformed by ground truth transformation. However, the ground truth transformation is usually not available, then other approaches should be applied to judge the registration performance.

An alternative method that is common in computing the registration accuracy is to use corresponding points or landmarks. These points are known in both images and after registration, ideally, they should align with each other. The average distance between these corresponding points can be used to compute the registration accuracy. In medical images, they are obtained either by fiducial markers attached to the imaging object/organ or by experts in the field, e.g., radiologists. However, this manipulation may be a source

of error as well, as it is generally difficult to accurately locate the corresponding points. Gold-standard registration is another approach that is utilized to compute the registration accuracy. In this method, it is assumed that there is an accurate and standard registration method, and one can compute the accuracy by comparing registration results with that of the accurate method. In all of these mentioned methods, mainly the distance between points is computed.

If it is not practical to extract identical corresponding points in the floating and reference images it might be possible to provide the corresponding regions ($R_f$ and $R_g$) based on their boundaries. These boundaries can be applied to estimate the registration accuracy being defined as the overlap between two corresponding regions. In this case, there are validation metrics (also can be applied in image segmentation tasks), which are used to quantify the registration accuracy. These validation assessments can be summarized as follows:

- **Dice Similarity Coefficient** (DSC): It is defined as $(2|\mathrm{R_f} \cap \mathrm{R_g}|)/(|\mathrm{R_f}| + |\mathrm{R_g}|)$, where the modulus sign $|\cdot|$ is used to define the set size (i.e., the number of pixels in its related binary mask), while $\cap$ stands for set overlap. The DSC takes its maximum value, one, if two regions completely overlap each other, and it will take zero if regions $R_f$ and $R_g$ have no overlap.

- **Jaccard Coefficient** (JAC): It is defined as $(|\mathrm{R_f} \cap \mathrm{R_g}|)/(|\mathrm{R_f} \cup \mathrm{R_g}|)$, and known to be less sensitive to visual errors, and a high value (close to one) is desirable.

- **Sensitivity** (SEN): It is defined as $\mathrm{TP}/(\mathrm{TP} + \mathrm{FN})$, where TP and FN stand for the true positive and false negative, respectively. Note that the voxels (or pixels) that do not belong to $R_g$ (in reference image $g$) and $R_f$ (in floating image $f$) are considered as background. Lower values of SEN indicate a relatively large number of misclassified pixels.

- **Specificity** (SPE): It is defined as $\mathrm{TN}/(\mathrm{TN} + \mathrm{FP})$, where TN and FP stand for the true negative and false positive, respectively.

- **Accuracy** (ACC): It is based on the overlap between $R_f$ and $R_g$ and also background regions in two images, $(\mathrm{TP} + \mathrm{TN})/(\mathrm{TP} + \mathrm{TN} + \mathrm{FP} + \mathrm{FN})$.

- **False Positive Rate** (FPR): FPR is defined as $\mathrm{FP}/(\mathrm{FP} + \mathrm{TN})$, and small values of it (close to zero) is an indication of better performance of an algorithm.

- **False Negative Rate** (FNR): It is defined as $\mathrm{FN}/(\mathrm{FN} + \mathrm{TP})$ and, similar to FPR, an algorithm with smallest FNR is desired.

Breast image registration is generally between different X-ray images (MLO and CC), MRI images in the supine and prone position, and between MRI, X-ray and ultrasound images. The next sections elaborate more on these registration types.

## 2.2 Intra-modal Breast Image Registration

Intra-modal registration is the alignment of two images (of the same organ/object) produced by the same imaging modality, or even acquired by an identical sensor. We first focus on breast MRI image registration and then discuss different registrations among X-ray breast images.

### 2.2.1 MRI Image Registration

A DCE-MRI protocol is based on collection of images which are acquired concurrently with administration contrast agent. The coordinates of these temporal images might differ due to involuntary subject motion (e.g., breathing and movements of the patient). The existence of this kind of motion requires re-alignment of the images before further analysis. To correct the motion artefacts, non-rigid image registration has been successfully applied [136],[132]. In particular, one of the original works is by Rueckert et al. [136], where the authors modeled the transformation by B-spline kernels. This algorithm has been improved in [132] by adding a new constraint of volume conservation. It was shown that their proposed approach gives higher accuracy in the regions containing tumors when registering DCE-MRI images.

The use of the pharmacokinetic model for registration is another type of solution which has been attempted. Pharmacokinetic refers to an intensity transformation approach, rather than spatial transformation. In contrast to previous algorithms, pharmacokinetic-based registration methods assume hat image intensity does not remain constant with dynamic MR sequence. In these methods, a pharmacokinetic model is created to estimate the intensity variation among image sequence which results in an accurate motion estimation and compensation. Early work in this area was developed by Hayton et al. [55], and it later was improved by Xiaohua et al. [167] into an automatic joint registration and segmentation algorithm, making use of the pharmacokinetic parameter to drive tissue classification.

Valentin et al. [51] introduced a new registration technique based on Robust Principal Component Analysis (RPCA) to decompose a given DCE-MRI series into a low-rank and

a sparse component. This helps to robustly separate the motion components (which can be registered) from intensity variations that are left unchanged. DCE-MRI registration has been recently improved by Subashini et al. [149], where they proposed to use fat-based registration of breast DCE images, which is a promising technique for deformable registration.

Another breast MRI image registration is aligning images from prone to supine positions. Owing to the large deformations, which is mainly due to the change in the direction of gravity during prone and supine imaging, this task is challenging. Biomechanical models have been used in registration methods to include the direction of gravity reversal as prior knowledge. Due to limited knowledge about the exact in vivo tissue response to loading, among other factors biomechanical models and corresponding simulations are not accurate enough [53]. Augmenting the biomechanical simulations with intensity-based image registration techniques can boost the whole accuracy [32].

### 2.2.2 X-ray Image Registration

To determine the presence of breast disease, comparison of mammographic scans acquired from a patient at different time has been routinely done in breast radiology. Moreover, in the context of a clinical screening, it is of great importance to examine the temporal changes in mammographic features (including changes in the spatial distribution of radio-dense tissue) and to relate the spatial distribution of prediagnostic features to the tumor location [119]. This requires accurately identifying corresponding areas on serial mammograms of the breast. Variation in the imaging procedure such as positioning, breast compression, and X-ray set configuration, makes mammographic features appear at different locations on mammograms taken at separate time points. Additionally, sometimes radiologists want to register images from different views of breast tissue to discover the abnormalities. X-ray breast images registration can be clustered into three categories [1]: 1) temporal registration, where mammograms of the same breast tissue and the same view, taken at different times, are registered; 2) ipsilateral registration, where MLO and CC views of the same breast are registered; 3) bilateral registration, where registration is done between the images of the right and left breast from the same view.

The symmetry between right and left breast tissues is a critical consideration when interpreting breast images in X-ray mammography [70]. For instance, Byng et al. [18] investigated breast density patterns on X-ray mammograms, and using both subjective and objective measurements, reported symmetry between 30 left and right breasts . To use this symmetry information, bilateral registration techniques were employed to measure the amount of asymmetry between right and left breast attempting to improve the

detection of suspicious masses [138, 66, 79]. In particular, Trbalić [138] used thin-plate splines interpolation integrated into an intensity-based non-rigid registration approach to locate corresponding regions in the two mammograms. In [66], mutual information based on Tsallis entropy has been applied to perform the registration. It was demonstrated that Tsallis entropy could achieve higher registration accuracy in comparison to Shannon entropy. Registration accuracy was further improved by Yanfeng et al. [79] by proposing a two-step method: a region matching step for determining the correspondence between a pair of mammograms, and a bilateral similarity analysis step for dropping false positives in the detection. They showed that their method performs better in comparison to other state-of-the-art algorithms.

Recent studies have shown that the use of comparison mammograms at screening programs results in lower recall rates (6.9% with temporal analysis vs 14.9 % cross sectional analysis) [170]. Hence, mammograms, taken over a period of time, provide the radiologist with discriminatory information contributing toward the malignancy detection. The use of longitudinal analysis of mammographic scans range from local to global. Local registration methods, including B-splines, poly rigid and Demons registration [94], act at different regions of the image, modifying various regions of the image in different ways [29]. Nipple and center of mass alignment have been proposed to enhance the registration accuracy [157, 90]. Taking into consideration the spatial relations (to the right of, to the left of, below and above) is another temporal mammogram registration method, where the histogram of all possible angles between all pairs of points in a pair of Region Of Interests (ROI) is treated as a fuzzy set [87]. This method has been shown to improve overall detection efficiency. In [1], another solution has been illustrated which is based on a transformation model derived from the breast anatomy, namely the curvilinear coordinate system. In particular, breast tissue boundary was used to construct the curvilinear coordinates. Consequently, the resulting representation of the mammogram was rendered invariant to changes in the size, position, and orientation of the internal structures of the breast tissue.

Matching mammograms from MLO and CC views and incorporating their joined features into multi-view Computer-Aided Detection (CAD) systems has shown to significantly improve performance over single view CAD [159]. In some methods, the registering across views is often based on extracting suspicious regions from one view, computing their region-based features, and finding the most similar region on the ipsilateral view using these features [153]. Features include gray levels, morphological and texture features as well as location features, which describe the relative position of the region. Lesion-to-nipple distance was also used as a new feature to reduce false positive errors [153]. Another group of researchers proposed to simulate the deformation process during X-ray imaging (rotation, compression, projection) to determine the 3-D location of matched features from both

views [127], [169]. Thus for example, Qiu et al. [125] suggested applying a biomechanical model to map a lesion from CC and MLO mammograms to the MRI of the same patient, and then use the 3-D position of the lesion in the MRI to align temporal mammograms.

## 2.3 Multi-modal Breast Image Registration

Due to their different physical principle, X-ray mammography and MRI provide complementary diagnostic information. Therefore, both of these modalities are often read in combination for a definite diagnosis. However, the combined reading of mammograms and MRI requires a lot of experience. Therefore, image registration is applied to make this easier. Owing to huge spatial deformation in mammography, different dimensionality of images, patient positioning and compression state of the breast tissue, registering mammograms and MRI is an ill-posed problem. Furthermore, the different resolutions of these modalities (resolution of X-ray images is finer) makes this task even more complex. Many approaches have been proposed to automatically find correspondences between X-ray mammogram and breast MRI.

At a conceptual level, the solutions proposed thus far differ in how they: a) cope with the different dimensionalities of imaging modalities in use, b) model and estimate the geometric transformation parameters, and c) evaluate image similarity. Thus, for example, to overcome the problem with the discrepancy in image contrasts, Behrenbruch et al. suggested a solution based on feature-based image registration [9]. In its initial phase, the method computes and matches the spatial coordinates of several characteristic features (aka landmarks) within both MRI images and their related mammogram scans. Subsequently, the coordinates are used to estimate the deformation of interest employing a standard fitting procedure. A particular critical drawback of this approach, however, is due to the use of projected MRI images (rather than their volumetric counterparts), which overly simplifies the complex dynamics of mammographic compression.

A feature-based registration approach was exploited in [91] as well. In this case, however, the mammogram scans have been aligned with 2-D *slices* of MRI volumes (rather than their 2-D projections, as in [9]). Like other methods of this type, the algorithm relies on the assumption that the most salient features can be discerned in both the selected MRI slices and their related mammogram. Unfortunately, this assumption does not apply in the case of mammographically occult breast disease [17], which undermines the overall robustness of the proposed procedure.

On the other hand, a wide range of intensity-based registration algorithms has been

proposed to fuse information from MRI and mammography. In these methods, MRI volume is deformed by the transformation function and then projected to simulate a 2-D X-ray image. The similarity measure is maximized between the simulated and real mammogram by tuning the parameters of the transformation function. For example, Mertzanidou et al. proposed an intensity-based approach, in which the effects of mammographic compression were described by means of an affine transformation model [95]. In this case, the model parameters were estimated under the constraint of volume-preserving compression, resulting in a computationally simple and efficient algorithm. However, although the chosen transformation model is capable of explaining the global effects of mammographic compression (e.g., scaling, rotation, shifts, etc.), it does not seem to be adequate to describe the curvilinear displacements of breast tissue, which are likely to take place during its deformation.

It is important to emphasize that the ill-posedness of the problem of MRI to mammogram registration is mainly due to the extremely large magnitude of breast deformation during mammographic compression, which renders standard solutions ineffective, even when performed in combination with multi-scale computational schemes. Thus, taking into account the highly complex nature of such deformation, several studies considered the possibility of its prediction based on subject-specific biomechanical modeling using FEM-based methods.

The biomechanical methods simulate the effect of mammographic acquisition in a physically realistic way. They store information about the geometry and structure of the breast tissue and provide a physics relations to simulate mechanical deformations. FEM-based methods model the interrelationship of different tissue types by applying displacements, forces, and restrictions to the movement. A patient-specific biomechanical model is built using MRI volume which often needs some basic preprocessings. Typical preprocessing steps involved in building a biomechanical model are shown in Figure 2.5.

First, the breast tissue is isolated from other nearby organs, which involves finding air-breast and pectoralis-breast boundaries [46]. After extracting the breast geometry, which is restricted to skin and pectoralis muscle surface, one needs to segment the internal structure of the breast into different regions, or equivalently different tissue types. Having, labeled voxels in MRI to one of the known breast tissue types (e.g., adipose and fibroglandular) one can assign physical properties of that tissue to the corresponding voxel and predict its behavior during compression. Due to the low resolution of MRI images, it may not be possible to find the type of all breast internal tissues shown in Figure 1.1. Moreover, due to the physics behind MRI imaging, voxels belonging to different tissues may look like each other, e.g., lobules and ducts. For the sake of simplicity, in the literature, often voxels are labeled as fibroglandular (dense) or adipose (fat) tissue.

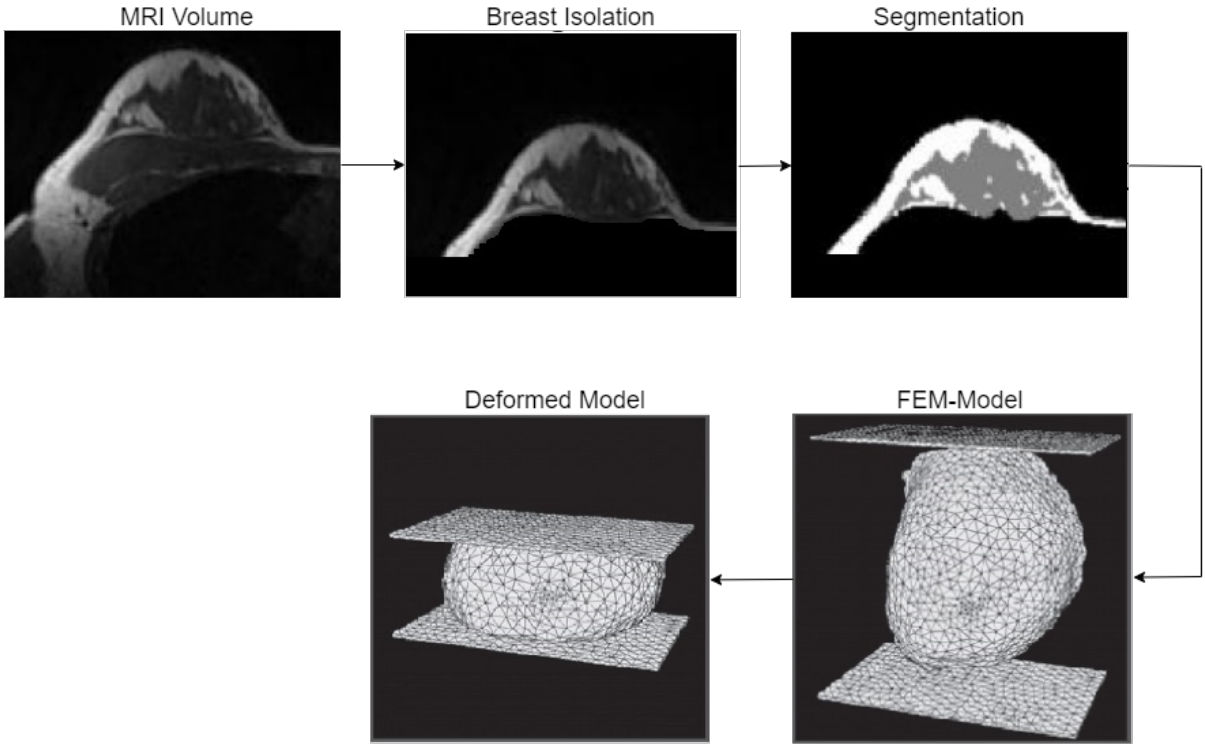


Figure 2.5: Preprocessing of FEM-based registration methods

Once internal tissues of the breast have been specified, the next step is to anatomically generate the realistic patient-specific FEM, which consists of two types of mesh generations, surface and volumetric meshes [41]. The surface mesh defines the external boundaries of the model, and the volumetric mesh accounts for the internal behavior of the model. These meshes break the whole MRI volume into smaller volumes known as elements. Based on the majority of voxel's label in an element, the corresponding physical property of that label (tissue) is assigned to that element. The complexity of the model is in direct relation to the resolution of the meshes (number of nodes or elements). On the other hand, there is a trade-off between the complexity and accuracy of the built model. Many efforts have been made to examine different mesh resolutions and mesh types, e.g., 4-node tetrahedral, to make this model as effective as possible [42], [59].

Once the model is defined in terms of its related meshes, the next step is to deform the obtained model to simulate the breast deformation during mammography. Finite Element (FE) analysis, which allows the simulation of large deformations (of the breast), is applied to reproduce the compressed breast. The Stress-Strain relationship is used to

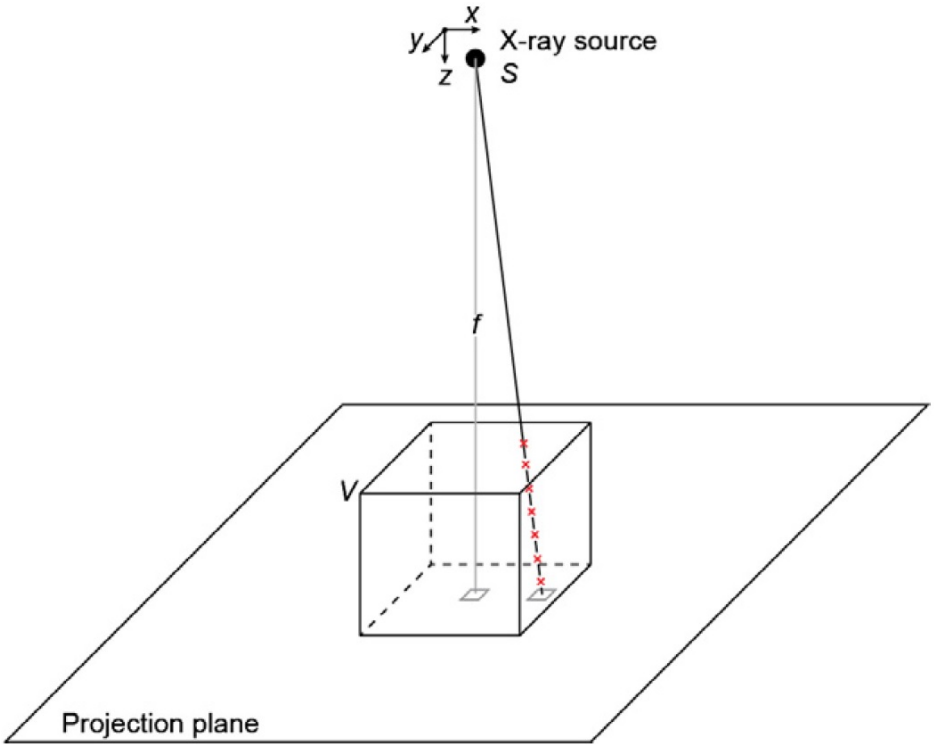


Figure 2.6: Simulating X-ray mammogram from a deformed MRI using ray-casting algorithm. Here $V$ represents the deformed MRI volume, and $f$ is the focal spot [97].

precisely simulate the biomechanical behavior of the breast tissue [41]. This relation can be linear, non-linear, or pseudo-nonlinear elasticity. Having physical properties of each element (Young's modulus) in hand, knowing the boundary conditions, applying external loads and forces, and the relation between strain-stress (for example Neo-Hookean), the model is deformed. This simulation can be done with many available FE solvers, such as ABAQUSTM and ANSYS commercial software packages or NiftySIm[1] and OpenCMISS [2] which are open source and publicly available.

The simulated deformation can be applied to the 3-D MRI volume to reproduce the shape of the breast in its compressed state. As the last step, a synthetic mammogram can be simulated by projecting the deformed MRI volume on a 2-D domain. In this case the application of Beer's law (Equation 1.1) along with the ray-casting algorithm

[1]available at : https://sourceforge.net/projects/niftysim/
[2]available at : http://opencmiss.org/downloads.html

allows one to produce the X-ray image from the deformed MRI. Note that MRI volume is segmented to adipose and fibroglandular voxels, and their attenuation coefficients are available. Figure 2.6 shows the projection geometry which is used to simulate a synthetic mammogram.

In the obtained synthetic mammogram, the intensity of each pixel (at location $(x, y)$) is proportional to the number of the fibroglandular and fat voxels in the path of the ray reaching $(x, y)$. In other words, the intensity depends on the thickness of fat and fibroglandular tissue along each ray, as given by

$$g(x, y) \propto \mu_f h_f + \mu_d h_d \tag{2.13}$$

where $\mu_f$ and $\mu_d$ denote linear attenuation coefficients of fat and dense tissues, respectively, while $h_d$ is the thickness of dense tissue along the ray reaching to $\mathbf{r}$, and $h_f$ shows the thickness of the fat tissue. Finally, after producing the synthetic mammogram, the similarity measure is maximized between the original and simulated mammogram to find the correspondences between MRI volume and X-ray mammogram.

To estimate breast deformation, the algorithms take advantage of FEM in different ways. For instance, one of the first efforts toward registering mammograms and breast MRI was proposed by Ruiter et al. [137] where a patient-specific biomechanical modeling approach was applied to simulate the large magnitude deformation of the breast tissue in mammography. In this method, it was suggested to deform the breast tissue by applying displacements on the surface nodes, in two directions: a) the direction of the projection (to account for the compression) and b) direction perpendicular to the projection (to take to account the anisotropic behavior of the breast under compression). The shape of the deformed breast and the boundary of the corresponding mammogram were used to estimate the 3-D shape of the breast tissue. After that, the boundary of the projection of the deformed breast was compared to that of the breast tissue in the X-ray mammogram, and their distances were calculated. Consequently, these distances were added to the displacements of the surface nodes of the deformed FEM model. Although this method simulates a sensible deformation of the breast tissue, it is not automatic, and it consists of several manual steps which may not be proper for clinical applications. For each patient, it needs to create a new FEM model which miight be challenging.

Using non-linear FEM, Angela et al. [74] have proposed another approach which is subject to contact mechanics constraints to reproduce the large compressive deformation. The parameters of FEM (e.g., the location and orientation of compression paddles) were optimized to provide the best match between the synthetic and clinical X-ray mammograms. Many assumptions regarding the tissue properties and the boundary conditions were made

to make the problem solvable. To check the error generated by these assumptions and to validate the framework, a few controlled experiments on the breast-shaped phantom has been done.

Mertzanidou et al. proposed to augment the FEM-based model with rigid-body transformation [98]. The transformation model has seven degrees of freedom, including parameters for both the initial rigid-body pose of the breast tissue before mammographic compression and those of the biomechanical model. Through an intensity-based framework, the authors simultaneously optimized the pose (rigid transform) and FEM parameters. To make their algorithm faster, it was suggested to decrease the volume resolution to $10\,\text{mm} \times 10\,\text{mm} \times 10\,\text{mm}$, and assume one homogeneous tissue type rather than assigning different material properties, i.e., fibroglandular and fat. Consequently, the number of the nodes was decreased in FEM model resulting in a lower computational cost, smooth meshes and free from artifacts. By optimizing NCC via hill-climbing approach, the mean registration error of $11.6\,\text{mm} \pm 3.8\,\text{mm}$ for the MRI to CC and $11\,\text{mm} \pm 5.4\,\text{mm}$ for the MRI to MLO view registrations were reached.

A fully automated method has been proposed in [148] which performs a complete registration of MRI volumes and X-ray images in both directions, from MRI to mammography and from mammography to MRI. Then, by applying C-Means and Otsu algorithms, the MRI voxels have been segmented to skin, fat and fibroglandular. Taking into consideration the skin physical properties in the biomechanical model, reduced the registration error to $4.2\,\text{mm} \pm 1.9\,\text{mm}$ for the MRI to CC and $4.8\,\text{mm} \pm 1.3\,\text{mm}$ for the MRI to MLO alignments.

In contrary to conventional FEM-based approaches, Eloy et al. proposed to align the density maps, extracted from the mammogram and MRI volume, rather than aligning the synthetic and actual mammograms [39]. Using Vollapar package[3], they build a density map from a mammogram which shows the thickness of fibroglandular tissue at each pixel location. On the other hand, by segmenting the MRI volume to dense and fat, a floating density map image is produced. In that work, mutual information was used as a similarity measure which was maximized by taking advantage of the simulated annealing algorithm. The transformation parameters were restricted to translation, rotation around the axis, elastic properties (Young's modulus), and amount of compression (distance between two mammography paddles). Their approach obtained a high-structural agreement between density maps regardless of the density of the breast tissue. The results showed that the similarity of the glandular tissue distributions and also the correlation between both images increases in denser breasts.

In [40], the same group of authors proposed to define the similarity measure using inten-

[3]Available at: https://volparasolutions.com/science-hub/breast-density/measuring-breast-density/

sity gradients. In particular, the authors projected the intensity gradient of the glandular tissue in the MRI volume to the mammographic space and tested two different gradient-based metrics, the normalized cross-correlation of the scalar gradient values and the gradient correlation of the vectoral gradients. Then, the biomechanical model extraction as well as numerical optimization was performed similar to their previous work in [39]. The performance of the two designed approaches was compared with an intensity-based FEM model as a baseline. The obtained results revealed that using a scalar gradient approach improves the registration accuracy, obtaining a registration error of $5.65\,\text{mm} \pm 2.76\,\text{mm}$ for CC and of $7.83\,\text{mm} \pm 3.04\,\text{mm}$ for MLO views.

In actuality, however, the above-mentioned solutions expose the main drawback of all FEM-based methods, *viz.* the strong dependence of their results to the initial conditions dictated by biomechanical modeling (let alone their excessive computational requirements due to the repetitive execution of the process of FEM-based prediction). In this case, the prediction error becomes a function of the geometric organization of breast tissue that is usually recovered through MRI image segmentation. Due to the presence of imaging artefacts, however, the latter is known to be a challenging task, which, in combination with using the average (rather than real) values of physical parameters, inevitably make the predicted deformation deviate from the actual one. As a result, the use of FEM-based methods comes at the cost of substantial between-subject variability, lack of standardization, reliance on a specific configuration of a numerical solver in use as well as the considerable dependence on interactions with the user. For these reasons, FEM-based MRI to mammogram image registration is still far from its incorporation into clinical workflows, remaining predominantly a subject of academic research.

# Chapter 3

# Preparatory Contributions

As it was mentioned in the first chapter, our goal has been to find an optimal spatial transformation which brings 3-D breast MRI images to a close alignment with the associated 2-D mammograms. However, before estimating this transformation, one needs to prepare these images for alignment, which requires a few preprocessing steps. First of all, breast MRI and mammogram images contain irrelevant information (other organs, e.g., lungs), and hence, it is required to segment and isolate the breast tissue from the background and other nearby organs existing in these images. In particular, the pectoralis major is often included in breast MRI and MLO view mammograms where it could be easily confused with fibroglandular breast tissue. Furthermore, as it was discussed in Chapter 2, to simulate X-ray mammogram from MRI scans employing ray-casting, it is essential to segment the internal structure of the breast MRI to either adipose or fibroglandular. Note that simulating X-ray mammograms from MRI images is necessary to estimate the residual deformation, which relies on breast properties. We proposed different algorithms to do each of these preprocessing steps, which will be discussed in this chapter.

## 3.1 Whole Breast Segmentation in MRI Scans

The performance of the registration relies on the accurate delineation of the breast boundary in MRI images. Due to the complex composition of breast tissue and its extensive inter-subject variability, this problem is known to be a challenging one. Whole breast segmentation can be broken down into two separate subproblems, namely locating: a) the breast-body boundary and b) the breast-air boundary. Although the latter is often

straightforward to address by means of standard edge detection algorithms, subproblem (a) turns out to be considerably more complicated in its nature. In particular, this subproblem amounts to detecting the 3-D surface which separates the breast from its adjacent pectoralis major muscle. In clinical breast MRI scans, pectoralis major muscle has a close proximity with fibroglandular tissue, which makes it challenging to distinguish the anterior pectoral boundary [171]. The partial visibility of pectoralis is further exacerbated by its complex fascial structure and of its surrounding connective tissue, which altogether renders the problem of breast segmentation far from trivial.

Over the last decades, the above problem has been addressed by a wide spectrum of different approaches, ranging from *semi-automatic* [154, 75, 69] to the scope of *fully-automated* methods [124, 130, 33]. However, semi-automatic methods have the disadvantage of being dependant on the laborious efforts of human interpreters, and fully-automated approaches despite the promise demonstrated by their results, their performance depends on the goodness of initialization which is left at the discretion of final user. The performance of the registration relies on the accurate delineation of the breast boundary in MRI images. Due to the complex composition of breast tissue and its extensive inter-subject variability, this problem is known to be a challenging one.

Among the most recent methods of breast segmentation are also those based on the ideas and tools of DL [100], [5]. Particularly, in [83], it is proposed to take advantage of transfer learning to leverage a pre-trained convolutional neural network (CNN), refined through additional training based on in-house data. In regard to the question of optimal network topology, different solutions have been discussed, e.g., in [133], [50] and [118], which advocated different extensions of a basic Unet architecture. Unfortunately, the performance of DL-based methods is known to degrade *pro rata* with a decrease in the number of (human annotated) training samples, which are frequently unavailable in sufficiently large quantities.

In an attempt to address some drawbacks of the existing methods of fully automated segmentation of breast MRI scans, we developed a simple, yet effective algorithm for finding reliable segmentation results in a computationally effective manner. The image gradient is used to generate a weighted graph, and the breast-body boundary is detected as the shortest path between two nodes of this graph. Details of our proposed solution are explained in the next section.

### 3.1.1 Proposed Approach

As mentioned earlier, the process of whole-breast segmentation can be arranged as a combination of two independent subroutines, *viz.* detection of the breast-body and the breast-air boundary. The former is defined by the deep layer of superficial fascia, which is typically difficult to discern in anatomical MRI scans due to limitations in the spatial resolution. For this reason, the problem of localization of the breast-body interface has long been considered to be a challenging one. To solve this problem, our proposed solution relies on Dijkstra's algorithm, which is a classical method of finding shortest paths (geodesics) over a weighted graph [26]. The algorithmic flow of the proposed solution is depicted in the block-diagram of Figure 3.1, where it is shown to consist of a total of six steps which are detailed next.

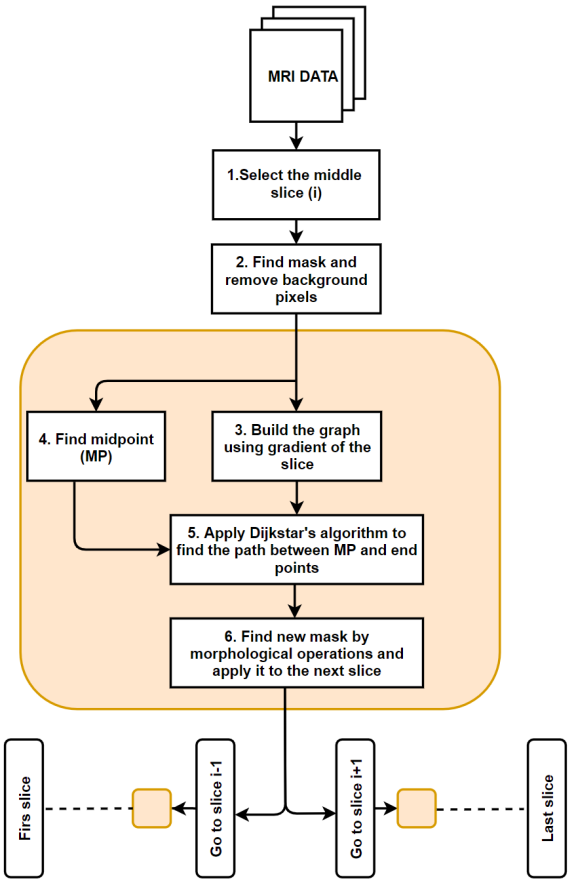


Figure 3.1: Flow diagram of the proposed algorithm.

**Step One:**

Given an anatomical T1-weighted MRI volume, as a first step, the algorithm selects its medial slice along the inferior-posterior (i.e., axial) direction. At this slice, it is often straightforward to detect the sternum, which will be used at the later processing steps.

**Step Two:**

Histogram-based segmentation is applied to the selected medial slice which results in an *approximate* segmentation mask of the breast. The main objective of the produced mask is to restrict the search space of Dijkstra's algorithm, which helps to improve the overall time efficiency of breast segmentation. To find a suitable value of the threshold, the maximum value of image histogram is used, whose largest "bin" typically represents the values of image background. Consequently, having the background value, denoted by $b_M$, the threshold is to $\tau = 1.1\, b_M$ which is a good choice for segmenting foreground from background. Furthermore, due to the effects of noise, the resulting binary mask may contain a number of disconnected components. For the purpose of the proposed method, however, only the component of largest area is kept and subsequently used.

**Step Three:**

In this step, a weighted graph $\mathcal{G} = (\mathcal{V}, \mathcal{E})$ is constructed, whose nodes $\mathcal{V}$ are associated with image pixels, whereas its edges $\mathcal{E}$ are defined based on the value of image gradient. More specifically, for each pixel (or, equivalently, a node) $x \in \mathcal{V}$, let $\mathcal{N}(x)$ denote its 8-neighbourhood. Then, for any $y \in \mathcal{N}(x)$, the edge between $x$ and $y$ is assigned a weight defined by [146]

$$W_{x,y} = \frac{1}{g(x) + g(y)} \tag{3.1}$$

where $g(x)$ and $g(y)$ represent the intensity of image gradient at pixels $x$ and $y$, respectively. To compute the values of $g$ over the entire image domain, we take advantage of steerable Gabor filtering performed at four different orientations, in which case the image gradient $g$ is set to be equal to the maximum of the absolute values of filter's outputs.

**Step Four:**

Now, the graph $\mathcal{G}$ is in hand and one can apply Dijkstra's algorithm to find the shortest path between any pair of points on $\mathcal{V}$. However, one needs to specify the starting and

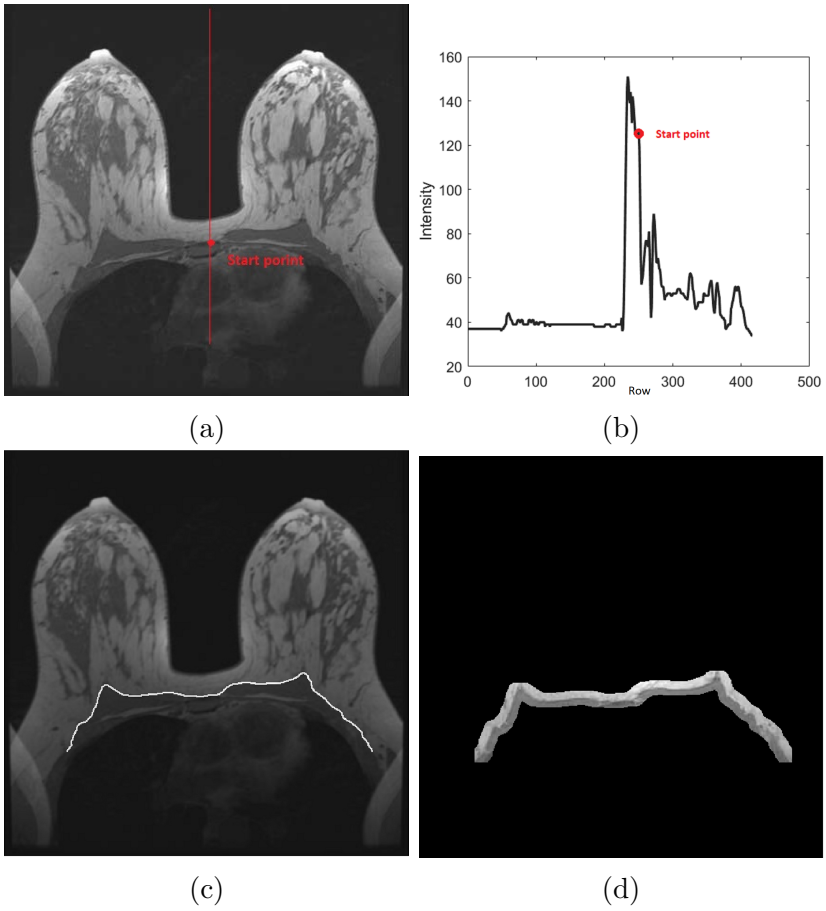


Figure 3.2: (a) Axial slice of a T1-weighted MRI volume; (b) Intensity variation of (a) along the middle column (red-line); (c) Detected pectoralis-breast boundary; and (d) Masked neighbouring slice.

end points on the graph. To this end, the starting point is chosen to be located at the sternum (see Step 1). Finding this location is usually a straightforward task in view of its homogeneous appearance due to the prevalence of adipose tissue, devoid of fibroglandular structures. Figure 3.2 (b) shows the profile of image intensity across the middle column of the medial-axial slice of a T1-weighted MRI volume. As it can be seen in this figure, the start-point $S$ (or mid-point MP in Figure 3.1) can be easily detected via following the peaks of image intensity profile (as shown by the red line in Figure 3.2 (a)).

It should be pointed out that Dijkstra's algorithm is a greedy search technique, which could result in prohibitively long processing times. To avoid this undesirable situation, the

search space of the algorithm should be restricted as much as possible. To this end, all the pixels that do not belong to the breast-body boundary need to be cropped out. In our proposed algorithm, the weights of the pixels located approximately one centimetre above the starting point are set to infinity.

Figure 3.3 shows the initial produced mask together with the computed graph. Note that, for each node in the computed graph, there are a total of eight associated weights. To visualize the computed graph, only the minimum value of these weights is shown in Figure 3.3. One can see, the graph has higher values at the nodes located relatively far from the actual boundary. Therefore, these "distant" values are excluded from the search, thus allowing Dijkstra's algorithm to detect the actual boundary much more efficiently.

**Step Five:**

In this step, Dijkstra's algorithm is used to find the minimum path between the start-point and the end-points positioned *bi-laterally*, i.e., around the left and right ends of pectoralis major. Starting at the sternum, the search is performed sequentially – first, to the left of the initial position and then to its right (or *vice versa*) – and it is terminated once the extremity of pectoral muscle is reached. To make the algorithm propagate unilaterally (i.e., towards either left or right), the weights $W_{x,y}$ are adjusted as follows. For example, to find the left pectoral end, the nodes located to the right of the starting point are blocked by setting their weights to infinity, *viz.*

$$W_{x,y} = \begin{cases} \infty, & \text{if } j_x > j_S \\ (g(x) + g(y))^{-1}, & \text{if } j_x \leq j_S \ \& \ y \in \mathcal{N}(x) \end{cases} \tag{3.2}$$

where $j_x$ and $j_S$ indicate the *column* coordinates of nodes $x$ and $S$, respectively. In this way, the algorithm is constrained to "ignore" the right breast, while being forced to propagate in the opposite direction until the left pectoral end is reached. Additionally, the algorithm can be further accelerated by preventing back-search in the direction of the starting point. With $x = (i_x, j_x)$ being the current state of the algorithm, this can be achieved by excluding from the search space the neighbouring nodes with coordinates $(i_x, j_x+1)$, $(i_x-1, j_x+1)$ and $(i_x+1, j_x+1)$, where, as before, $i_x$ and $j_x$ stand for the row and column pixel coordinates. Finally, once the left boundary is reconstructed, the algorithm is repeated along the right direction using the same numerical procedure *mutatis mutandis*. Figure 3.2(c) and Figure 3.3(d) demonstrate the examples of detected pectoral boundary for two different subjects.

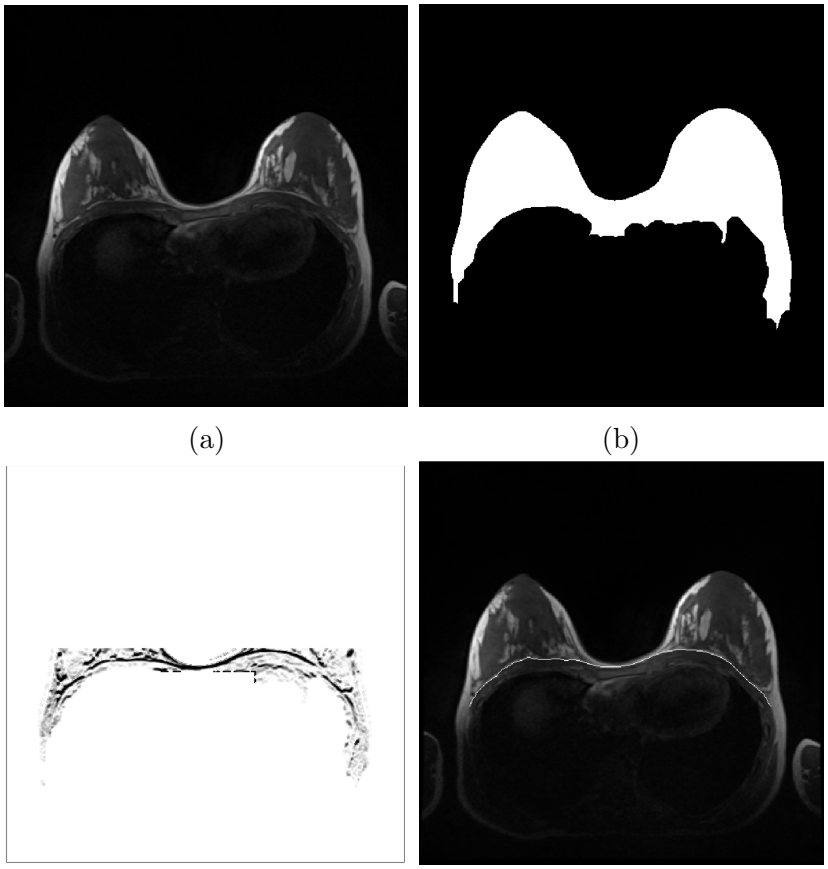

(a) (b)

(c) (d)

Figure 3.3: (a) An axial slice of a T1-weighted MRI volume; (b) Initial segmentation mask; (c) Resulting graph; and (d) Detected boundary

**Step Six:**

At the final stage, the breast-body boundary found within the medial (axial) slice is extended in both inferior and superior directions. The extension relies on the spatial correlation between adjacent (axial) slices, acquired with the slice thickness parameter set around 2 mm or less. Specifically, the 3-D reconstruction is carried out sequentially, with the final result being an aggregation of 2-D reconstructions obtained at different slices. To enforce the spatial regularity, the application of Dijkstra's algorithm at each subsequent slice is *guided* by the result obtained for its predecessor. This can be achieved by means of morphological dilation of an estimated 2-D boundary, followed by using the resulting

binary mask to define a search area for the next slice. An example of such a mask is shown in Figure 3.2(d). Although conceptually simple, the above procedure has been observed to provide stable and consistent results owing to the fact that the location of the superficial fascia at the breast-pectoralis interface does not significantly change between two consecutive slices. It also deserves noting that restricting the search area helps to limit the number of nodes "visited" by Dijkstra's algorithm, which renders the entire computational process numerically efficient.

Finally, we apply the same procedure for locating the upper boundary of the breast, the air-breast boundary. Due to the high contrast between the background and the breast, the air-breast boundary is considerably easier to find. Consequently, it is frequently possible to detect the boundary by means of less complicated edge-detection methods, e.g., adaptive thresholding. However, for higher accuracy purposes, the algorithm in Figure 3.1 was utilized to separate the breast tissue from background.

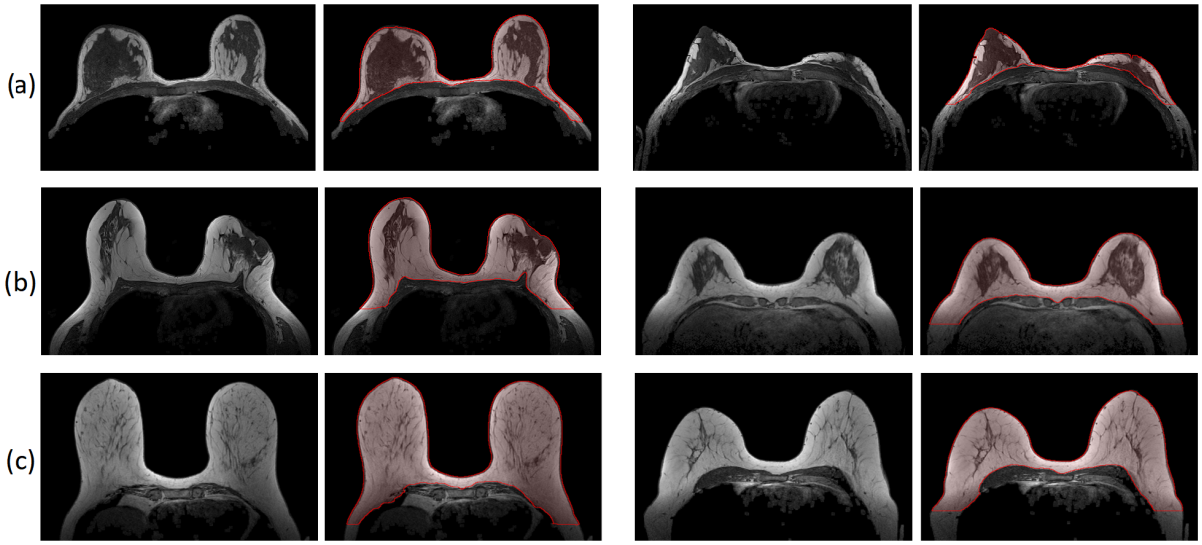


Figure 3.4: Breast segmentation results for different types of breast tissue, namely: (a) dense; (b) scattered fibroglandular; and (c) fatty

### 3.1.2 Evaluation and Results

To evaluate the performance of the proposed algorithm, a total of 20 T1-weighted volumes have been used in our experimental study. Out of these, 6 volumes (of size $512 \times 512 \times 86$)

were extracted from the publicly available Cancer Imaging Archive[1], while the remaining 14 volumes (of size $448 \times 448 \times 210$) have been acquired at the Princess Margaret Cancer Centre (Toronto, Canada) using standard (REB approved) protocols. All together, the algorithm was tested on total of 3316 slices.

The study cases have been diversified to include three different types of breast tissue, namely extremely dense, scattered fibroglandular and fatty. It should be noted that adipose tissue and pectoral muscle have considerably different T1-weighted contrasts, which makes it relatively simple to locate the body-breast boundary in fatty breasts. At the same time, the same task tends to become considerably more challenging in the case of dense breast due to the close similarity between the T1-weighted contrast of pectoralis and fibroglandular tissue. Thus, the experiments involving different types of breast tissue are critical for understanding the effect of inter-subject variability on the performance of breast segmentation. Despite the challenging nature of this experiment, however, the proposed method has been observed to be virtually invariant to the changes in breast composition. A number of representative results obtained by means of the proposed algorithm for different breast types are shown in Figure 3.4.

The proposed method has been observed to perform reliably in the case of disconnected and weak body-breast boundaries. This was expected, because if there is no clear boundary the algorithm picks a connection that minimizes the weight of the path. Thus, for instance, Figure 3.5 shows two sample slices pertaining to the cases of an extremely dense and a fatty breast. As shown in Figure 3.5(b), the proposed method detects the boundary in disconnected areas of the "dense slice" with a minimum apparent error. The same behaviour of the algorithm is demonstrated in Figure 3.5(d) for the case of fatty breast.

To evaluate the performance of the proposed method of breast segmentation in a quantitative manner, its results have been compared against the ground truth obtained by means of expert manual segmentation. The numerical comparisons have been based on a range of commonly used metrics including DSC, SEN and SPE.

Table 3.1 summarizes the performance metrics obtained using the proposed method. One can see, the method shows relatively high mean values of DSC, SEN and SPE, with relatively small values of their associated standard deviation. The mean value of each metric is the average score among all slices of volumes with the same breast type. Table 3.2 shows the performance scores obtained by means of four recent CNN-based segmentation method, which have been applied on a private dataset and reported in [118]. The mean values of DSC, SEN and SPE rates of the proposed method are above 97% for all tissue types, which is comparable with state of the art, shown in Table 3.2. In addition, the obtained results

[1]For more details visit `wiki.cancerimagingarchive.net/display/~Public/breast-diagnosis`.

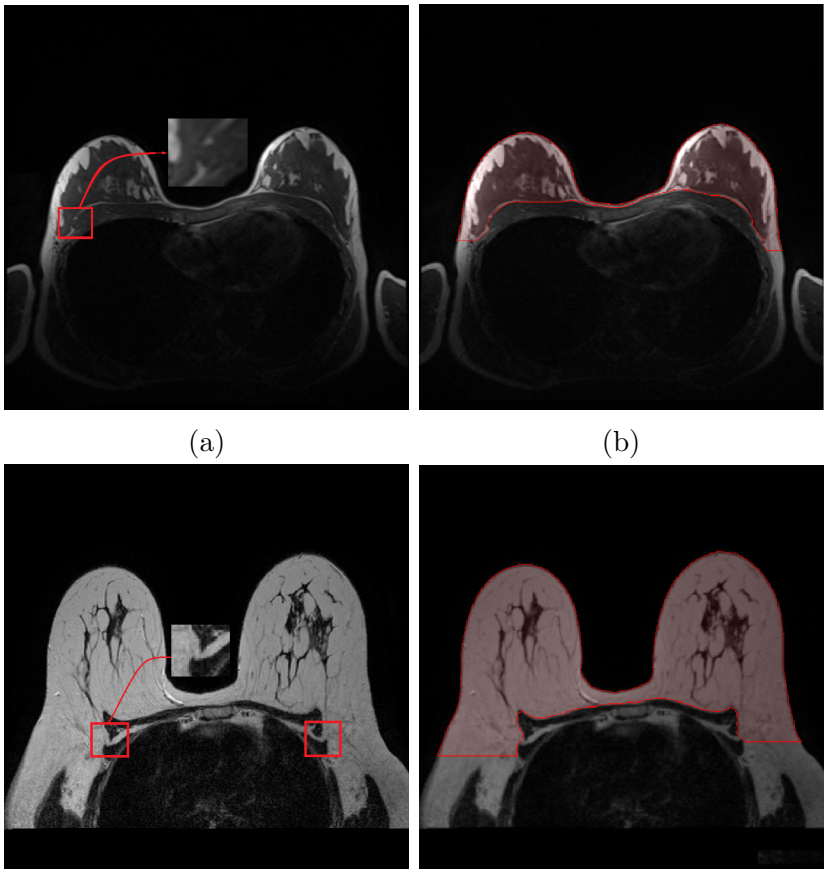

Figure 3.5: (a) An axial slice showing dense breast with disconnected boundary; (b) Detected boundary for (a); (c) An axial slice showing fatty breast with disconnected boundary; (d) Detected boundary for (c).

confirm that the performance of the proposed method does not vary significantly between different breast types, despite the visual indiscernibility of the body-breast boundary in denser breasts.

The performance of the proposed algorithm depends on finding the starting point within the medial-axial slice. However, as long as this point can be correctly localized, the algorithm is capable of finding the 3-D boundaries in a stable and consistent manner. The start-point detection procedure proposed in step four of Section 3.1.1 has been tested on other image slices. This point is detectable in more than 90% of all slices. However, this

Table 3.1: DSC, SEN and SPE scores (mean ± standard deviation) of proposed method.

| Breast type | DSC (%) | SEN (%) | SPE (%) |
|---|---|---|---|
| Dense | 97.42 ± 1.21 | 98.01 ± 0.89 | 99.12 ± 0.19 |
| Scattered dense | 98.04 ± 0.84 | 98.61 ± 0.72 | 99.47 ± 0.14 |
| Fatty | 97.86 ± 0.49 | 98.71 ± 0.41 | 99.56 ± 0.15 |

Table 3.2: DSC, SEN and SPE scores (mean ± standard deviation) of CNN-based methods.

| Method | DSC (%) | SEN (%) | SPE (%) |
|---|---|---|---|
| Multi-planar [118] | 96.60 ± 0.30 | 96.85 ± 0.47 | 99.49 ± 0.09 |
| U-Net [133] | 95.60 ± 0.34 | 96.20 ± 0.87 | 99.41 ± 0.16 |
| SegNet [5] | 95.34 ± 0.85 | 95.16 ± 0.76 | 99.44 ± 0.13 |
| V-Net [100] | 90.44 ± 3.12 | 95.14 ± 1.59 | 99.39 ± 0.19 |

point needs to be detected in the middle slice of the MRI volume, which is straightforward.

From a computational point of view, the proposed method is simple and straightforward to implement. In comparison to state of the art algorithms (which are mainly based on the use of neural networks, as in [118]), the method takes less time to complete an end-to-end breast volume segmentation. On average, it takes less than 80 seconds to process one MRI volume in MATLAB® on a standard desktop computer, without GPU acceleration.

## 3.2 Segmentation of Pectoral Muscle in Digital Mammograms

Although it is rarely seen in CC mammogram, pectoralis major often appears in MLO view, and for the purpose of an accurate alignment of breast MRI and mammogram, one needs to segment and isolate it from the breast tissue. Unfortunately, the delineation of pectoralis major in MLO mammograms is known to be a difficult problem for a number of reasons. In particular, both in terms of its morphology and contrast, the pectoral muscle can be similar to the appearance of fibroglandular tissue, which renders their delineation quite problematic. This situation is particularly frequent in the case of dense breast tissue whose fibroglandular component tends to edge near the breast-body bounding line, often overlapping (and, as a result, obscuring) the pectoral region. Moreover, due to significant inter-subject variability, the boundary of pectoralis major does not have a consistent ap-

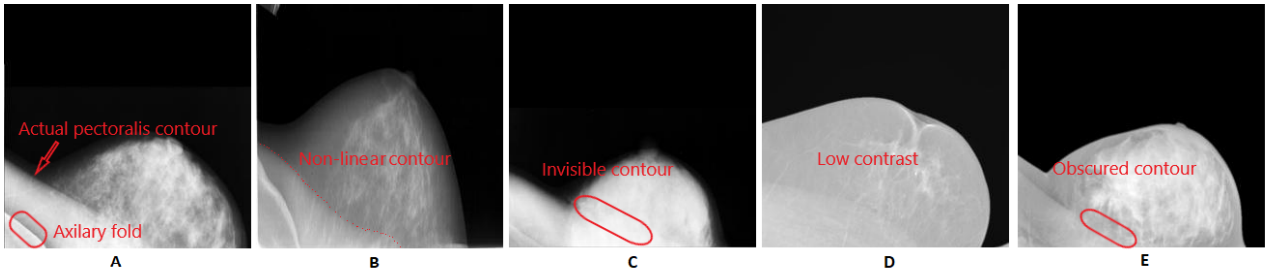


Figure 3.6: Varying appearance of the pectoral boundary due to the effects of inter-subject variability.

pearance in MLO scans, exhibiting substantial variations in shape (i.e., from quasi-linear to curved) and/or visibility due to low imaging contrast and physical occlusions (see Figure 3.6 for the examples of clinical mammograms which demonstrate the above effects). Consequently, the application of conventional methods of statistical shape analysis have shown rather limited ability to improve the accuracy of breast segmentation.

In MLO mammograms, the problem of pectoralis boundary detection has been addressed in multiple studies using a range of different approaches. In particular, there have been a group of methods based on specific *a priori* assumptions regarding the boundary geometry. Thus, for example, in [68], the boundary was approximated by a straight line, thus allowing the authors to take advantage of the Hough transform for its detection. While very efficient numerically, however, this approach suffers from the simplicity of its model assumptions, which limits its applicability in the case of curved boundaries (e.g., as shown in Subplot B of Figure 3.6). The limitations of the straight-line model have been addressed by a number of later studies, where they used the straight-line model as an initialization which was subsequently refined into a curved configuration by means of additional processing steps [34, 73, 73] and [73]. The initialization of the pectoral boundary based on the results of adaptive thresholding has been discussed by several authors as well [107, 23, 161, 172]. In particular, following the thresholding stage, the initial pectoral boundary was refined through curve fitting using least squares minimization in [161]. However, the dependence of the above methods on photometric information and low-order polynomial modelling makes them overly sensitive to the appearance (visibility) of the pectoral muscle. As a result, their performance may still deteriorate dramatically when the pectoral boundary is either visually indiscernible or obscured by dense tissue, which is a common effect of tissue folding.

Among the most recent methods of pectorlis muscle segmentation are also those based

on the ideas and tools of DL, and specifically CNN, which offer conceptually new possibilities to tackle this problem. Subsequently, several studies aimed at designing the CNN architectures which were specifically tailored to the problem at hand. Among such works, the most promising results have been demonstrated in [31, 102, 128]. More specifically, in [31, 102], the CNNs were trained using image blocks (i.e., mini patches) extracted from the pectoral region, thus taking into account the structural appearance and photometric properties of the pectoral muscle. Despite the promising results reported by these two studies, their output segmentation maps still suffered from the effects of false positive misclassification. To overcome this problem, it was proposed in [128] to subject the output of CNN-based classification to a post-processing stage involving morphological operations. It is worthwhile noting that, in its first stage, the method relied on a modified version of the hierarchical edge detection (HED) network of [168] which is capable of integrating the information on the location of pectoral edges across multiple resolution scales.

It should be pointed out that, the last few years have seen a rapid development of edge detection CNNs which are capable of detecting both fine- and course-scale representations of various geometric structures in data images (such as, e.g., edges, ridges, etc.) [81, 80, 122]. The main idea of these methods is to produce edge maps in different resolution scales, followed by fusing the obtained information to yield the final result. However, while very effective for reducing uncertainties (due to imaging artefacts and the effects of noise), the process of fusion is not without drawbacks, chief of which is often attributed to the excessive thickness of resulting edges [122]. This could be a serious disadvantage in the case of breast segmentation, in which case the edges are required to be as fine as possible. To overcome some of the drawbacks of existing algorithms, a new approach was proposed to the problem of pectoralis-breast boundary detection which will be explained in the next section.

### 3.2.1 Proposed Approach

Similar to earlier works, our solution relies on a two-stage processing scheme. The first stage uses a modified version of the VGG16 network architecture [141]. The introduced modification restricts the analysis to two resolution levels and, as a result, it has the important advantage of depending on a relatively small number of network parameters which are substantially easier to train. Moreover, the proposed architecture proves to be sufficient to encode all the relevant information about the pectoral boundary, with the course level pinpointing its anatomical location (with virtually no "false positives") and the fine level following its true configuration at a much higher resolution. Although the fine resolution map remains prone to numerous misclassification errors, the latter are effectively

eliminated by the fusion process, yielding an accurate initialization for the second stage of the proposed algorithm. At this stage, we construct a weighted graph and take advantage of Dijkstra's algorithm to locate the pectoralis boundary at a *single-pixel* resolution (thickness). Below, these steps are discussed in detail.

**CNN-based Edge Detection:** Our designed CNN architecture is mainly based on the principles of edge detection networks proposed recently in [168, 81, 80, 122]. In particular, all these methods take advantage of multiple CNNs which correspond to different resolution levels and are optimized using different numbers of training images. The backbone of these models is formed by the convolutional blocks of VGG16 architecture, where edge maps are generated from each block resulting in a multi-scale learning structure. Thus, for example, the HED network of [168] exploits a total of five convolutional blocks, taking a side-output from each of them. Subsequently, the outputs are integrated by a fusing block producing the final edge map. Note that each of the convolutional blocks as well as the fusing block are optimized using different cost functions (i.e., a total of six in the case of [168]), which requires a relatively large number of training samples.

In the above-mentioned HED network, the edge (probability) maps are computed at different resolution levels, resulting in edge estimates of variable thickness. In this case, the final estimate produced by the process of fusion may not always reduce the edge thickness to a single-pixel resolution [122]. In addition, aforementioned CNN-based models have been designed to capture the complex edges in natural images. However, our aim is to find only the boundary of the pectoralis major and neglect other possible edges in MLO mammograms. This can be achieved using a simplified network architecture (with a substantially reduced number of training parameters), as explained next.

To produce a thin-edge map and make the current edge-detection networks simpler, using VGG16 as the base of the network, we designed a new architecture. VGG16 consists of three fully connected layers and 13 *convolutional* layers which are subdivided into five stages, and after each stage a pooling layer is connected. The fifth stage was excluded and all the fully connected layers were cut, resulting in a simplified design depicted in Figure 3.7.

Contrary to most edge detection networks and the method in [128], instead of taking 5 side outputs and fusing them, we only take two side outputs from stages 2 and 4, and leave them unfused (which makes the network simpler). *Convolutional* layers of stages 2 and 4 are connected to a *convolutional* layer with kernel size $1 \times 1$ and depth 11. Note that in the original VGG16, the depth size is 21 and in our work is is reduced to 11 (which was set experimentally) in order to create a network with less complexity. Feature maps produced

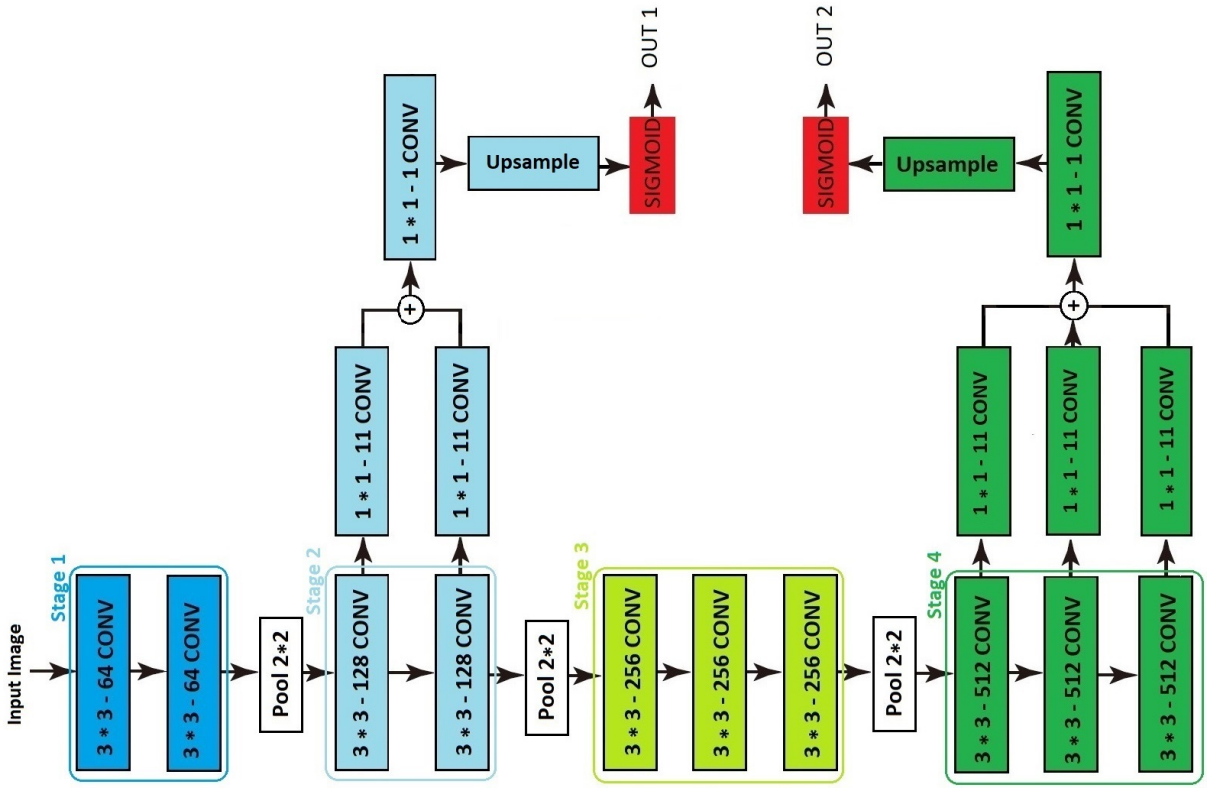


Figure 3.7: Proposed CNN architecture for pectoral boundary detection.

in each stage are accumulated and passed to another *convolutional* with size $1 \times 1$ and depth 1. Eventually, these feature maps are up-sampled to the size of the input image and passed to a sigmoid function to produce the probability edge-maps. Linear interpolation is used to do up-sampling. In the second phase of the algorithm, these two probability maps can be subsequently used to locate the pectoralis muscle.

The proposed network was trained and tested using three public datasets, namely MIAS [152], InBreast [104], and CBIS-DDSM [76]. MIAS and CBIS-DDSM consist of 322 and 457 scanned film mammograms, respectively, of different image sizes. The InBreast dataset, on the other hand, consists of 208 FFDM of size $2560 \times 3328$. To create the reference edge labels (i.e., $Y$), all the mammograms have been manually annotated by a qualified radiologist. Both data mammograms and their related edge maps were subsequently resized to a standard dimension of $256 \times 256$ pixels. Appendix A.1 provides details of the training procedure of the network.

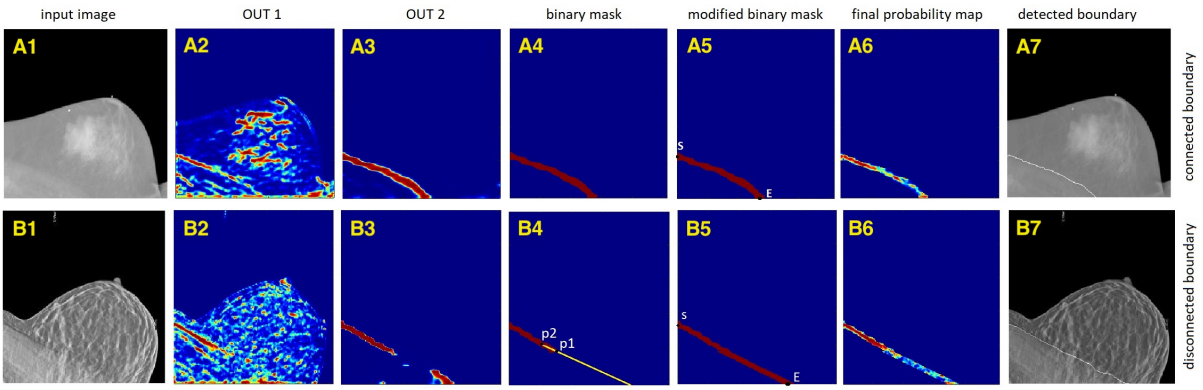


Figure 3.8: Upper row of subplots: (A1) input MLO mammogram; (A2) edge probability map OUT 1; (A3) edge probability map OUT 2; (A4) binary mask $B$; (A5) modified binary mask; (A6) final edge probability map; and (A7) the result of graph-based edge detection. Subplots B1-B7 are composed in an analogous manner, corresponding to a different input image shown in Subplot B1.

The produced edge probability maps from stage 2 (OUT 1) and stage 4 (OUT 2) are shown for two sample MLO mammograms in Figure 3.8 (Subplots A2-A3 and B2-B3). Note that the probability maps are depicted in pseudo-colour, with the values of 0 and 1 represented by the blue and red colours, respectively.

**Detection of Pectoral Boundary:** As it is shown in Figure 3.8, the edge map constructed in OUT 1 is thinner with respect to that of the OUT 2, but it suffers from a substantially larger amount of clutter noise due to the network's response to the dense structures of breast tissue. Fusing these two probability maps may result in a thin edge map with no (or less) false positives. To this end, first the binary mask $B$ is generated by hard thresholding the probability map of OUT 2. Subsequently, $B$ is subjected to morphological pruning that retains the longest connected component of $B$, which is normally associated with the pectoral boundary. Note that, as opposed to the majority of earlier approaches, the pruning step does not rely on any *a priori* assumptions regarding the orientation of pectoral muscle.

For numerical convenience, all the images have been reoriented so as to position the pectoral region at the low-left corner of the image coordinate system (as shown in Figure 3.8). As a result, the opposite ends of pectoral boundary had been constrained to lie on the first column and the last row of $B$, respectively (as shown in Subplots A4 and B4 of Figure 3.8).

Unfortunately, the numerical procedure described above has one critical limitation. In particular, it has been assumed that the longest connected component of $B$ coincides with the pectoral boundary *along its entire length* (as illustrated by Subplot A4 in Figure 3.8). Unfortunately, there are situations in which this component can be disconnected (as exemplified in Subplot B4 of the same figure). Therefore, it is necessary to recover the missing parts of the contour in the probability map. This problem can be overcome by means of simple linear extrapolation. In particular, suppose the edge indicated by $B$ is disconnected on the right and, as a result, its terminating point $p_1$ falls short of reaching the boundary of the image domain, as depicted in Subplot B4 of Figure 3.8. The point $p_1$ can be defined by the (right) endpoint of the morphological skeleton of the partial edge. Furthermore, following the same skeleton (starting at $p_1$), one can define another point $p_2$, lying at a predefined arc-length distance $\mathcal{D}$. In the course of our experimental study, the value of $\mathcal{D} = 25$ was found to provide stable and consistent results.

Finally, the skeletal points within the interval defined by $p_1$ and $p_2$ can be fit by a line segment, which can, in turn, be used to complete the partial edge (see the illustration in Figure 3.8). In the present study, the fitting was based on a standard LS formulation. Also, the thickness of the completing part of the edge was set to be equal to the average thickness of its initial segment. The result of edge completion is shown in Subplot B5 of Figure 3.8. Needless to add, the above considerations pertain to only one possible scenario, while in practice, the edge incompletion problem may arise on either or both sides of the longest connected component of $B$. In such cases, the edge completion can be done in an analogous way *mutatis mutandis*.

In the end, given the binary mask $B$ (which could have been modified through the above described edge completion procedure, if necessary), the final edge probability map $M$ can be defined to be the result of element-wise product of $B$ with OUT 1. Formally,

$$M = B \odot \text{OUT 1},$$

where $\odot$ denotes the element-wise (Hadamard) product between two equally-sized matrices.

The computation of $M$ concludes the first phase of the proposed method. At the next stage, $M$ is used to resolve the breast-body interface at a single-pixel resolution. To this end, $M$ can first be converted to a symmetric, weighted, fully-connected graph $\mathcal{G}(V, E)$, with $V$ and $E$ denoting the nodes and edges of the graph, respectively. Eventually, given two points $S$ (for "start") and $E$ (for "end") on the opposite sides of pectoralis, its boundary can be closely approximated by the *shortest path* on $\mathcal{G}$ that connects $S$ and $E$. These points are shown in subplot A.6 and B.6 of Figure 3.8. More details of finding the shortest path from $S$ to $E$ can be found in Appendix A.2.

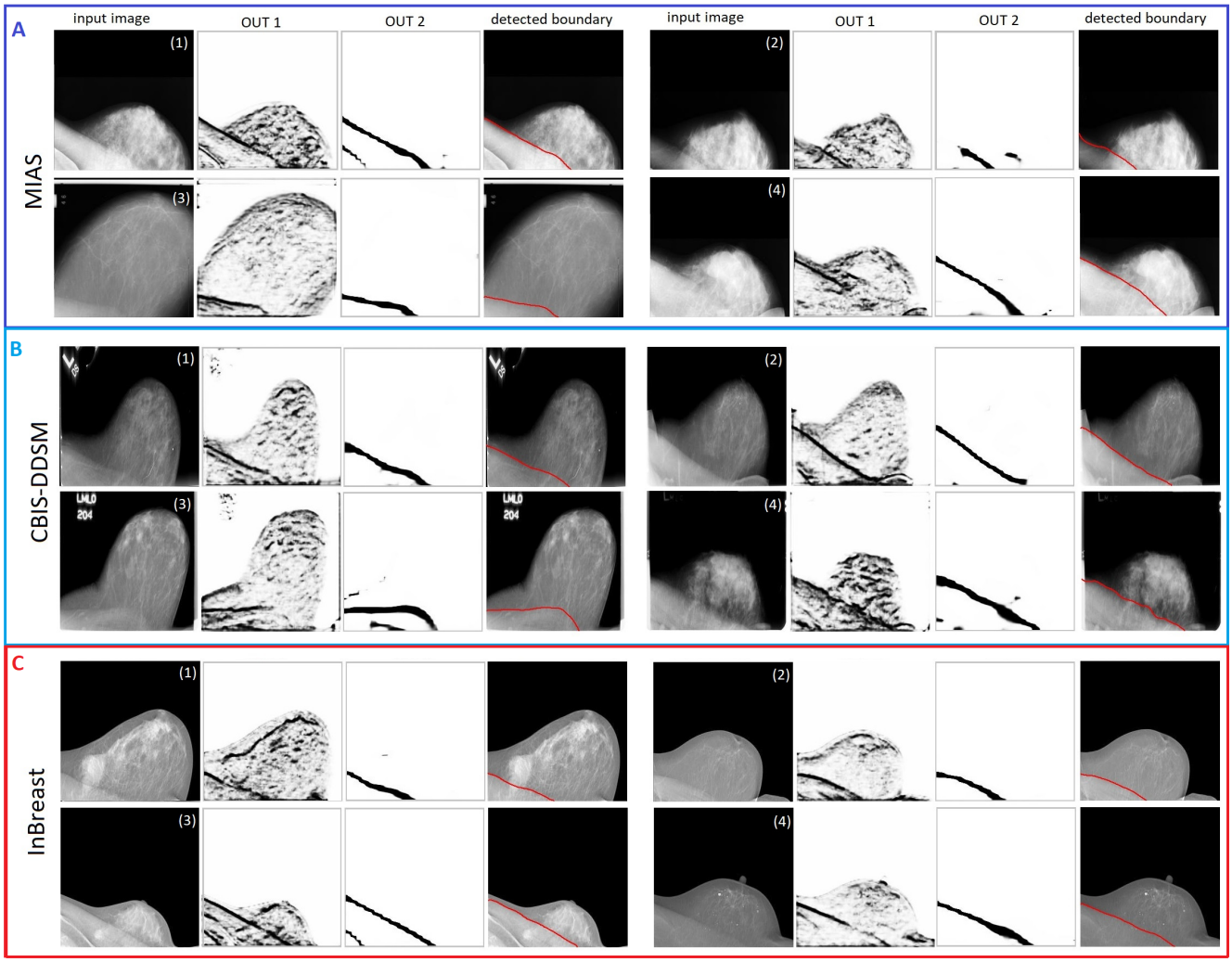


Figure 3.9: **Panel A**: Four examples of pectoral boundary detection showing MLO mammograms (Subplots 1-4) from the MIAS dataset along with their associated OUT1, OUT2, and detected boundary (shown in the red colour); **Panel B**: same as A, only for the CBIS-DDSM dataset; **Panel C**: same as A, only for the InBreast dataset.

### 3.2.2 Evaluation and Results

As it was mentioned earlier, the proposed method for breast segmentation has been tested on three public datasets (MIAS [152], InBreast [104] and CBIS-DDSM [76]), containing both scanned film and digital mammograms acquired from different subjects under various

settings.

The three panels in Figure 3.9 show the results of detection of the pectoral boundary, where each panel consists of four examples pertaining to the MIAS (Panel A), CBIS-DDSM (Panel B) and InBeast (Panel C) datasets. In addition to input images and boundary reconstructions, Figure 3.9 also shows their associated OUT1 and OUT2. One can see that the largest values of OUT2 are indeed localized in a close proximity of the true pectoral boundary, thereby guaranteeing the final probability map $M$ to be free of outliers (false alarms) due to the clutter noise in OUT1. One can also notice that the detection results remain consistent with respect to underlying anatomy even in the cases of low-contrast and/or incomplete observations (as depicted, e.g., in Subplots 2 & 4 of Panel A, Subplots 1 & 3 of Panel B or Subplots 1 & 4 of Panel C). Moreover, the proposed method has demonstrated outstanding robustness to the presence of axillary foldings, which is another common source of artefacts impeding the process of breast segmentation (see, e.g., Subplots 1, 2, and 3 in Panels A, B, and C, respectively).

Once the pectoral boundary is recovered, all pixels being below this boundary are set to '1' which results in a binary image (pectoralis mask) showing the pectoral muscle region. For the purpose of quantitative analysis, the quality of pectoralis mask has been assessed in terms of a number of performance metrics. Assuming $R$ and $R_G$ denote an estimated mask of pectoralis major and its ground truth counterpart, the performance metrics included: 1- DSC, 2-JAC, 3- SPE, 4- SEN, 5- ACC, 6- FPR and 7- FNR.

While adopting the above metrics, it is important to keep in mind some of their principal characteristics. In particular, better performance is associated with higher values of DSC, FNR, SPE, SEN and ACC and lower values of FPR and FNR. At the same time, DSC and JAC measures are known to be more sensitive in comparison to the other metrics (such as, e.g., ACC and SPE) [128], while JAC and DSC are known to be less sensitive to visual errors. Note that highly sensitive and highly specific algorithms rarely overlook the target they are looking for and they rarely mistake anything else for that specific target.

Table 3.3 summarizes the results of our comparative analysis by showing the mean values of the metrics (expressed in %) plus/minus one standard deviation. One can see that, in all the cases, the values of DSC, FNR, SPE, SEN and ACC remain above 93%, while the values of FPR and FNR are close to zero. The worst results have been observed with the InBreast dataset, with DSC=% 96.39, JAC=93.17% and FNR=5.6%. It has to be noted, however, that this dataset predominantly contains MLO mammograms with poorly defined pectoral boundaries, which are far from trivial to detect in general. At the same time, the algorithm's performance on the MIAS and CBIS-DDSM datasets has been found to be comparable (with DSC>97.6%, JAC>95.3%, SPE& ACC>99.5%, along with

Table 3.3: Comparison results for three database. All metrics are presented in % by their mean value ± one standard deviation.

| Metric | MIAS | CBIS-DDSM | InBreast |
|---|---|---|---|
| DSC | 97.59±1.73 | 97.69 ± 1.51 | 96.39 ± 2.66 |
| JAC | 95.35±3.20 | 95.52 ± 2.79 | 93.17 ± 4.79 |
| SPE | 99.83 ±0.22 | 99.73 ±0.34 | 99.92 ±0.15 |
| SEN | 97.76±2.27 | 98.66 ± 1.74 | 94.39 ± 3.77 |
| ACC | 99.72 ±0.22 | 99.51±0.35 | 99.69±0.25 |
| FPR | 0.16 ± 0.22 | 0.26 ± 0.34 | 0.07 ± 0.15 |
| FNR | 2.23 ± 2.27 | 2.33 ± 1.74 | 5.60 ± 4.61 |

FNR<2.5% and FPR<0.3%).

The comparison between our algorithm with the state of the art can be found in Appendix A.3.

## 3.3 Segmentation of Breast MRI

Segmenting breast tissue into adipose and fibroglandular classes is the other preprocessing task that should be done before registration. The problem of segmentation of breast MRI scans have been addressed in several studies using different approaches, such as thresholding-based and gradient-based image segmentation, active contours, machine learning and others [126]. Thus, for example, an adaptation of the fuzzy c-means method with a specially designed kernel was proposed in [67], while a solution to the problem of segmentation of dermal and fibroglandular tissue by means of k-means clustering was described in [111]. An alternative use of the fuzzy c-means method, resulting in an adaptive and semi-automatic algorithm for segmentation of fibroglandular and adipose tissue, was introduced in [110]. In [117], a similar idea of semi-automatic segmentation was realized based on the method of region growing. Unfortunately, the manual selection of seed points as well as the relatively high computational complexity of this method somewhat weaken its otherwise excellent performance. The recent proliferation of the theory and tools of DL has substantially expanded the possibilities of image segmentation as well. Thus, for example, a particular architecture of deep neural networks (specifically CNN), known as U-net, was used to segment fibroglandular and adipose tissues in [133]. However, that the performance of CNNs usually improves *pro rata* with the size of training sets (e.g., manually segmented

MRI scans, in the case at hand). Thus, generalizing DL-based methods to a wide range of different densities and geometries of the breast could be potentially problematic.

When searching for relatively simple yet robust methods of segmentation of breast MRI scans, statistical methods based on use of *mixture models* deserve special noting. In particular, the assumption on image values to obey a Gaussian Mixture Model (GMM) was exploited in [52, 45]. In this case, the GMM model is typically fitted by means of the Expectation Maximization (EM) algorithm [27], properly modified to account for spatial dependencies between same-class labels (using, e.g., the Markov Random Field model [45]).

For relatively high values of signal-to-noise ratio (SNR), the GMM is known to provide an adequate approximation of the probability distribution of breast MRI scans. At low SNR, however, the quality of this statistical model is known to plummet, causing notable segmentation artefacts. To resolve this problem, we consider the use of *Rician* Mixture Modeling (RMM) [48], which is known to be a more natural and accurate statistical description in the case of MRI. To avoid dealing with the generally complex nature of RMM fitting, we introduce a simple "gaussianization" procedure which effectively reduces the Rician case to a Gaussian one. Moreover, the proposed method can explicitly account for the effect of bias fields [65], ultimately leading to a straightforward optimization problem. The latter is shown to admit a computationally efficient solution, which can be found in just a few iterations.

### 3.3.1 Proposed Approach

To set the notations, let $\Omega \in \mathbb{R}^3$ be a volumetric image domain over with an MRI scan $F : \Omega \to \mathbb{R}^3$ is assumed to be defined. The scan $F$ is also assumed to be contaminated by a bias field $B : \Omega \to \mathbb{R}$, the effect of which is usually considered to be multiplicative. Consequently, in the absence of other artefacts and noises, the corresponding observed image $G$ could be modeled as

$$G(\mathbf{r}) = F(\mathbf{r})B(\mathbf{r}), \quad \mathbf{r} \in \Omega. \tag{3.3}$$

In practical settings, $G$ is always contaminated by Rician noise, which leads to a relatively complex analysis in the presence of $B$. To simplify the model, one can redefine (3.3) in the logarithmic domain as

$$g(\mathbf{r}) = \mathcal{R}_{\mathcal{L}}\left\{f(\mathbf{r}) + b(\mathbf{r})\right\}, \quad \mathbf{r} \in \Omega, \tag{3.4}$$

with $g$, $f$ and $b$ standing for $\log G$, $\log F$ and $\log B$, respectively, and with $\mathcal{R}_{\mathcal{L}}\{\cdot\}$ being a symbolic representation of the effect of the log-transformed Rician noise. The latter can

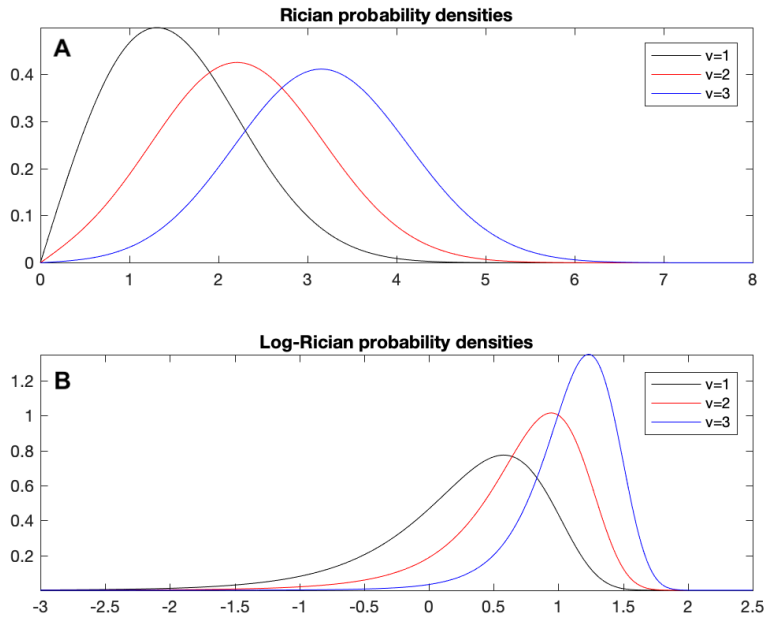


Figure 3.10: (Subplot A) Rician probability densities $\mathcal{R}(x\,|\,\sigma,\nu)$ for $\sigma = 1$ and $\nu = 1,2,3$; (Subplot B) Corresponding log-Rician densities $\mathcal{R}_{\mathcal{L}}(y\,|\,\sigma,\nu)$, with $y = \log x$.

be shown to behave similarly to a Gaussian noise, except for the presence of occasional "spikes", which can be attributed to the relatively large mass of the left-side tail of a log-Rician distribution. In its Subplot A, Figure 3.10 depicts some examples of Rician probability densities $\mathcal{R}(x\,|\,\sigma,\nu)$ for $\sigma = 1$ and $\nu = 1,2,3$. Note how the shapes of the densities transform from asymmetric to Gaussian-like as $\nu$ increases. Subplot B of the same figure, on the other hand, shows the corresponding log-Rician probability densities $\mathcal{R}_{\mathcal{L}}(y\,|\,\sigma,\nu)$ (with $y = \log x$). Note that, for all $\nu$, the densities have a Gaussian-like appearance, with the exception of their heavy left tail.

Clearly, dealing with the log-Rician noise offers few advantages over the Rician case, unless the former is properly "gaussianized" so that $\mathcal{R}_{\mathcal{L}}\{f(\mathbf{r}) + b(\mathbf{r})\}$ can be approximately replaced with $f(\mathbf{r}) + b(\mathbf{r}) + u(\mathbf{r})$, where $u(\mathbf{r})$ obeys a Gaussian distribution. Note that such "gaussianization" should, in fact, be able to suppress the impulsive component of the log-Rician noise. Such a result can be achieved by means of the procedure of *outlier shrinkage* as given by

$$g(\mathbf{r}) \mapsto g(\mathbf{r}) - \mathcal{S}_{\lambda}\{g(\mathbf{r}) - \bar{g}(\mathbf{r})\}, \quad \forall \mathbf{r} \in \Omega, \tag{3.5}$$

where $\bar{g}$ stands for a median-filtered version of $g$[2], while $\mathcal{S}_\lambda$ denotes the operator of soft thresholding given by

$$\mathcal{S}_\lambda(z) = \min(z + \lambda, 0) + \max(z - \lambda, 0),$$

where $\lambda > 0$ is a predefined threshold value.

The action of outlier shrinkage is straightforward. With the original image $f$ being a piece-wise smooth function and $b$ being a smooth field, the residuals $g - \bar{g}$ can be reasonably assumed to be dominated by noise. When subjected to soft thresholding, the noise retains its largest values which are likely to be associated with its impulsive ("spiky") component. Subsequently, the latter is subtracted from $g$, thus making the residual noise to behave in a nearly Gaussian manner.

Despite its conceptual and computational simplicity, the procedure of outlier shrinkage has demonstrated considerable efficacy for properly set values of $\lambda$. In this work, the latter has been set to be equal to two times the median absolute deviation of the residual $g - \bar{g}$ [77].

**Two-class segmentation model:** The anatomy of the breast is relatively complex. However, when it comes to the T1 contrast, which is typically used in breast MRI, there are two main tissue classes that are usually targeted by image segmentation algorithms. These classes correspond to fibroglandular and adipose tissue, which is referred below as the dense and fat tissues, respectively[3]. Accordingly, in what follows, the problem of image segmentation will be formulated for a two-class scenario. In this case, the objective of image segmentation becomes to partition the domain $\Omega$ into two mutually exclusive subdomains $\Omega_d$ and $\Omega_f$ (with $\Omega = \Omega_d \cup \Omega_f$ and $\Omega_d \cap \Omega_f = \varnothing$) associated with the dense and fat tissues, respectively. Such a partition can, in turn, be described in terms of an *partition function* $\xi : \Omega \to \{0, 1\}$ given by

$$\xi(\mathbf{r}) = \begin{cases} 1, & \mathbf{r} \in \Omega_d \\ 0, & \mathbf{r} \in \Omega_f \end{cases} .$$

Consequently, the problem of image segmentation can be equivalently formulated as a problem of estimation of function $\xi$.

One way to formulate the above estimation problem is by taking advantage of the effect of outlier shrinkage, which guarantees the residual noise contaminating $g$ is approximately additive white Gaussian noise. In this case, it seems reasonable to assume the class-conditional probability densities $p(g(\mathbf{r}) \,|\, \mathbf{r} \in \Omega_d)$ and $p(g(\mathbf{r}) \,|\, \mathbf{r} \in \Omega_f)$ to be Gaussian with

[2]In practical computations, a $3 \times 3$ median filter has proven to be an adequate choice.

[3]In the absence of contrast enhancement, dermal and tumorous tissues have a visual appearance similar to that of dense tissue . For this reason, tumors are often included in the "dense" class .

their means equal to $\mu_d + b(\mathbf{r})$ and $\mu_f + b(\mathbf{r})$, respectively. Under this assumption, the problem of estimation of $\xi$ can be expressed as an optimization problem of the form

$$\min_{\xi,\mu_d,\mu_f,b} \left\{ \lambda_d \sum_{\mathbf{r}\in\Omega} \xi(\mathbf{r}) |g(\mathbf{r}) - \mu_d - b(\mathbf{r})|^2 + \lambda_f \sum_{\mathbf{r}\in\Omega} (1 - \xi(\mathbf{r})) |g(\mathbf{r}) - \mu_f - b(\mathbf{r})|^2 \right\}$$
$$\text{s.t. } \xi(\mathbf{r}) \in \{0, 1\}, \ \forall \mathbf{r} \in \Omega, \tag{3.6}$$

for some regularization parameters $\lambda_d, \lambda_f > 0$. It is important to emphasize that, in (3.6), both $\mu_d$ and $\mu_f$ as well as the bias field $b$ are treated as optimization variables, similarly to $\xi$.

The problem defined by (3.6) is a non-convex integer optimization problem, a solution to which would have been quite difficult to find in general. To overcome this difficulty, one can try to "relax" the problem by letting the values of $\xi(\mathbf{r})$ be anywhere within the interval $[0, 1]$ (instead of being trapped at either 0 or 1), while restricting the optimal $\xi^*$ to the class of piece-wise smooth functions. This can be accomplished by minimizing the value of the *total variation* (TV) semi-norm of $\xi$ that is given by

$$\|\xi\|_{\text{TV}} = \sum_{\mathbf{r}\in\Omega} |\nabla\xi(\mathbf{r})|,$$

where $\nabla\xi$ denotes the (discrete) gradient of $\xi$ and $|\nabla\xi(\mathbf{r})|$ stands for its magnitude at position $\mathbf{r}$. Consequently, the resulting minimization problem acquires the following form [105]

$$\min_{\xi,\mu_d,\mu_f,b} \left\{ \lambda_d \sum_{\mathbf{r}\in\Omega} \xi(\mathbf{r}) |g(\mathbf{r}) - \mu_d - b(\mathbf{r})|^2 + \lambda_f \sum_{\mathbf{r}\in\Omega} (1 - \xi(\mathbf{r})) |g(\mathbf{r}) - \mu_f - b(\mathbf{r})|^2 + \right.$$
$$\left. + \|\xi\|_{\text{TV}} + I_{[0,1]}(\xi) \right\}, \tag{3.7}$$

where $I_{[0,1]}$ stands for the indicator function of the closed interval $[0, 1]$ that is given by

$$I_{[0,1]}(z) = \begin{cases} 0, & 0 \le z \le 1, \\ \infty, & \text{otherwise} \end{cases}.$$

Additionally, one can also take advantage of the fact that, in practice, the bias field $b$ is a smooth slowly varying function, which can approximated by a polynomial of a relatively low order. Specifically, let $\{\phi_k\}_{k=0}^K$ be a set of polynomials of orders $0, 1, \ldots, K$. Then, with $\Phi_{i,j,k}(\mathbf{r}) = \Phi_{i,j,k}(x, y, z) = \phi_i(x)\phi_j(y)\phi_k(z)$, the bias field $b$ can then be approximated as

$$b(\mathbf{r}) = \sum_{i=0}^{K} \sum_{j=0}^{K} \sum_{k=0}^{K} c_{i,j,k} \Phi_{i,j,k}(\mathbf{r})$$

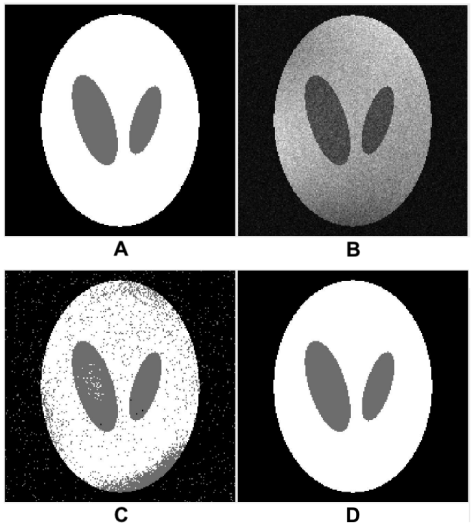


Figure 3.11: (A) Cross-sectional slice of a 3-D phantom; (B) Same slice contaminated by a bias field and Rician noise; (C) Segmentation obtained using the GMM-based method of [105]; (D) Segmentation obtained using the proposed method.

or, more concisely, as $b(\mathbf{r}) = \Phi(\mathbf{r})c$. Consequently, the problem of estimation of the bias field $b$ can be reduced to the equivalent problem of estimation of its polynomial coefficients $c \in \mathbb{R}^{(K+1)^3}$. In this case, the optimization problem (3.7) becomes

$$\min_{\xi,\mu_d,\mu_f,c} \left\{ \lambda_d \sum_{\mathbf{r}\in\Omega} \xi(\mathbf{r})|g(\mathbf{r}) - \mu_d - \Phi(\mathbf{r})c|^2 + \lambda_f \sum_{\mathbf{r}\in\Omega} (1-\xi(\mathbf{r}))|g(\mathbf{r}) - \mu_f - \Phi(\mathbf{r})c|^2 + \right. \\ \left. + \|\xi\|_{\mathrm{TV}} + I_{[0,1]}(\xi) \right\}. \tag{3.8}$$

In this work, to define $\Phi(\mathbf{r})$, Bernstein polynomials have been used [85]. This choice is by no means exclusive, and alternative definitions of polynomial bases could have been used instead. Numerical solution of (3.8) is provided in Appendix B.

### 3.3.2 Evaluation and Results

The performance of the proposed method for segmentation of breast MRI scans has been tested using both phantom and real-life data. In the former case, a 3-D version of the Shepp-Logan phantom has been used as a model of the breast, while in the latter case we

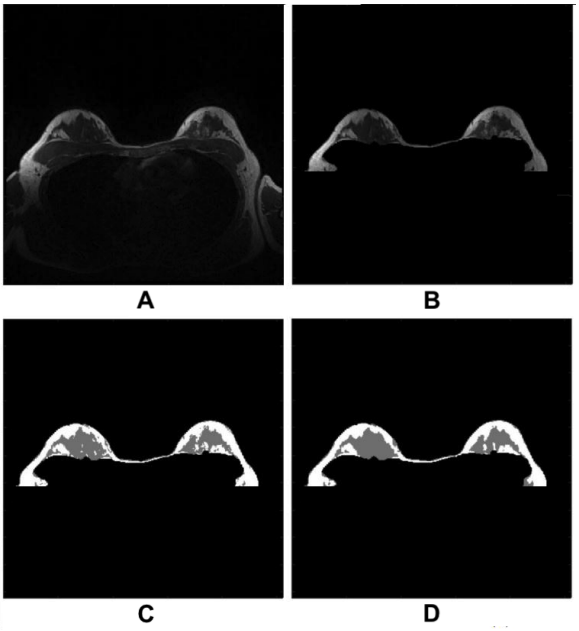


Figure 3.12: (A) Axial slice of a 3-D breast MRI volume; (B) Same slice contaminated by a bias field and Rician noise; (C) Segmentation obtained using the GMM-based method of [105]; (D) Segmentation obtained using the proposed method.

used the breast MRI scans acquired with a 3T Signa$^{TM}$ Premier MRI scanner (GE Healthcare, Inc.) at the Princess Margaret Cancer Center (Toronto, Canada). As a reference method, the GMM-based algorithm of [105] has been used.

Some representative results produced by the reference and proposed methods are shown in Figure 3.11 and Figure 3.12 corresponding to the case of *in silico* and *in vivo* experiments, respectively. One can see that the Gaussian model is incapable of adequately capturing the nature of Rician noise, resulting in erroneous segmentation. The proposed method, on the other hand, has been able to produce valuable results at low SNR and in the presence of sizable bias.

Moreover, using the phantom data allowed us to compare the performance of the reference and proposed methods in a quantitative way. As a figure of merit, we used the DSC, which its values are distributed between 0 and 1, with the latter corresponding to the case of perfect segmentation.

The quantitative comparisons have been performed at different levels of SNR and bias field contamination. Table 3.4 demonstrates the obtained results for a representative set

of SNR values. One can see that, in all these cases, the proposed method outperforms the reference segmentation by a substantial margin.

## 3.4 Conclusion

In this chapter, we discussed the details of three preprocessing steps which are necessary for an accurate breast MRI to mammogram registration. First, using Dijkstra's algorithm a fully automatic and computationally efficient method of whole-breast segmentation was introduced. Based on the fact that neighbour slices of MRI scans are strongly correlated, the detected boundary in each slice was used as a guide to find the breast boundary in adjacent slices. This recursive organization of estimation process renders the algorithm efficient, fast, and reliable, as supported by a series of experimental results performed on clinical MRI volumes. The performance of the proposed method has been demonstrated to remain nearly independent of breast type, which constitutes a significant improvement over existing methods of breast segmentation.

Second, we illustrated the use of a simplified CNN architecture combined with a graph search technique in locating the breast-pectoralis boundary in MLO mammograms. In view of its limited description power (as a result of using a substantially smaller number of network parameters), the proposed CNN is not expected to produce the final result, but rather to provide reliable initialization for the second part of post-processing that takes advantage of Dijkstras's algorithm to complete the task. The proposed two-step reconstruction of the pectoralis mask is advantageous in a number of ways. First, the use of CNN eliminates the need for analytical assumptions regarding the geometry of pectoral boundary, which are prone to errors due to the effects of inter-subject variability. Consequently, the CNN-based processing remains stable and consistent across a variety

Table 3.4: Quantitative comparison of the reference and proposed methods.

| SNR(in dB) | DSC (reference method) | DSC (proposed method) |
|---|---|---|
| 6.6 | 0.86 | 0.97 |
| 7.0 | 0.65 | 0.94 |
| 7.4 | 0.65 | 0.91 |
| 7.8 | 0.69 | 0.95 |
| 12.0 | 0.86 | 0.97 |
| 12.3 | 0.79 | 0.97 |

of different pectoral anatomies, imaging contrasts, and image acquisition methods (e.g., scanned film vs digital mammography). Furthermore, the subsequent use of graph-based processing allows one to recover the pectoral boundary at a single-pixel resolution in a fully automatic way as well.

Finally, a new method of segmentation of breast MRI scans has been described. A principle attribute of the method is its formulation in the logarithmic domain in conjunctions with proper "gaussianization". It has been shown that such preprocessing allows one to substantially simplify the problem of image segmentation, leading to a computationally efficient numerical solution that remains accurate and stable for a wide range of values of SNR as well as in the presence of sizable bias fields.

# Chapter 4

# Breast MRI to Mammography Registration

Due to their dependence on different contrast mechanisms breast MRI and X-ray mammogram images provide different trade-offs in terms of the sensitivity and specificity of their respective findings. For this reason, fusing the informational content of MRI scans and digital mammograms has been considered to be a promising means to achieve improved diagnostics of breast malignancies. Such fusion, however, entails spatial alignment of the mammographic and MRI scans, which is known to be a difficult estimation problem – not only that the scans are acquired under different physical conditions, but also they have disparate contrasts and dimensionality. To this end, earlier studies depended on complex, subject-specific bio-mechanical modelling to predict the breast deformation due to paddle compression. In this chapter, we propose a different framework, in which the total breast deformation is split to global and residual components. The global component is the substantial part of the deformation which is almost independent of the breast tissue properties, and it is common among all subjects. In this chapter, we will discuss two computationally simple approaches to estimate the global deformation. Additionally, this deformation estimation is refined by computing the residual deformation by taking the advantages of FFD model. The residual deformation is patient-specific and requires to take into account the breast properties, e.g., the ratio of adipose and fibroglandular voxels.

## 4.1 Problem Formulation

Let $f$ be a 3-D MRI volume in a Left-Anterior-Superior (LSA) orientation, defined over a rectangular domain $\Omega \in \mathbb{R}^3$. In addition, let $\Omega_{2D}$ be a 2-D plane within $\Omega$ defined as $\Omega_{2D} = \{(x, y, z) \in \Omega \mid z = 0\}$, which will serve as the domain of definition for a 2-D mammogram image $g$ related to $f$. For the sake of generality, in what follows, $f$ and $g$ will be replaced by their transformed versions $\mathcal{I}_f(f)$ and $\mathcal{I}_g(g)$, respectively, where $\mathcal{I}_f$ and $\mathcal{I}_g$ denote two intensity transformations to be specified later in this chapter.

Given $f$, its corresponding "simulated mammogram" can be obtained by radiographically projecting $\mathcal{I}_f(f)$ onto $\Omega_{2D}$. In this work, the projection amounts to integrating the image along its $z$-coordinate according to

$$\mathcal{P}\{\mathcal{I}_f(f)\} = \int_z \mathcal{I}_f(f(x, y, z))\, dz. \tag{4.1}$$

Note that the projection relies on the assumption of parallel rays, which seems to be reasonable given the fact that, in most mammographic settings, the source-to-plane distance is usually greater than breast thickness by an order of magnitude. It should also be noted that the above projection corresponds to the case of a CC view (which will be extended to MLO projections in the next section).

Central to this work is the assumption that $f$ and $g$ are related by a geometric transformation accounting for the change in the anatomical posture as well as the effect of paddle compression. Formally, this transformation can be defined as a map $\varphi : \Omega \to \Omega$. Consequently, one can define the "simulated mammogram" of $f$ as $\mathcal{P}\{\mathcal{I}_f(f) \circ \varphi\}$, which allows comparing it against $\mathcal{I}_g(g)$ in terms of a predefined similarity measure $\mathcal{S}$ [176]. In this case, the problem of estimating $\varphi$ can be cast into an optimization framework, where its optimal value is recovered as a solution to

$$\max_{\varphi \in \Phi} \mathcal{S}\Big(\mathcal{P}\{\mathcal{I}_f(f) \circ \varphi\}, \mathcal{I}_g(g)\Big), \tag{4.2}$$

where the maximization is performed over all transformations $\Phi$ deemed to be admissible (such as, e.g., topology preserving mappings [106]).

As mentioned in the introduction, directly estimating $\varphi$ is rarely possible. Instead, the proposed solution seeks for an optimal deformation of the form

$$\varphi_{\text{total}} = \varphi_{\text{res}} \circ \varphi_{\text{glb}}, \tag{4.3}$$

where, as before, the $\circ$ symbol stands for functional composition. In (4.3), $\varphi_{\text{glb}}$ is used to model the large-magnitude global component of the total deformation $\varphi_{\text{total}}$, while $\varphi_{\text{res}}$

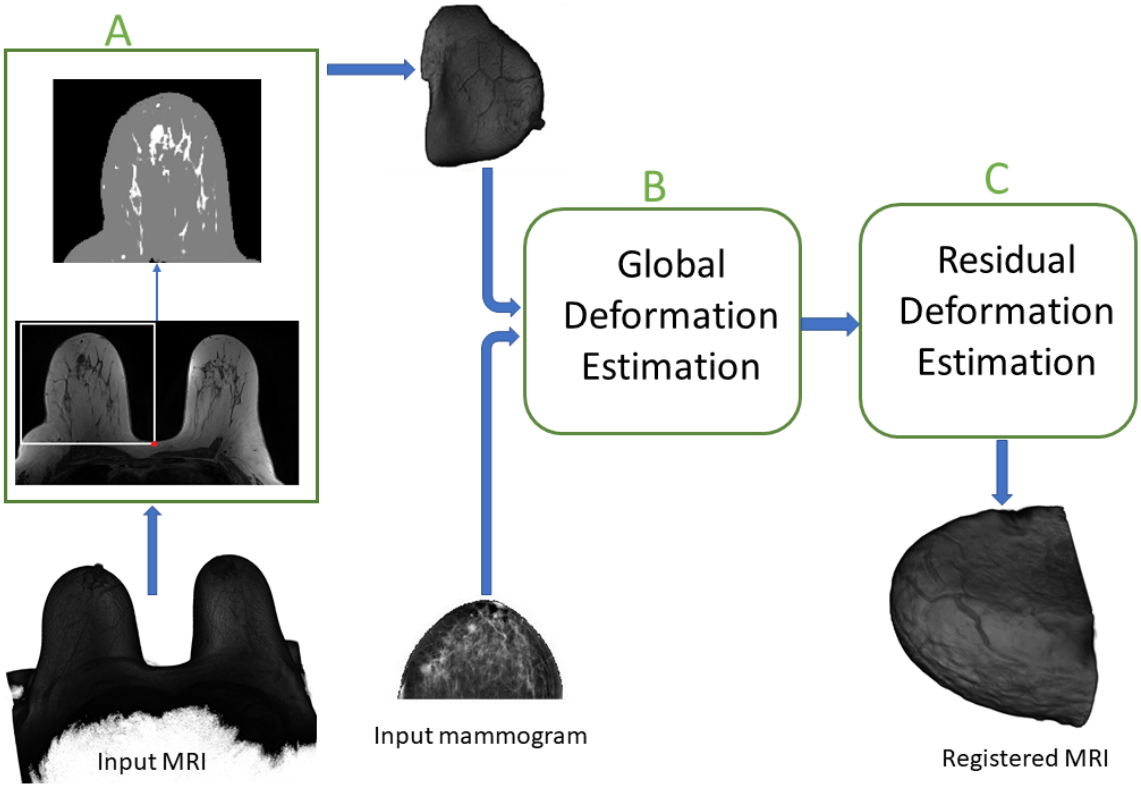


Figure 4.1: Block diagram of the proposed method: (A) preprocessing step which includes geometry extraction and breast tissue segmentation in MRI images; (B) Estimation global deformation; and (C) Computation of residual deformation by using the advantages of FFD.

stands for a residual deformation of a relatively smaller magnitude (i.e., $\|\varphi_{\text{res}}\| \ll \|\varphi_{\text{glb}}\|$). In this work, the similarity $\mathcal{S}$ is maximized as a function of $\varphi_{\text{res}}$ alone, whereas $\varphi_{\text{glb}}$ is replaced by its *predicted* value $\hat{\varphi}_{\text{glb}}$. Consequently, the final estimate is obtained as $\hat{\varphi}_{\text{res}} \circ \hat{\varphi}_{\text{glb}}$, with

$$\hat{\varphi}_{\text{res}} = \arg\max_{\varphi_{\text{res}} \in \Phi} \mathcal{S}\Big(\mathcal{P}\{\tilde{f} \circ \varphi_{\text{res}}\}, \tilde{g}\Big), \tag{4.4}$$

where $\tilde{f} := \mathcal{I}_f(f) \circ \hat{\varphi}_{\text{glb}}$ and $\tilde{g} := \mathcal{I}_g(g)$. The rest of this chapter provides details on computing the prediction $\hat{\varphi}_{\text{glb}}$ as well as the computation of $\hat{\varphi}_{\text{res}}$ using (4.4). The overall structure of the proposed method is depicted in Figure 4.1.

## 4.2 Data preprocessing

In general, breast MRI volumes acquired in a supine position contain an abundance of unnecessary information on the nearby anatomy of the chest wall. Thus, cropping the volumes to retain their relevant portion alone constitutes the first step in MRI to mammogram registration [59]. In the supine position, when the breast is unrestricted and pendulous, one can isolate it from the rest of the chest wall by means of a *coronal* separating plane which is constrained to pass through the anterior end of sternal body (as shown by the red dot in Subplot A of Figure 4.1). Note that, since mammographic paddles are typically propped against the sternum, the breast anatomy represented by the cropped MRI volumes and their respective mammograms can be reasonably assumed to be nearly the same.

As the next step, the cropped MRI volumes need to be prepared for their alignment with mammogram scans. In the case of CC mammograms, the direction of paddle compression and radiographic projection coincides with the $z$-axis, which precludes the breast from free rotation around the coordinate axes. In the case of MLO mammograms, on the other hand, the paddles are rotated around the $y$-axis through a predefined roll angle (around 45°), whose value is usually known[1]. Moreover, during the examination, the subject's position is further optimized by adding an in-plane rotation around the $z$-axis, usually in the range between 15° and 30°. Consequently, in the case of MLO, the process of cropping the MRI volumes has been preceded by their rotation through both of the above angles (with the in-plane rotation set to 20° [96]).

As it was discussed in the previous chapter, as a preprocessing step, one needs to isolate breast tissue from nearby tissues, particularly pectoralis muscle. To exclude this muscle both from MLO mammograms as well as from their related MRI scans, our proposed solutions in Sections 3.1 and 3.2 were applied.

Finally, to resolve the problem with the discrepancy between different imaging contrasts, two different approaches to the definition of intensity transformations $\mathcal{I}_f$ and $\mathcal{I}_g$ have been investigated. In the first case, the latter is set to be an identity (i.e., $\mathcal{I}_g(g) = g$), while $\mathcal{I}_f$ is defined following the method proposed in [40]. In particular, at each voxel $\mathbf{r} = (x, y, z)$, let $P_a(\mathbf{r})$ and $P_d(\mathbf{r})$ be the posterior probabilities of its value to be associated with the class of adipose and dense tissue, respectively[2], so that $P_a(\mathbf{r}) + P_d(\mathbf{r}) = 1$. The adipose and dense classes, in turn, can be associated with their corresponding (average) attenuation coefficients $\mu_a(E)$ and $\mu_d(E)$, which depend on the X-ray energy level $E$. Thus,

[1] This and other relevant information is standardly included in the header of DICOM files.

[2] Following [40], the dense component of breast tissue is assumed to consist of both its fibro-glandular fraction and possible tumorous neoplasms [64].

an *effective attenuation* coefficient $\mu_{\text{eff}}$ at $\mathbf{r}$ can be defined as given by

$$\mu_{\text{eff}}(\mathbf{r}, E) = \mu_a(E)P_a(\mathbf{r}) + \mu_d(E)P_d(\mathbf{r}).$$

Consequently, given the attenuation coefficients of water ($\mu_{\text{water}}(E)$) and air ($\mu_{\text{air}}(E)$), the intensity transformation $I_f$ can be defined as [40]

$$\mathcal{I}_f(f(\mathbf{r})) = \sum_{E=0}^{kVp} \omega(E) \frac{\mu_{\text{eff}}(\mathbf{r}, E) - \mu_{\text{water}}(E)}{\mu_{\text{water}}(E) - \mu_{\text{air}}(E)}, \tag{4.5}$$

where $kVp$ stands for the end-point energy, while $\omega(E)$ denotes the energy spectrum of the anode material (which is normally available).

The main idea behind using (4.5) is to convert an MRI volume $f$ into a "pseudo-X-ray" volume $\mathcal{I}_f(f)$, whose projected values have an intensity distribution close to that of a mammographic scan. In this way, the transformation makes it possible to use computationally simpler similarity measures to solve (4.4), as it will be shown later.

Another approach to defining $\mathcal{I}_f$ and $\mathcal{I}_g$ is due to [57]. In this case, $\mathcal{I}_f(f(\mathbf{r})) = P_d(\mathbf{r})\,\Delta z$, with $\Delta z$ denoting the MRI resolution in the direction of projection. It is important to note that $P_d$ can be viewed as a "soft" segmentation mask of the dense tissue. Hence, the projected values of $P_d\,\Delta z$ are expected to represent the physical *thickness* of the latter in the direction of mammographic projection.

The above definition of $\mathcal{I}_f$ requires a proper adaptation of $\mathcal{I}_g$, which should now reflect the thickness of the dense tissue in $g$. To this end, assuming the latter is given in a raw (linear) format, let $g_a$ be equal to the average value of $g$ corresponding to its regions dominated by fat. Then, the intensity transformation $\mathcal{I}_g$ can be defined to be the mammographic density of the dense tissue as given by [57]

$$\mathcal{I}_g(g(x, y)) = \frac{\log(g(x, y)) - \log(g_a)}{\mu_a - \mu_d}. \tag{4.6}$$

The use of (4.6) requires the knowledge of $g_a$, which could be hard to compute in mammographically dense scenarios. In this case, an alternative way of computing $g_a$ can be based on the fact that the total (physical) volume of the dense tissue should be equal in both MRI and its related mammogram. Consequently, an optimal value of $g_a$ can be adjusted empirically until the above equality is reached. Figure 4.9 shows an example of CC mammograms with their respective transformed counterparts.

Concluding this section, it should also be noted that both approaches to the definition of $\mathcal{I}_f$ require segmentation of an MRI volume $f$ into two classes, namely adipose and

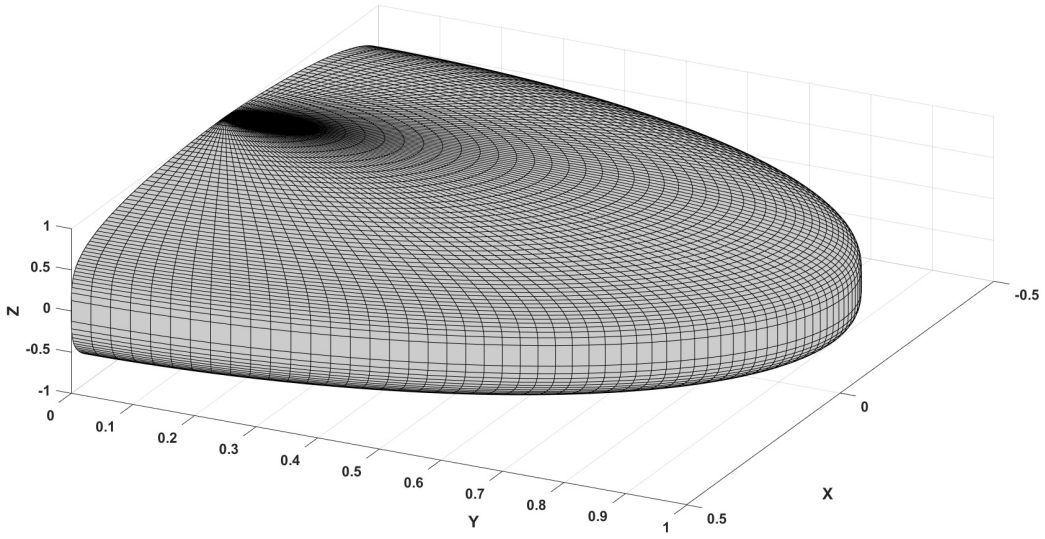


Figure 4.2: Super-quadratic with $a = 0.6$, $b = 1$, $c = 1$, $t = 4$ and $r = 2$, $s = 2$ $(0 \leq y)$

dense. Although standard in breast MRI analysis, such segmentation is known to be a difficult problem, especially in the presence of bias fields. In the present work, the proposed approach in Section 3.3 was used that is capable of dealing with practical noises and common imaging artefacts, while offering the advantage of straightforward and efficient implementation. This being said, however, our choice of the segmentation method is by no means binding, and other algorithms could have been used instead as well.

In the rest of this chapter, we introduce two different approaches for global deformation ($\varphi_{\text{glb}}$) estimation along with details of computing the residual deformation ($\varphi_{\text{res}}$).

## 4.3 Global Deformation Estimation by Superquadratic Function Model

According to (4.3), the total deformation $\varphi_{\text{total}}$ is assumed to consist of a composition of $\varphi_{\text{glb}}$ and $\varphi_{\text{res}}$. While the second component is estimated based on imaging information, the first is predicted from the breast geometry. It is important to emphasize that, in the above model, the principal function of $\varphi_{\text{glb}}$ is to account for the massive displacement of breast tissue in response to mammographic compression. It is therefore not as important for a predicted $\varphi_{\text{glb}}$ to be as close as possible to $\varphi_{\text{total}}$ as to make sure that the residual

deformation is sufficiently small (and, thus, amiable for accurate numerical estimation). A common way to compute such predictions has been through the use of complex, subject-specific bio-physical modelling by means of FEM. However, considering the global nature of $\varphi_{\text{glb}}$, its prediction can be computed based on a much simpler computational procedure, as explained below.

The global deformation of the breast during mammographic compression has many properties and characteristics which appear to be common to subjects within different breast geometry and composition. Thus, in particular, the boundary of a compressed breast can be closely approximated by a super-quadratic ([7]) of the form

$$\left|\frac{x}{a}\right|^r + \left|\frac{y}{b}\right|^s + \left|\frac{z}{c}\right|^t = 1, \quad y \geq 0, \tag{4.7}$$

where the $x$, $y$ and $z$ coordinates are aligned with the left-right, posterior-anterior and inferior-superior directions, respectively. Note that the condition $y \geq 0$ is added to keep the anterior part of the surface only. The parameter $\theta = \{a, b, c, r, s, t\}$ controls the shape of the super-quadratic and, hence, needs to be properly defined. Figure 4.2 shows the shape of resulted super-quadrics for $a = 0.6$, $b = 1$, $c = 1$, $r = 2$ and $s = 2$, $t = 4$ ($0 \leq y$). As it can be seen, the shape looks like a breast tissue which is compressed between two mammographic paddles. Therefore, one can use this function and roughly model the breast deformation by tuning $a, b, c, r, s$ and $t$.

To this end, it has been noticed that the projection of the super-quadratic onto the $(x, y)$ plane is described by a simplified equation of the form $|x/a|^r + |y/b|^s = 1$. This shape can be reasonably expected to be aligned with the mammographic boundary of the breast. Thus, one can find parameters ($a$, $b$, $r$ and $s$) by fitting the above equation to the points in the boundary of X-ray mammogram. We first extract the boundary of the breast from the mammogram, and then find these parameters by feeding it to a heuristic optimization algorithm, Teaching Learning-Based Optimization [129]. Then, the objective function was defined as

$$\mathfrak{f}(a, b, r, s) = \sum_{x_i, y_i \in \mathcal{A}} \left(1 - \left(\left|\frac{x_i}{a}\right|^r + \left|\frac{y_i}{b}\right|^s\right)\right)^2 \tag{4.8}$$

where $\mathcal{A}$ is the boundary of breast tissue in the mammogram and $\{(x_i, y_i)\}_{i=1}^K$ are the coordinates of the points located on the boundary of the mammogram. Figure 4.3 shows a sample fitted super-quadratic function in 2-D ($x - y$ plane).

To estimate the remaining parameters of the super-quadratic (i.e., $c$ and $t$), we use the fact that information about the distance between compression paddles is always indicated

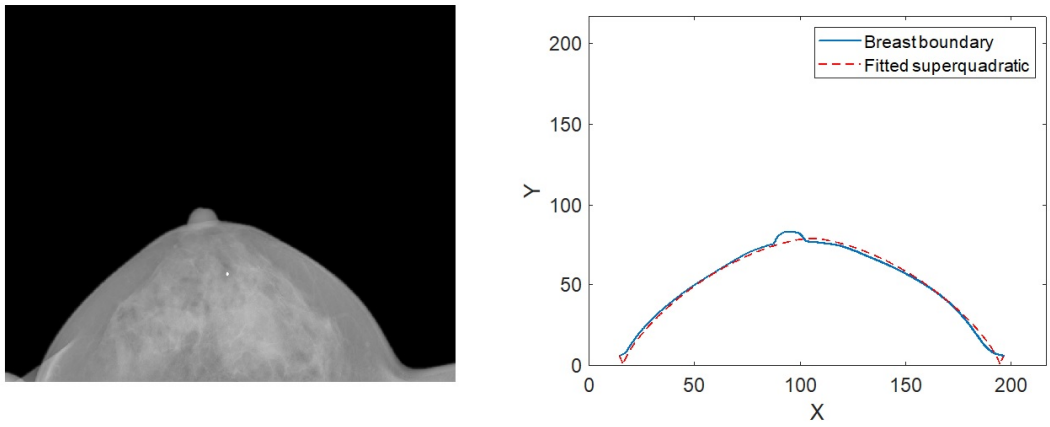


Figure 4.3: Fitting super-quadratic function to boundary of mammogram: (a) Sample mammogram; (b) Fitted super-quadratic curve to the boundary of mammogram in (a)

in the header of mammography files[3]. Consequently, denoting this distance by $h$, it is straightforward to see that $c = h/2$. Finally, to estimate $t$, the compression is assumed to be volume preserving [97]. Thus, given an estimate of the breast volume derived from the 3-D MRI, one can simply find a value of $t$ yielding a super-quadratic (4.7) of equal volume.

Given the original boundary of the breast (as observed in MRI scans) and its referenced "compressed" boundary (as represented by the fitted super-quadratic), the final step in estimation of $\varphi_{\text{glb}}$ consists of finding a spatial transformation that aligns these surfaces. Note that, in practical computations, the surfaces are represented by sets of discrete point coordinates. Consequently, in this work, we took advantage of the Coherent Point Drift (CPD) point registration algorithm [108], which is a set-point registration technique allowing one to determine a spatial transformation that brings the two sets of discrete (surface) points into close correspondence with each other. This method was chosen for the convenience and simplicity of its algorithmic structure that requires neither preprocessing nor special initialization.

In the CPD algorithm, the alignment of two point clouds is formulated as a probability density estimation problem, and centroids (representing the first point cloud) are fitted to the data (the second point cloud) by maximizing the likelihood. GMM centroids move coherently as a group to preserve the topological structure of the set-points. The

[3]The value of $h$ is a standard attribute of mammogram data which is designated as "breast thickness" in DICOM nomenclature.

transformation is defined as the initial position plus a displacement field $v$,

$$\mathcal{T}(\mathbf{r}, v) = \mathbf{r} + v(\mathbf{r}) \tag{4.9}$$

The norm of $v$ is used as a regularizer to guarantee the smoothness of the transformation. This suggests that the points that are close to one another tend to move coherently. The expectation Maximization (EM) algorithm is used to find the parameters of the transformation. The algorithm starts with choosing the initial values of the parameters which is known as the E-step. The parameter values are then updated in the M-step, where the expectation of the complete negative log-likelihood function is minimized.

A fast implementation of this algorithm, reducing the method computation complexity to linear, is publicly available [4]. This code was used to find the transformation field between surfaces. To apply set-point registration, we uniformly sampled around 2000 points to 3000 points from each surface. Results showed that CPD algorithm suits our problem and can easily handle noise and outliers, specifically points on the nipple. Figure 4.4 (a) shows the result of point registration, and as it can be seen, the nipple in the MRI surface has been considered as noise.

It should be noted that the above method of surface registration can only be used to predict the motion of the boundary points, while remaining oblivious to what happens inside the breast mass. To overcome this problem, one can extrapolate the boundary motion *inside* the breast volume by means of Thin Plate Spline (TPS) interpolation [12]. Note that this type of interpolation is guaranteed to find a spatial transformation of minimum possible bending energy, which agrees well with the general tendency of soft biological tissue to deform in the most "ergonomic" way. Subplots (b) and (c) of Figure 4.4 provide an illustration of the above-described process.

The proposed method for estimating $\varphi_{\text{glb}}$ does not take into consideration the actual composition of breast tissue, effectively assuming it to be homogeneous. As a result, it would be unreasonable to expect $\varphi_{\text{glb}}$ thus obtained to be sufficient to explain the real displacement. This brings us to the problem of estimation of the residual transformation $\varphi_{\text{res}}$, which is detailed in next sections.

[4] www.bme. ogi.edu/~myron/matlab/cpd.

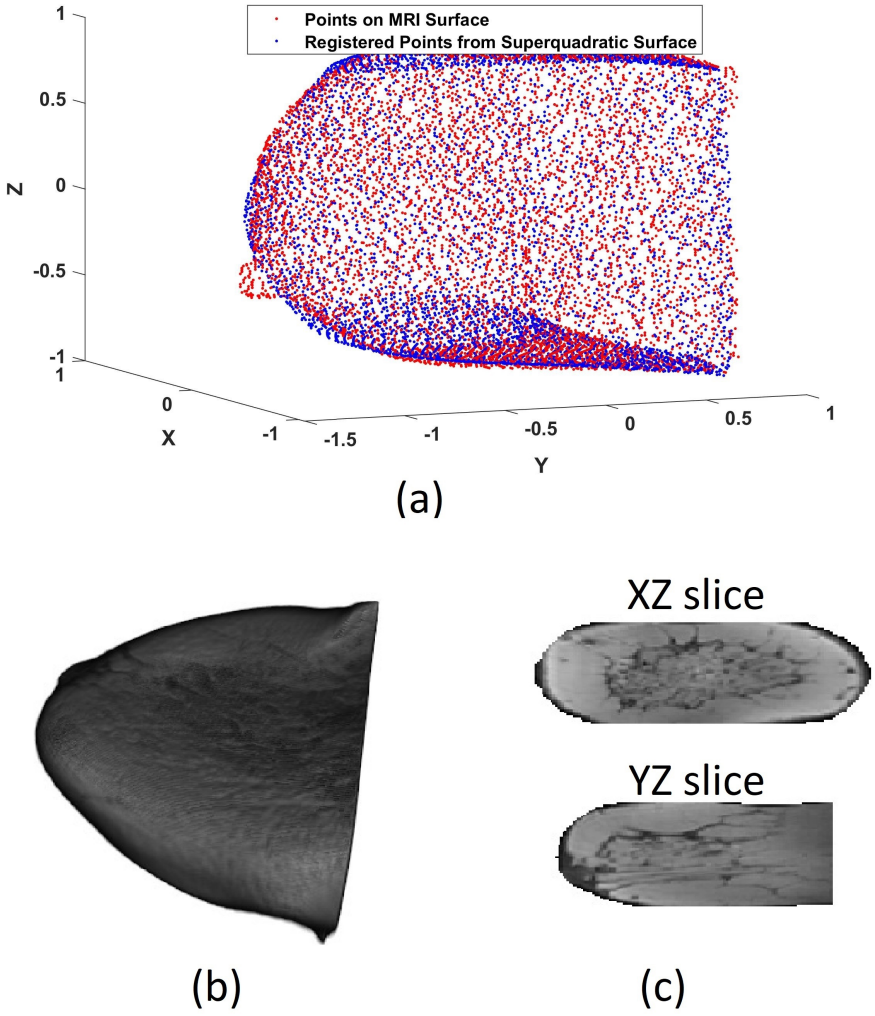


Figure 4.4: MRI deformation using CPD: (a) Registered points of the surfaces of MRI and simulated superquadratic; (b) Deformed MRI (shown in Figure 4.3 (b)); (c) Sample slices of deformed MRI.

## 4.4 Estimation of Global Deformation by Temporal Evolution of Breast Surface

As an alternative method for estimating the global deformation, a new numerical approach was developed. The principal idea is rooted in the observation that, due to the large

magnitude of compression forces and the intrinsic softness of breast tissue, the shape of a mammographically deformed breast mainly depends on its initial geometry rather than its internal properties. Consequently, a useful prediction of $\varphi_{\text{glb}}$ can be derived from the apparent deformation of the breast boundary due to compression. In the present work, this deformation is emulated by means of the *Clip-And-Restore* (CAR) procedure which is detailed below.

As its input, the CAR procedure uses the breast boundary which can be extracted directly from $f$. The boundary can be represented by the zero level-set $\Gamma_0$ of a Lipschitz-continuous function $\psi : \Omega \to \mathbb{R}$, so that $\Gamma_0 = \{\mathbf{r} \in \mathbb{R}^3 \mid \psi(\mathbf{r}) = 0\}$. In particular, it is common to define $\psi$ to be the Signed Distance Function (SDF) of the breast boundary, with its values being positive inside the breast region, while being negative outside [112]. Such SDF has the following properties:

$$\begin{cases} |\nabla\psi(\mathbf{r})| = 1, & \forall \mathbf{r} \in \mathbb{R}^3 \\ \psi(\mathbf{r}) = 0, & \forall \mathbf{r} \in \Gamma \\ \psi(\mathbf{r}) > 0, & \forall \mathbf{r} \in \text{ interior of } \Gamma \\ \psi(\mathbf{r}) < 0, & \forall \mathbf{r} \in \text{ exterior of } \Gamma \end{cases}$$

with $\nabla\psi$ standing for the gradient of $\psi$ and $|\nabla\psi(\mathbf{r})|$ being its magnitude at $\mathbf{r}$.

Assuming, as before, that the compression forces are applied along the caudal-cranial direction, let $z_0^{\min}$ and $z_0^{\max}$ be the minimum and maximum value of the $z$-coordinate of $\Gamma_0$. To emulate the process of mammographic compression, we use a pair of *virtual paddles* located at $z_0^{\min}$ and $z_0^{\max}$, respectively, with their surfaces parallel to the $(x, y)$ plane (as shown in Figure 4.6). Note that, in such an arrangement, the breast region is guaranteed to be confined to the spatial "slab" $\{(x, y, z) \mid z_0^{\min} \le z \le z_0^{\max} \;\&\; y \ge 0\}$, where the points with $y = 0$ are assumed to be aligned with the chest wall. Figure 4.5 illustrates the initial configuration of the breast and the virtual paddles.

As its name suggests, the CAR procedure consists of two steps – clipping and restoring – which are initiated with $\Gamma_0$, $z_0^{\min}$, $z_0^{\max}$ and performed iteratively until a termination condition is reached. In this way, the procedure yields a sequence of breast boundaries $\Gamma_0, \Gamma_1, \Gamma_2, \ldots$, closely converging to the breast boundary at the end of compression.

**Clipping:** The purpose of clipping is to emulate the movement of mammographic paddles by a small increment $\Delta_c$ towards each other. At iteration $k$, this amounts to redefining the paddle positions as

$$z_k^{\min} \leftarrow z_{k-1}^{\min} + \Delta_c/2, \quad z_k^{\max} \leftarrow z_{k-1}^{\max} - \Delta_c/2.$$

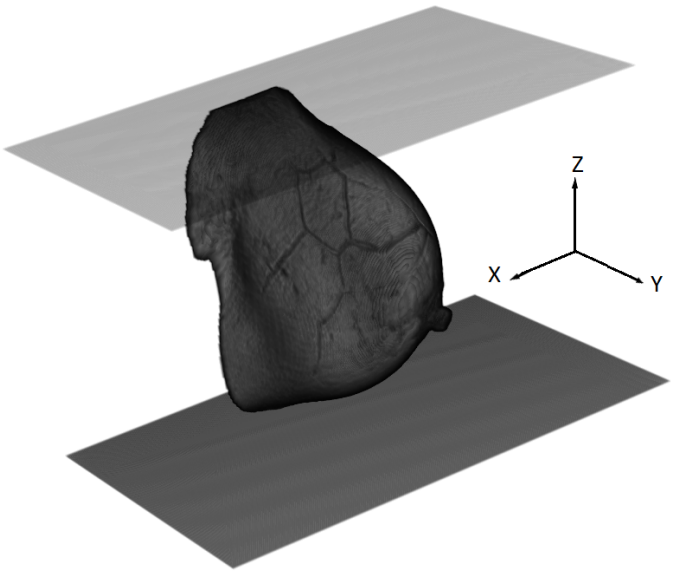


Figure 4.5: Configuration of the virtual paddles in the beginning of emulation of mammographic compression.

Subsequently, the $z$-coordinates of the points in $\Gamma_{k-1}$ are rectified according to

$$z \leftarrow \min\Big\{\max\{z,\, z_k^{\min}\},\, z_k^{\max}\Big\},$$

resulting in a new boundary $\Gamma_k$. (The parameters of the clipping procedure are shown in Figure 4.6).

Needless to say, that the new boundary $\Gamma_k$ is flawed in two critical ways. First, the clipping renders it non-smooth, which contradicts the natural curviness and regularity of breast surface. Second, $\Gamma_k$ is bound to encompass a smaller volume of tissue as compared to $\Gamma_{k-1}$, thus violating the volume preservation constraint that requires the initial and final breast volumes to be equal [97]. Accordingly, the above inconsistencies need to be remedied through an additional step of "restoration".

**Restoring:** To restore the regularity of $\Gamma_k$, its corresponding signed distance function $\psi$ is subjected to smoothing by means of *mean curvature flow* [61]

$$\frac{\partial\psi(\mathbf{r},t)}{\partial t} = -\mathrm{div}\left(\frac{\nabla\psi(\mathbf{r},t)}{\|\nabla\psi(\mathbf{r},t)\|}\right)\frac{\nabla\psi(\mathbf{r},t)}{\|\nabla\psi(\mathbf{r},t)\|}, \tag{4.10}$$

where $t$ stands for an artificial "diffusion" time, div and $\nabla$ denote the divergence and gradient operators, while $\|\cdot\|$ is standard Euclidian norm. Starting with the signed distance

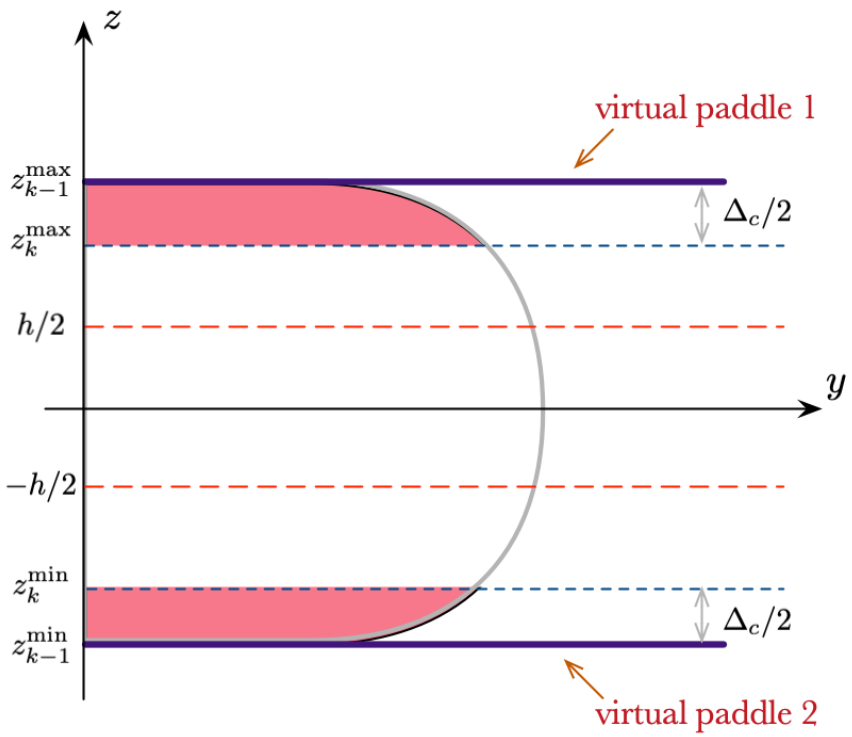


Figure 4.6: Parameters of the clipping procedure (sagittal view)

function of the "clipped" breast boundary, (4.10) forces it to evolve in the normal direction towards a solution with a minimal value of mean curvature. As a result, the evolution driven by (4.10) always results in smooth and regular boundaries which happen to be in a good compliance with the real-life morphology of the breast.

Unfortunately, if not properly constrained, solution to (4.10) is bound to converge to a single point, which is rather undesirable [60]. To prevent this outcome, the "curvature force" on the right hand side of (4.10) has been complemented with two additional terms, leading to

$$\frac{\partial \psi(\mathbf{r},t)}{\partial t} = \left[ -\operatorname{div}\left( \frac{\nabla \psi(\mathbf{r},t)}{\|\nabla \psi(\mathbf{r},t)\|} \right) + \gamma(t) + \mathcal{B} \right] \frac{\nabla \psi(\mathbf{r},t)}{\|\nabla \psi(\mathbf{r},t)\|}, \tag{4.11}$$

where

$$\gamma(t) = \int_\Omega \alpha(\mathbf{r},t) |\operatorname{div}\left( \frac{\nabla \psi(\mathbf{r},t)}{\|\nabla \psi(\mathbf{r},t)\|} \right) d\mathbf{r} \Big/ \int_\Omega \alpha(\mathbf{r},t)\, d\mathbf{r}$$

with $\alpha(\mathbf{r},t) = \|\nabla \mathcal{H}(\psi(\mathbf{r},t))\|$ being the (unit) indicator function of the evolving surface and

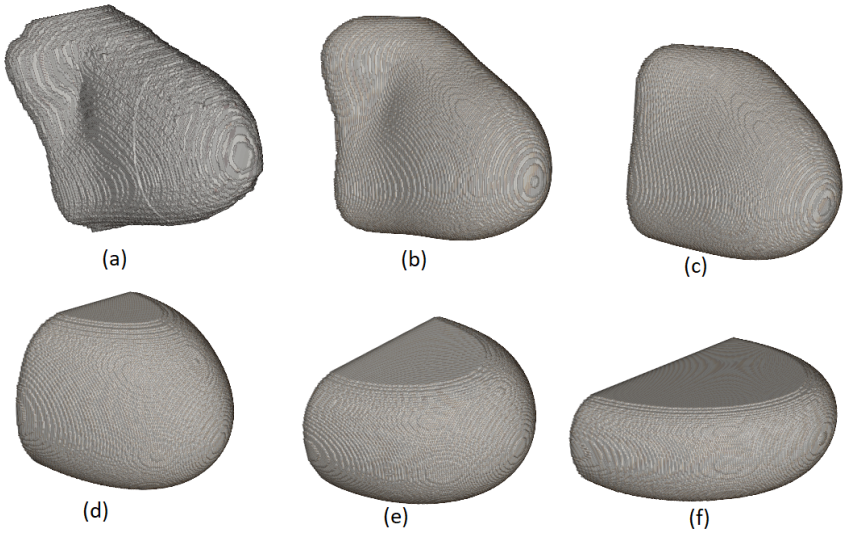


Figure 4.7: Evolution of the breast boundary under the CAR procedure: (a) original breast surface; (b-e) breast surface after 1, 3, 5, and 7 iterations, respectively; and (f) final solution after 10 iterations.

$\mathcal{H}$ standing for the Heavyside function, i.e., $\mathcal{H}(\tau) = 1$, if $\tau \geq 0$, and $\mathcal{H}(\tau) = 0$, otherwise. As shown in [78], the addition of $\gamma(t)$ guarantees the volume enclosed by the evolving boundary remains constant, thus enforcing the compression to be volume-preserving [97]. On the other hand, including $\mathcal{B} > 0$ gives rise to a ballooning (aka inflation) force which makes the breast boundary expand outwards, thereby increasing its volume [78]. This force needs to vanish when the expansion brings the volume to its initial value $V_0$. For this to happen, $\mathcal{B}$ has been set to be proportional to the difference between $V_0$ and the volume at time $t$, *viz.*

$$\mathcal{B} = \mu \left( V_0 - \int_\Omega \mathcal{H}(\psi(\mathbf{r}, t))\, d\mathbf{r} \right)$$

for some predefined $\mu > 0$. In this way, the effect of the ballooning force is forced to vanish as the evolving volume reaches its target value of $V_0$.

In the practical implementation of (4.11), it is important to pay close attention to boundary conditions to prevent the estimated boundary from "leaking" into the chest wall as well as outside the "between-the-paddle" space. This can be achieved by using Dirichlet boundary conditions both on the chest wall (i.e., when $y = 0$) and the paddle planes.

The clipping and restoration stages of the CAR procedure are repeated sequentially until the between-the-paddles distance $z_k^{\max} - z_k^{\min}$ reaches a target value of $h$ that is equal

to the physical thickness of the breast at the end of compression. In this case, the clipping parameter $\Delta_c$ can be set to be equal to

$$\Delta_c = (z_0^{\max} - z_0^{\min} - h)/N,$$

where $N$ denotes the total number of CAR iterations. It has been observed that, most of the time, setting $N = 10$ is sufficient to complete the emulation in a stable and consistent manner. The results of the CAR procedure are exemplified in Figure 4.7, which shows an initial breast surface (Subplot (a)) along with the compressed surfaces corresponding to $k = 1, 3, 5, 7$ (Subplots (b)-(e)) and the final solution at $N = 10$ (Subplot (f)).

Finally, the CAR procedure detailed above is only capable of tracking the motion of the breast surface. To estimate the global deformation $\varphi_{\text{glb}}$, it is therefore necessary to extend the boundary displacement to the entire domain $\Omega$. To this end, we used a procedure similar to the one exploited in Section 4.3. In particular, at the end of each iteration of CAR, the trajectories of the boundary points were computed based on spatial proximity. Subsequently, the incremental trajectories thus obtained were integrated into the global displacement relating the configuration of the breast boundary at the initial and final stages of CAR. As a final step, the boundary displacement was extrapolated to the entire image domain by means of TPS interpolation, producing the required estimate $\hat{\varphi}_{\text{glb}}$. It should be noted that the choice of the interpolation model has been by no means arbitrary, but rather rooted in the property of TPS to yield approximations of minimal bending energy, which seems to be in a good agreement with the general tendency of breast tissue to deform in the most "ergonomic" way. A representative output of the proposed algorithm is demonstrated in Figure 4.8.

## 4.5 Estimation of Residual Deformation

Given a prediction of the global component of $\varphi$, the next step is to estimate its residual part $\varphi_{\text{res}}$ through registering $\tilde{f} := \mathcal{I}_f(f) \circ \hat{\varphi}_{\text{glb}}$ and $\tilde{g} := \mathcal{I}_g(g)$. In our proposed solution, $\varphi_{\text{res}}$ is assumed to be a member of the parametric family $\Phi$ of piecewise polynomial functions. Specifically, with $\mathbf{r} = (x, y, z)$, let $\varphi_{\text{res}}^x(\mathbf{r})$, $\varphi_{\text{res}}^y(\mathbf{r})$, and $\varphi_{\text{res}}^z(\mathbf{r})$ be the $x$, $y$, and $z$ components of $\varphi_{\text{res}}$, respectively, so that

$$\varphi_{\text{res}}(\mathbf{r}) = \varphi_{\text{res}}^x(\mathbf{r})\,\mathbf{i} + \varphi_{\text{res}}^y(\mathbf{r})\,\mathbf{j} + \varphi_{\text{res}}^z(\mathbf{r})\,\mathbf{k},$$

where $\mathbf{i}$, $\mathbf{j}$, $\mathbf{k}$ denote the unit vectors in the direction of corresponding spatial coordinates. Then, each of the three components of $\varphi_{\text{res}}$ is assumed to be given as

$$\varphi_{\text{res}}^l(\mathbf{r}) = \sum c_{\mathbf{n}}^l\, \boldsymbol{\beta}(\mathbf{r}/\Delta - \mathbf{n}), \quad l \in (x, y, z), \tag{4.12}$$

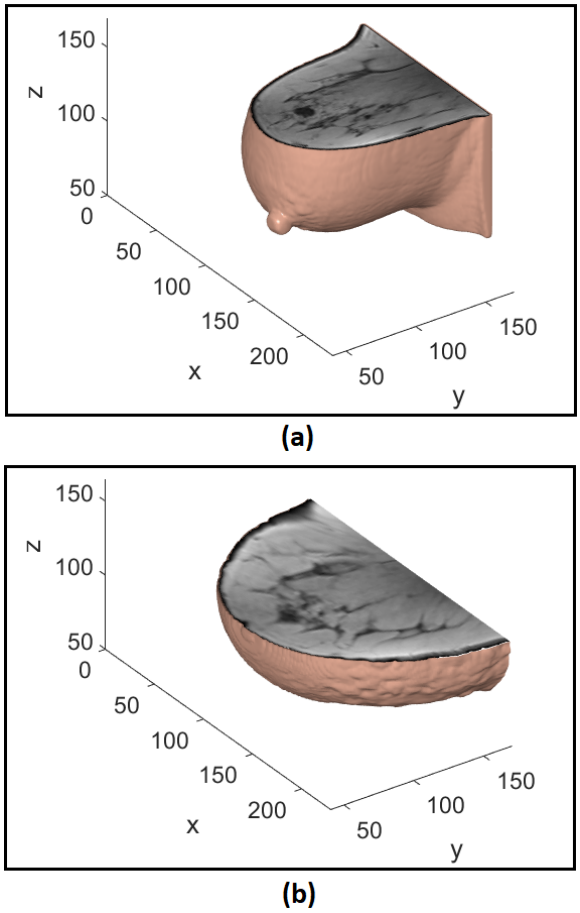


Figure 4.8: Global deformation of an MRI volume under the CAR procedure: (a) original MRI volume; and (b) compressed MRI volume.

with $\mathbf{n} = (n^x, n^y, n^z)$ being a triplet of integer translations and $\boldsymbol{\beta}(\mathbf{r})$ denoting a *separable* B-spline of the form

$$\boldsymbol{\beta}(\mathbf{r}) = \beta(x)\,\beta(y)\,\beta(z),$$

with $\beta$ being a one-dimensional B-spline of some predefined degree. In (4.12), the parameter $\Delta > 0$ is used to govern the location of control points and their associated spline coefficients $c^l_{\mathbf{n}}$, thus determining the spatial resolution of the residual transformation.

The use of parametric representation allows reducing the estimation of $\varphi_{\text{res}}$ to the problem of finding a set of optimal spline coefficients, which, for the sake of convenience, we agglomerate into a single numerical array $\mathbf{c} = \{c^x_{\mathbf{n}}, c^y_{\mathbf{n}}, c^z_{\mathbf{n}}\}$. The number of such coefficients

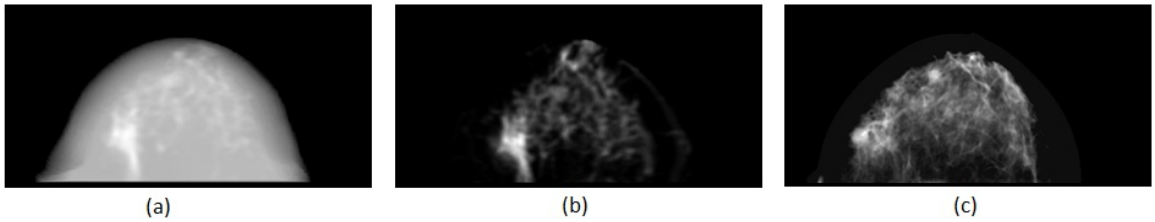


Figure 4.9: Transformed intensity images: (a) Projected pseudo-CT; (b) Fibroglandular thickness computed from MRI scan; (c) Fibroglandular thickness computed from mammogram.

is a function of $\Delta$, with its higher values resulting in a smaller number of unknowns. To render the numerical estimation of $\mathbf{c}$ stable, we employ a multi-scale approach, in which the estimation is initially done for a relatively large $\Delta$, followed by a sequence of refinements via gradually reducing its value by a factor of 2. Thus, in the beginning of iterations, the estimation produces a coarse approximation of $\varphi_{\text{res}}$, which is robust against the effects of noise. As the refinement advances, the spline model acquires more degrees of freedom (at the expense of a greater number of coefficients $\mathbf{c}$), yielding progressively finer estimates of the residual deformation.

The multi-scale approach to the estimation of $\mathbf{c}$ has been found to be a useful means to prevent convergence to locally optimal solutions, producing consistent reconstructions across various geometries and compositions of the breast. Yet, as $\Delta$ approaches the resolution of imaging data, the estimation becomes more variable and, with that, less stable numerically. A particularly simple and effective way to mitigate such instabilities is to augment the optimization cost with an additional regularization term. In this work, the regularization has been achieved by constraining the "bending energy" of the residual deformation that is given by [101]

$$\mathcal{R}(\mathbf{c}) = \frac{1}{2} \sum_{l \in (x,y,z)} \int_{\Omega} \left| \nabla \varphi^{l}_{\text{res}}(\mathbf{r} \mid \mathbf{c}) \right|^2 d\mathbf{r}, \tag{4.13}$$

where $\nabla \varphi^{l}_{\text{res}}(\mathbf{r} \mid \mathbf{c})$ denotes the gradient of $\varphi^{l}_{\text{res}}(\mathbf{r} \mid \mathbf{c})$ at $\mathbf{r}$, with its magnitude equal to $|\nabla \varphi^{l}_{\text{res}}(\mathbf{r} \mid \mathbf{c})|$. With the addition of $\mathcal{R}(\mathbf{c})$, it turns out to be unnecessary to devise a special rule for termination of the multi-scale update, in which case, the estimation can be stopped at the value of $\Delta$ below which no further improve in the optimization cost is observed.

As it was mentioned in the introduction, the present work explores a number of different definitions of the intensity transformations, which has been paired with two similarity

measures. The first one was chosen to be the standard SSD given by [4]

$$\mathcal{S}_{\mathrm{SSD}}(\mathbf{c}) = -\iint_{\Omega_{2\mathrm{D}}} \left|\mathcal{P}\{\tilde{f}\circ\varphi_{\mathrm{res}}(\mathbf{c})\}(x,y) - \tilde{g}(x,y)\right|^2 dx\,dy \tag{4.14}$$

where the negative sign is added to keep the definition consistent with the maximization in (4.4). With addition of the regularization term $\mathcal{R}(\mathbf{c})$, this case amounts to maximization of $\mathcal{S}_{\mathrm{SSD}}(\mathbf{c}) - \lambda\mathcal{R}(\mathbf{c})$, with $\lambda > 0$ being a user-defined regularization parameter.

In addition to SSD, which is generally considered to be an intra-modal distance, we also used a cross-modal similarity measured in terms of MI [109, 144]. The definition of MI relies on both joint and marginal probability distributions of registered images. With $K$ being a Parzen window [116], the empirical distributions of $\mathcal{P}\{\tilde{f}\circ\varphi_{\mathrm{res}}\}$ and $\tilde{g}$ have been computed according to

$$P_{\tilde{f}}(r \mid \mathbf{c}) = \frac{1}{|\Omega_{2\mathrm{D}}|}\iint_{\Omega_{2\mathrm{D}}} K\left(r - \mathcal{P}\{\tilde{f}\circ\varphi_{\mathrm{res}}(\mathbf{c})\}(x,y)\right) dx\,dy$$

and

$$P_{\tilde{g}}(s) = \frac{1}{|\Omega_{2\mathrm{D}}|}\iint_{\Omega_{2\mathrm{D}}} K\left(s - \tilde{g}(x,y)\right) dx\,dy,$$

respectively, while their joint distribution was defined as[5]

$$\begin{aligned} P(r,s \mid \mathbf{c}) &= \\ &= \frac{1}{|\Omega_{2\mathrm{D}}|}\iint_{\Omega_{2\mathrm{D}}} K\left(r - \mathcal{P}\{\tilde{f}\circ\varphi_{\mathrm{res}}(\mathbf{c})\}(x,y)\right) K\left(s - \tilde{g}(x,y)\right) dx\,dy. \end{aligned} \tag{4.15}$$

With the above definitions, MI can now be defined according to [162],

$$\mathcal{S}_{\mathrm{MI}}(\mathbf{c}) = \iint P(r,s \mid \mathbf{c}) \log\left(\frac{P(r,s \mid \mathbf{c})}{P_{\tilde{f}}(r \mid \mathbf{c})P_{\tilde{g}}(s)}\right) dr\,ds \tag{4.16}$$

Consequently, in this case, the objective function to maximize is given by $\mathcal{S}_{\mathrm{MI}}(\mathbf{c}) - \lambda\mathcal{R}(\mathbf{c})$.

In our experiments, the optimization over $\mathbf{c}$ has been performed by means of the standard gradient ascent algorithm, a iteration of which is given by

$$\mathbf{c}^{(t+1)} = \mathbf{c}^{(t)} + \tau\left(\nabla\mathcal{S}(\mathbf{c}^{(t)}) - \lambda\nabla\mathcal{R}(\mathbf{c}^{(t)})\right), \tag{4.17}$$

where $\mathcal{S}$ is set to be $\mathcal{S}_{\mathrm{MI}}$ or $\mathcal{S}_{\mathrm{SSD}}$, and $\tau > 0$ is a predefined step-size.

[5] Note that $P_{\tilde{f}}(r \mid \mathbf{c}) = \int P(r,s \mid \mathbf{c})\,ds$, offers an alternative way of computing $P_{\tilde{f}}(r \mid \mathbf{c})$.

To estimate the optimal values of $\mathbf{c}$, one needs to compute the gradient of regularized objective functions, $\mathcal{S}_{\text{MI}}(cc) - \lambda\mathcal{R}(\mathbf{c})$ and $\mathcal{S}_{\text{SSD}}(\mathbf{c}) - \lambda\mathcal{R}(\mathbf{c})$, which requires computing the derivative of each term with respect to $c^l_{\mathbf{n}}$.

As shown by [155], computation of the derivative of $\mathcal{S}_{\text{MI}}(\mathbf{c})$ respect to $c^l_{\mathbf{n}}$ boils down to

$$\frac{\partial \mathcal{S}_{\text{MI}}(\mathbf{c})}{\partial c^l_{\mathbf{n}}} = \iint \frac{\partial P(r,s \mid \mathbf{c})}{\partial c^l_{\mathbf{n}}} log(\frac{P(r,s \mid \mathbf{c})}{P_{\tilde{f}}(l|\mathbf{c})})\, dr\, ds \tag{4.18}$$

which only requires the calculation of $\frac{\partial P(r,s|\mathbf{c})}{\partial c^l_{\mathbf{n}}}$. Using (4.16) one can write

$$\begin{aligned}\frac{\partial P(r,s|\mathbf{c})}{\partial c^l_{\mathbf{n}}} = \frac{1}{|\Omega_{2D}|} \iint_{\Omega_{2\text{D}}} K(s - \tilde{g}(x,y)) \frac{\partial K}{\partial u}\Big|_{u=r-\mathcal{P}\{\tilde{f}\circ\varphi_{\text{res}}(\mathbf{c})\}(x,y)} \\ \times -\frac{\partial \mathcal{P}\{\tilde{f}\circ\varphi_{\text{res}}(\mathbf{c})\}(x,y)}{\partial c^l_{\mathbf{n}}}\, dx\, dy\end{aligned}$$

where

$$\frac{\partial \mathcal{P}\{\tilde{f}\circ\varphi_{\text{res}}(\mathbf{c})\}}{\partial c^l_{\mathbf{n}}} = \int_z \nabla\tilde{f}(\mathbf{r} + \varphi_{\text{res}}(\mathbf{r}|\mathbf{c}))^T \frac{\partial \varphi_{\text{res}}(\mathbf{r}|\mathbf{c})}{\partial c^l_{\mathbf{n}}} dz.$$

Note that $l \in \{x, y, z\}$, $\frac{\partial \varphi_{\text{res}}(\mathbf{r}|\mathbf{c})}{\partial c^x_{\mathbf{n}}} = (\boldsymbol{\beta}(\mathbf{r}/\Delta - \mathbf{n}), 0, 0)$, $\frac{\partial \varphi_{\text{res}}(\mathbf{r}|\mathbf{c})}{\partial c^y_{\mathbf{n}}} = (0, \boldsymbol{\beta}(\mathbf{r}/\Delta - \mathbf{n}), 0)$ and $\frac{\partial \varphi_{\text{res}}(\mathbf{r}|\mathbf{c})}{\partial c^z_{\mathbf{n}}} = (0, 0, \boldsymbol{\beta}(\mathbf{r}/\Delta - \mathbf{n}))$.

Using Equation (4.14) and applying basic derivative rules, the derivative of $\mathcal{S}_{\text{SSD}}(\mathbf{c})$ can be computed as follows,

$$\begin{aligned}\frac{\partial \mathcal{S}_{\text{SSD}}(\mathbf{c})}{\partial c^l_{\mathbf{n}}} = -2 \iint_{\Omega_{2\text{D}}} \left(\mathcal{P}\{\tilde{f}\circ\varphi_{\text{res}}(\mathbf{c})\}(x,y) - \tilde{g}(x,y)\right) \\ \times \frac{\partial \mathcal{P}\{\tilde{f}\circ\varphi_{\text{res}}(\mathbf{c})\}(x,y)}{\partial c^l_{\mathbf{n}}}\, dx\, dy.\end{aligned} \tag{4.19}$$

On the other hand, derivative of the regularization term with respect to $c^l_{\mathbf{n}}$ is given by

$$\frac{\partial \mathcal{R}(\mathbf{c})}{\partial c^l_{\mathbf{n}}} = \int_\Omega \nabla\varphi^l_{\text{res}}(\mathbf{r} \mid \mathbf{c}) \cdot \frac{\partial \nabla\varphi^l_{\text{res}}(\mathbf{r} \mid \mathbf{c})}{\partial c^l_{\mathbf{n}}}\, d\mathbf{r}$$

where $\nabla\varphi^l_{\text{res}}(\mathbf{r} \mid \mathbf{c}) = \left[\frac{\partial\varphi^l_{\text{res}}(\mathbf{r}|\mathbf{c})}{\partial x}, \frac{\partial\varphi^l_{\text{res}}(\mathbf{r}|\mathbf{c})}{\partial y}, \frac{\partial\varphi^l_{\text{res}}(\mathbf{r}|\mathbf{c})}{\partial z}\right]$. $\varphi^l_{\text{res}}(\mathbf{r} \mid \mathbf{c})$ is defined as a linear combination of separable cubic B-splines (4.12), thus, for example, one can compute $\frac{\partial \nabla\varphi^x_{\text{res}}(\mathbf{r}|\mathbf{c})}{\partial c^x_{\mathbf{n}}}$ as follows,

$$\frac{\partial \nabla\varphi^x_{\text{res}}(\mathbf{r} \mid \mathbf{c})}{\partial c^x_{\mathbf{n}}} = \left[\frac{\partial^2\varphi^x_{\text{res}}(\mathbf{r} \mid \mathbf{c})}{\partial x\, \partial c^x_{\mathbf{n}}}, \frac{\partial^2\varphi^x_{\text{res}}(\mathbf{r} \mid \mathbf{c})}{\partial y\, \partial c^x_{\mathbf{n}}}, \frac{\partial^2\varphi^x_{\text{res}}(\mathbf{r} \mid \mathbf{c})}{\partial z\, \partial c^x_{\mathbf{n}}}\right]$$

where

$$\frac{\partial^2 \varphi^x_{\text{res}}(\mathbf{r} \mid \mathbf{c})}{\partial x\, \partial c^x_{\mathbf{n}}} = \frac{1}{\Delta} \frac{d\,\beta(u)}{d\,u}\bigg|_{u=\frac{x}{\Delta}-n^x} \beta(\frac{y}{\Delta}-n^y)\beta(\frac{z}{\Delta}-n^z)$$

$$\frac{\partial^2 \varphi^x_{\text{res}}(\mathbf{r} \mid \mathbf{c})}{\partial y\, \partial c^x_{\mathbf{n}}} = \frac{1}{\Delta} \beta(\frac{x}{\Delta}-n^x) \frac{d\,\beta(u)}{d\,u}\bigg|_{u=\frac{y}{\Delta}-n^y} \beta(\frac{z}{\Delta}-n^z)$$

$$\frac{\partial^2 \varphi^x_{\text{res}}(\mathbf{r} \mid \mathbf{c})}{\partial z\, \partial c^x_{\mathbf{n}}} = \frac{1}{\Delta} \beta(\frac{x}{\Delta}-n^x)\beta(\frac{y}{\Delta}-n^y) \frac{d\,\beta(u)}{d\,u}\bigg|_{u=\frac{z}{\Delta}-n^z}$$

$\frac{\partial \nabla \varphi^y_{\text{res}}(\mathbf{r}|\mathbf{c})}{\partial c^y_{\mathbf{n}}}$ and $\frac{\partial \nabla \varphi^z_{\text{res}}(\mathbf{r}|\mathbf{c})}{\partial c^z_{\mathbf{n}}}$ can be computed in the same manner.

Finally, in our practical examples, both $\boldsymbol{\beta}$ and $K$ have been chosen to be given by a cubic B-spline, which offers an excellent compromise between the accuracy of approximation and the efficiency of numerical implementation [156]. Also, in the course of optimization, it is required to extrapolate the values of $\tilde{f}$ and its gradient in between the points of a discrete numerical grid, which was achieved by means of cubic interpolation.

To accelerate the gradient descent optimization, the limited-memory quasi-Newton minimization algorithm [19] was applied which reduces the objective function until termination criteria are satisfied. The limited-memory quasi-Newton method is faster because instead of estimating the entire Hessian during minimization, only a low-rank approximation is calculated, allowing linear or super-linear convergence rates. It also provides an additional advantage by allowing bound constraints on the independent variables.

In summary, we introduced two different geometry-dependent strategies for estimating global deformation. The first one is formulated using an analytical model that is superquadratic and, on the other hand, the second approach is based on the process of evolution and clipping-restoring procedure. The process of predicting the global deformation is followed by estimating the residual deformation where we take advantage of FFD model. In the next chapter, the performance of our proposed framework will be evaluated.

# Chapter 5

# Experimental Results

In this chapter, we demonstrate quantitative and visual results of registering 3-D breast MRI images to digital mammograms on a clinical dataset using our proposed registration approach. The results are compared against FEM-basd registration methods discussing the advantages of our method over other algorithms.

## 5.1 Evaluation

The proposed method was tested on a clinical dataset consisting of MRI and mammogram data acquired from 10 different subjects with unilateral breast lesions. Each case consisted of a structural T1-weighted MRI volume and two mammographic images (i.e., CC and MLO mammograms). All the imaging data were acquired approximately at the same time point to avoid the significant change of tissues inside the breast. The breast MRI scans were acquired at the Princess Margaret Cancer Centre (Toronto, Canada) by means of a 3T Signa$^{TM}$ Premier MRI scanner (GE Healthcare, Inc.). The spatial resolution of MRI scans was set to $0.76\,\text{mm} \times 0.76\,\text{mm} \times 1.2\,\text{mm}$, resulting in MRI volumes of size $448 \times 448 \times 210$ voxels. The digital mammograms, acquired at the same centre, had the spatial resolution of $0.094\,\text{mm} \times 0.094\,\text{mm}$, with the associated size of $2294 \times 1914$ pixels. Prior to numerical treatment, both MRI and mammogram images were resampled to 1 $\text{mm}^3$ isotropic resolution. Moreover, the images have also been subjected to the procedure of histogram equalization to increase the contrast of the fibroglandular component of breast tissue.

In this study, we worked with unilateral diseases where only one breast is affected. Also, the cases are not mammographically occult which allowed expert segmentation and

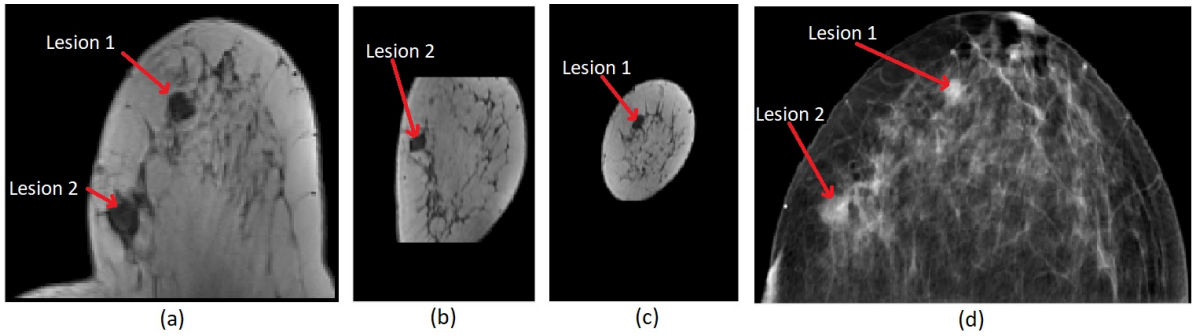


Figure 5.1: Sample case with visible lesions: (a) Lesions in an MRI slice (Transversal view); (b,c) Lesions in MRI slices (Sagittal view); (d) Same lesions depicted by mammography

annotation of lesions in both MRI and mammography scans. Figure 5.1 shows lesions in MRI and mammogram images of a sample case. For the sake of quantitative comparison, the Target Registration Error (TRE) metric has been used to evaluate the accuracy of the proposed methods. To compute TRE, one needs to have reference points in both images, which are called landmarks. However, in our experiments, the center of mass of the lesion was used to compute the error. Consequently, the TRE is computed as the Euclidean distance between the centroid of the 2-D tumor in the mammogram and the projected centroid of the 3-D tumor [36].

Estimating the residual deformation was carried out in three different resolutions. In the first resolution (coarse resolution) the distance between control points, the center of B-spline kernels, was 20 mm in each $x$, $y$, and $z$-direction. In the second and third resolutions, this distance was set to 10 mm and 5 mm, respectively. Furthermore, since the deformation in $z$-direction is mainly incorporated in the estimation of global part $\hat{\varphi}_{glb}$, the amount of deformation in the $z$-direction was limited. To do so, in the phase of residual deformation computation, $\varphi^z_{\text{res}}$ has been restricted to vary slowly in comparison to $\varphi^x_{\text{res}}$ and $\phi^y_{\text{res}}$.

As it was mentioned in the previous chapter, another objective of the present study has been the exploration of two intensity transformation models and their performance under two different similarity measures, i.e., SSD and MI. The first transformation model is defined by (4.5) which aims at transforming an MRI volume into an *"emulated" X-ray* (EXR) volume prior to its projection onto the mammographic plane. The second transformation model is based on computing the physical Thickness of the Dense (fibroglandular) Tissue (TDT), both in MRI and mammogram scans (using (4.6)).

In the rest of this chapter, the results obtained by the two proposed registration approaches, global deformation using a superquadratic model and the CAR procedure, will

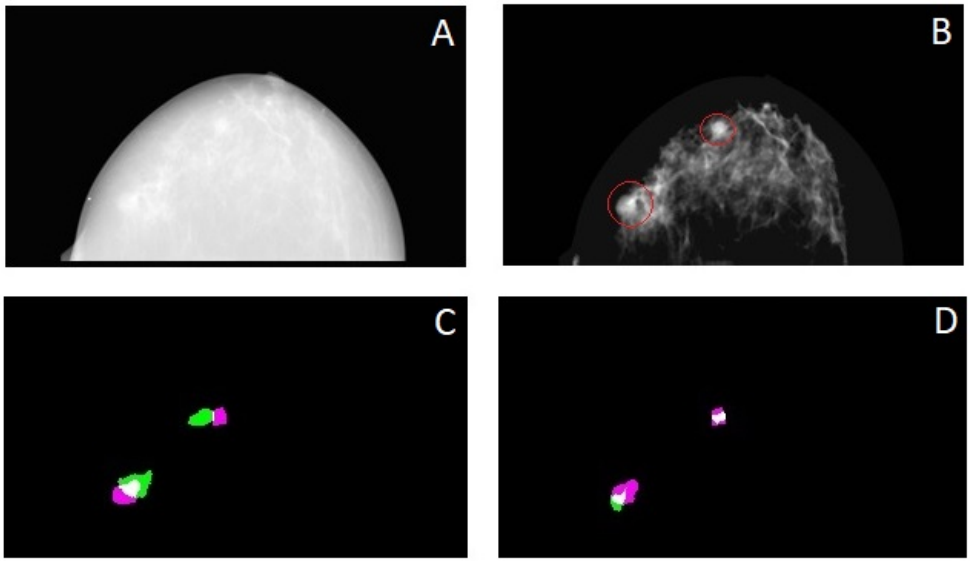


Figure 5.2: Registration results of subject 1 using superquadratic model: (A) Test mammogram in CC view; (B) Thickness of dense tissue of A; (C) Result using EXR; (D) Results using TDT. In both (C) and (D), purple shows the manually segmented lesion in the mammogram and green indicates the projected lesion.

be discussed.

## 5.2 Quantitative Assessment of Superquadratic Model

The proposed superquadratic model (Section 4.3) for global deformation estimation was applied to bring breast MRIs and mammograms in CC view to an alignment. Then, the alignment was refined by applying the proposed approach (Section 4.5) for residual deformation estimation.

Figures 5.2 - 5.5 illustrate the results of registration for some sample cases using EXR and TDT images. The visible boundaries of lesions are outlined red in thickness (TDT) images. In the case of both registrations (using thickness and simulated X-ray images) the deformed and projected lesions are shown with green color, while manually segmented tumors (from mammograms) are purple. The overlap between the two lesions is indicated

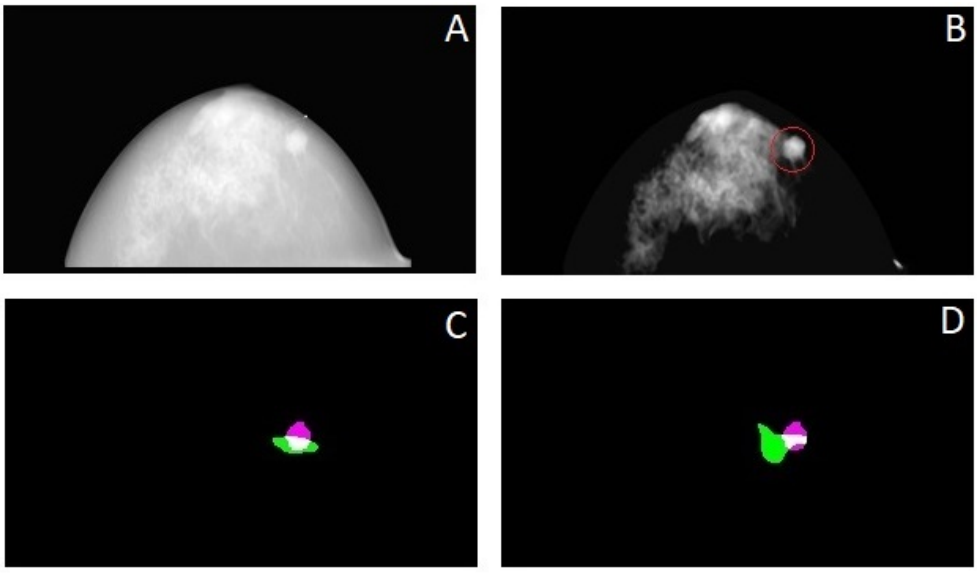


Figure 5.3: Registration results of subject 4 using superquadratic model: (A) Test mammogram in CC view; (B) Thickness of dense tissue of A; (C) Result using EXR; (D) Results using TDT. In both (C) and (D), purple shows the manually segmented lesion in the mammogram and green indicates the projected lesion.

in white color. As it can be observed that in both cases the projected lesions are reasonably close to lesions in the mammograms.

Table 5.1 summarizes the registration results on 10 different cases in the dataset. The obtained mean TRE for registration by thickness images is 5.44 mm ± 3.61 mm and it is 7.49 mm±3.72 mm for registration using EXR images. Considering each case independently, all of the TREs are lower than 13 mm for both registrations (use of EXR and TDT images). Comparing TREs by simulated X-ray and fibroglandular thickness, it is clear that the use of thickness images results in smaller errors. However, the standard deviation is almost the same for both approaches, indicating the same consistency of these methods. In the case of fatty breast tissues, e.g., case 1 or case 7, there is less information (fibroglandular tissue) and as a result, the simulated EXR is a relatively uniform image. In these kinds of images, it is hard to drive the deformation and subsequently, the optimization is more likely to terminate at a local minima. For example, using EXR images for registration resulted in TRE of 11.63 mm in case 1. However, using thickness images may result in higher accuracy in the case of fatty breasts. In fibroglandular thickness images, TDT, fatty areas are treated as background; it only considers fibroglandular tissue. Therefore, if the tumors

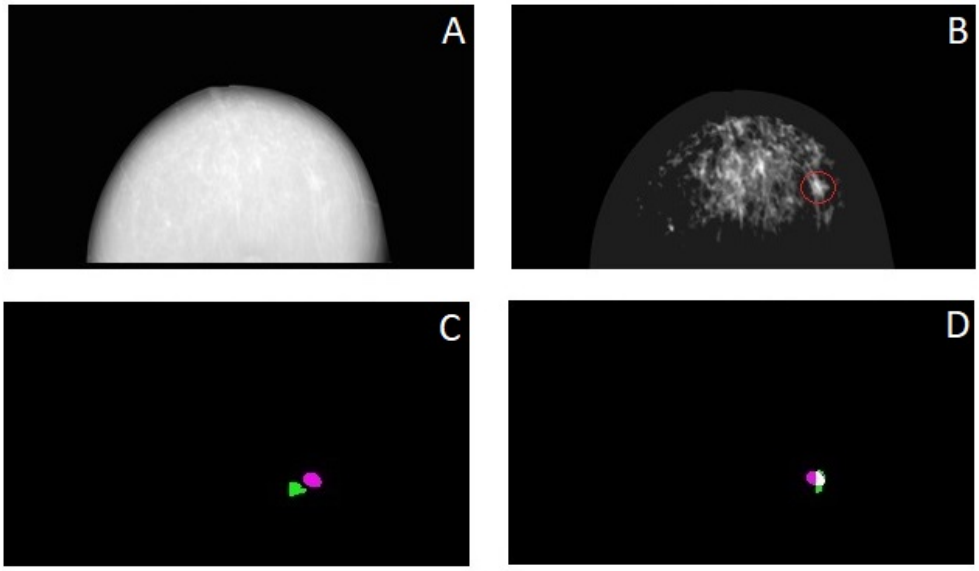


Figure 5.4: Registration results of subject 6 using superquadratic model: (A) Test mammogram in CC view; (B) Thickness of dense tissue of A; (C) Result using EXR; (D) Results using TDT. In both (C) and (D), purple shows the manually segmented lesion in the mammogram and green indicates the projected lesion.

from the mammogram and the projected MRI volume have been brought close to each other by $\hat{\varphi_{\text{glb}}}$, the FFD model will align them precisely in the second step of the proposed framework. For instance, registering thickness images resulted in TRE of 0.54 mm for case 1. On the other hand, the breast boundary usually contains only fat, and consequently, the boundary of the breast tissue will not be distinct in the fibroglandular thickness images. Therefore, the resulting deformation field may not be physically plausible in the boundary, or even areas far from fibroglandular tissue.

The accuracy of the proposed approach is comparable with that obtained from FEM-based methods (shown in Table 5.2). All of these methods use image intensity to optimize the objective function over registration parameters. Note that there is no standard database, and one should be cautious comparing the results provided by previous works. However, comparing the TRE figures obtained by our approach as well as by the FEM-based methods, one can see that results are of the same order of accuracy.

In the literature, some papers use the correspondences between mammogram boundary and projected MRI boundary to judge the accuracy of the registration. However, due to use of surface fitting in the first step and applying the FFD model in the second step of our

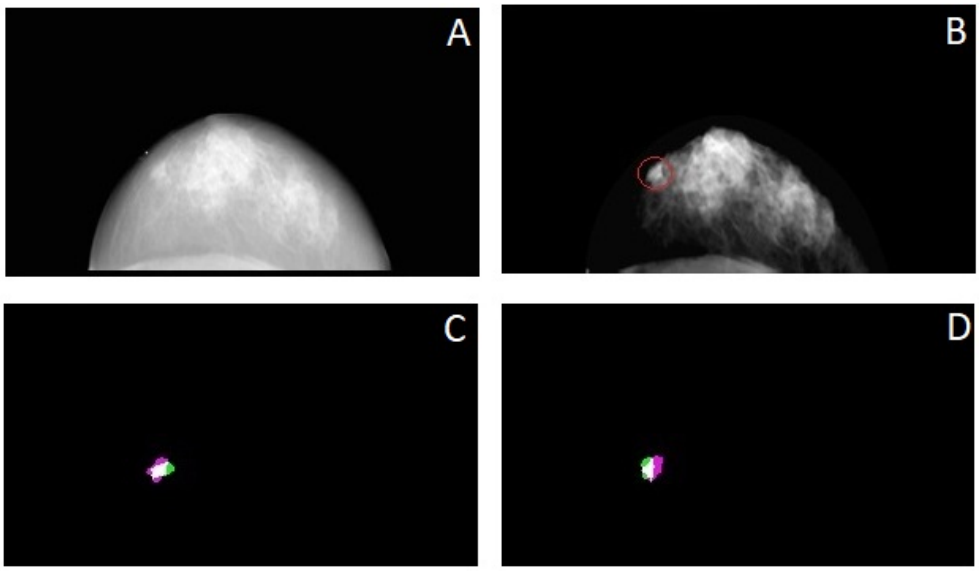


Figure 5.5: Registration results of subject 10 using superquadratic model:(A) Test mammogram in CC view; (B) Thickness of dense tissue of A; (C) Result using EXR; (D) Results using TDT. In both (C) and (D), purple shows the manually segmented lesion in the mammogram and green indicates the projected lesion.

proposed method, the boundaries of the two images coincide with each other completely, especially when EXR images are used to do the registration. Therefore, our algorithm's accuracy would be much higher from this point of view. Figure 5.6 shows the boundaries of the registered synthetic mammogram and the original mammogram of a sample case. As it can be seen, the two boundaries match each other.

## 5.3 Quantitative Assessment of the CAR Procedure

The performance of the proposed CAR model has been evaluated in four different scenarios, where two intensity transformations (EXR and TDT) and apply two similarity measures, namely MI and SSD, have been used. The proposed method has been applied to align breast MRI images with its associated mammograms in both CC and MLO views.

As an example, Subplots A and E of Figure 5.7 show the CC and MLO mammograms collected from the same subject, with the corresponding TDT shown in Subplots B and F, respectively. The remaining subplots of the figure demonstrate the results of SSD-based

Table 5.1: Target registration error obtained by superquadratic model, in millimeters, for the 10 CC -mammograms using EXR and TDT image

| | Using EXR images | Using TDT image |
|---|---|---|
| Case 1 | 11.63 | 0.54 |
| Case 2 | 8.15 | 8.27 |
| Case 3 | 13.4 | 11.21 |
| Case 4 | 5.4 | 10.26 |
| Case 5 | 2.45 | 3.29 |
| Case 6 | 6.24 | 2.44 |
| Case 7 | 6.74 | 6.91 |
| Case 8 | 12.01 | 3.13 |
| Case 9 | 5.33 | 3.78 |
| Case 10 | 5.58 | 4.25 |
| Mean | 7.49 | 5.44 |
| STD | 3.72 | 3.61 |

Table 5.2: TRE(mm) of recent FEM-based methods in the literature

| Method | CC | MLO |
|---|---|---|
| Garcia [40] {isotropic} | 9.02±4.28 | 12.96±3.78 |
| Garcia[41] | 9.90±3.72 | 8.04±4.68 |
| Mertzanidou[98] | 11.6±3.8 | 11.0±5.40 |
| Solves[148] | 4.2 ±1.9 | 4.8±1.3 |
| Mertzanidou[97] | 12.9 | 13.9 |

image registration using the EXR (Subplots C and G) and TDT models (Subplots D and H). Here, the spatial location of a breast lesion is shown with the red-colored circles, while the purple and green colors encode the manual delineation of the lesion and its MRI-based projection, respectively. The overlap between the manual and MRI-based delineations is shown with the white color, which indicates a good match between them.

Tables 5.3 and 5.4 summarize the results of MRI to mammogram registration obtained for different intensity transformation models (i.e., EXR and TDT ) and similarity measures (i.e., SSD and MI ). In particular, Table 5.3 shows the values of TRE for 10 cases of CC mammograms – case 1 through case 10 – corresponding to various settings. The mean values of the error and its standard deviation are indicated in the last two columns of the table, respectively. Table 5.4, on the other hand, shows the values of TRE for 10 cases of

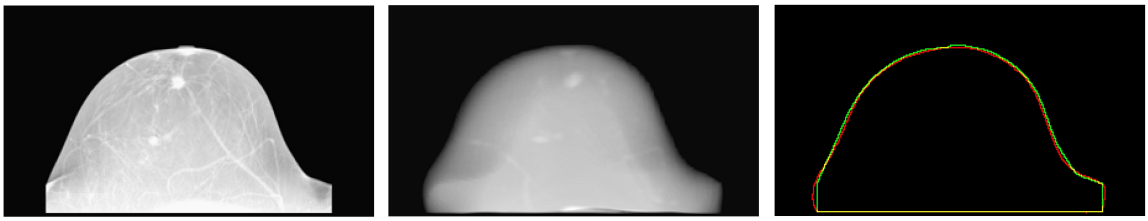


Figure 5.6: Results of registration using EXR images for a sample case: (a) Real mammogram in CC view; (b) Registered synthetic mammogram; and (c) Boundaries of two registered images in (a) and (b). The green line is the boundary of FFDM and red one is the boundary of registered image.

MLO mammograms, following the same arrangement as in Figure 5.3. One can see that, in both scenarios, the best performance is achieved through combining the TDT intensity model with the SSD metric, resulting in the average values of 4.81 mm ± 3.44 mm and 7.59 mm ± 4.88 mm in the case of CC and MLO mammograms, respectively.

A more detailed analysis of Tables 5.3 and 5.4 reveals that, in the case of CC mammograms, the values of TRE remains below 10 mm in all subjects, while the corresponding values in the case of MLO mammograms are bounded from above by 11 mm. The obtained values compare favourably with the results of much more complex, FEM-based registration methods which are summarized in Table 5.2. It should be emphasized that, even though in some cases, the difference in the results does not seem to be critical, the proposed solution has been achieved by much simpler computational means, without any need for intervention by a human interpreter.

When comparing the performance of SSD and MI criteria, one can see that both measures produced comparable results under the EXR intensity transformation model. Thus, in particular, the mean values of TRE in the case of CC and MLO mammograms was found to be about 8.5 mm and 11 mm, respectively, while having similar values of its standard deviation around 4 mm. However, in the case of the TDT intensity model, the two similarity metrics produced considerably different outcomes, with the SSD-based registration offering better accuracy as compared to the case of MI. This result, however, was expected. Indeed, under the TDT model, the values of both MRI and mammogram scans are transformed into estimates of the physical thickness of dense tissue, thereby equalizing their photometric properties and dynamic ranges. Consequently, the resulting $\mathcal{P}\{\mathcal{I}_f(f)\circ\varphi\}$ and $\mathcal{I}_g(g)$ are perceived by SSD as if they were produced by the same imaging modality, which makes this measure particularly effective. On the other hand, the EXR intensity model of (4.5)

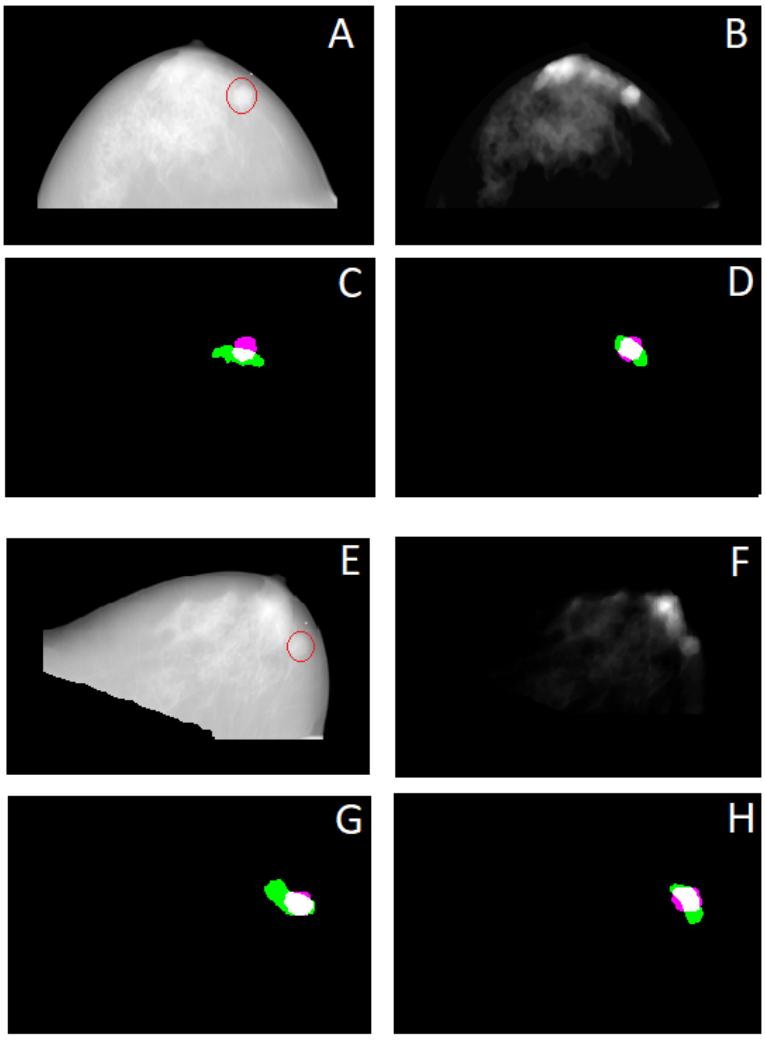


Figure 5.7: Results of SSD-based MRI to mammogram registration using CAR model: (A) Test mammogram in CC view; (B) thickness of dense tissue for the image in A; (C) Manually (purple) and MRI-based (green) delineation of the breast lesion under the EXR intensity transformation corresponding to A; (D) Manually (purple) and MRI-based (green) delineation of the breast lesion under the TDT intensity transformation corresponding to A; E-H are arranged similarly for the case of MLO mammogram in E. Note that the overlap between manual and automatic segmentations is coloured in white.

is limited in its ability to translate the MRI contrast into the one characteristic of X-ray

Table 5.3: TRE values (in millimetres) of CAR procedure for 10 cases of CC mammograms under different intensity transformations and similarity measures

| Measure | MI | | SSD | |
|---|---|---|---|---|
| Image type | EXR image | TDT image | EXR image | TDT image |
| Case 1 | 8.12 | 6.89 | 6.39 | 3.64 |
| Case 2 | 11.13 | 11.19 | 10.73 | 4.06 |
| Case 3 | 9.00 | 7.11 | 8.97 | 6.51 |
| Case 4 | 7.05 | 8.47 | 6.76 | 1.44 |
| Case 5 | 7.94 | 8.03 | 5.94 | 2.48 |
| Case 6 | 5.41 | 6.48 | 3.86 | 1.88 |
| Case 7 | 9.33 | 4.70 | 10.30 | 2.55 |
| Case 8 | 13.27 | 9.67 | 13.24 | 12.54 |
| Case 9 | 14.12 | 14.50 | 12.51 | 8.24 |
| Case 10 | 3.12 | 5.21 | 2.93 | 4.83 |
| Mean | 8.85 | 8.22 | 8.16 | 4.81 |
| STD | 3.36 | 2.94 | 3.53 | 3.44 |

imaging. As a result, this scenario still resembles the case of inter-modality registration, for which the use SSD is known to be inadequate [163].

Since one of the main contributions of this paper is the introduction of a new method of predicting the global displacement $\varphi_{\text{glb}}$, the question of the quality of this prediction should not be overlooked. To this end, the computation of TRE was repeated for the case when $\varphi = \varphi_{\text{glb}}$, i.e., with the effect of $\varphi_{\text{res}}$ ignored. Surprisingly enough, in this suboptimal scenario, the quality of image registration was found to be relatively high, with the average values of TRE equal to 12.4 mm and 14 mm for CC and MLO mammograms, respectively. At the same time, the contribution of $\varphi_{\text{res}}$ has been found to be directly dependent on the quality of predicted $\tilde{\varphi}_{\text{glb}}$. Moreover, it was observed that poor predictions can, in effect, worsen the results of final estimation. Thus, for instance, in case 2, the prediction alone produced a relatively large error of 17 mm, which further declined to 19.49 mm after the application of $\varphi_{\text{res}}$.

Another important observation has been made in connection to the performance of the TDT model in the case of almost entirely fatty breasts. In such situations, due to the virtual lack of fibroglandular tissue, the intensity model had difficulty producing sufficiently salient features which were necessary to guide the process of deformation. As a result, the

Table 5.4: TRE values (in millimetres) of CAR procedure for 10 cases of MLO mammograms under different intensity transformations and similarity measures

| Measure | MI | | SSD | |
|---|---|---|---|---|
| Image type | EXR image | TDT image | EXR image | TDT image |
| Case 1 | 16.43 | 18.34 | 16.36 | 9.02 |
| Case 2 | 15.69 | 13.07 | 15.95 | 19.49 |
| Case 3 | 4.29 | 6.35 | 4.97 | 6.67 |
| Case 4 | 13.60 | 13.63 | 9.19 | 4.03 |
| Case 5 | 4.49 | 4.56 | 3.53 | 3.44 |
| Case 6 | 10.59 | 10.25 | 10.53 | 10.44 |
| Case 7 | 9.39 | 8.18 | 10.36 | 3.36 |
| Case 8 | 12.48 | 10.79 | 12.59 | 8.64 |
| Case 9 | 13.59 | 13.18 | 11.45 | 4.12 |
| Case 10 | 6.98 | 7.01 | 6.47 | 6.73 |
| Mean | 10.75 | 10.54 | 10.14 | 7.59 |
| STD | 4.38 | 4.15 | 4.28 | 4.88 |

estimation of $\varphi_{\text{res}}$ was found to be prone to overfitting. Fortunately, the latter can be easily prevented by requiring the spline resolution $\Delta$ to be low-bounded by a predefined distance, e.g., 8 mm. An additional way to regularize the estimation of $\varphi_{\text{res}}$ is to require the transformation to be diffeomorphic and, hence, topology preserving. As demonstrated in ([25]), to enforce this property, it is sufficient to upper bound the spline coefficients so that $|c^l_{\mathbf{n}}| \leq \kappa/\Delta$, for all $l \in \{x, y, z\}$, with $\kappa = 2.48$. Both strategies have been found to be simple and effective remedies to avoid spurious variations in the final deformation field.

## 5.4 Additional Observations

Unfortunately, perfect alignment between (projected) MRI scans and mammograms are impossible to achieve in practice for several reasons. First of all, due to different imaging mechanisms used by these modalities as well as their different spatial resolutions, one modality may capture content which does not appear in the other modality. For instance, blood vessels are often seen in mammography, while being virtually indiscernible in MRI scans. Consequently, in contrast to original mammograms, their MRI-based "emulations" cannot be expected to contain these details. The second reason is that even if one can

accurately extract the lesion's boundary in both MRI and mammogram images, these boundaries may not be the same in both images. It is because MRI and mammography measure different physical properties of the breast tissue. In general, the projections of the MRI annotations appear different than those of the X-ray images. This difference could be partially explained by the fact that the two modalities measure different physical properties of the tissue and also by the fact that, in general, it is much harder for a radiologist to annotate 3-D structures in MRI volume. Moreover, the size of malignant lesions on X-ray mammography tends to be underestimated, while MRI measurements have been repeatedly shown to be larger, albeit more accurate [98]. Furthermore, when breast lesions are deformed during registration, their radius can be reduced in the direction of the projection and consequently increased in the perpendicular plane.

Following [40] and [98], we also studied the influence of the position of the lesions within the breast. Figure 5.8 shows the relative position of lesions of the ten cases used in this study. The boundary of the projected MRI volume or mammogram is shown by a semi-half circle. One can see that the lesions are nearly uniformly distributed across the breast, with some of them appearing closer to either the boundary or the center than the others. We examined the relation between the values of TRE and the lesion's position with respect to the pectoral boundary as well as the $x$-axis. However, in none of our experimental scenarios, the relation was found to be statistically significant. To support this conclusion, Figure 5.9 shows the values of TRE as a function of the distance between the lesions and pectoral boundary of different subjects in the case of SSD-based registration under the TDT intensity model. One can see that in the case of both CC and MLO projections, the error varies around the 8 mm mark, with no apparent trends. Note that a similar conclusion was made in the studies relying on FEM modelling.

It should also be noted that, in the literature on MRI to mammogram registration, it is not uncommon to use relatively small datasets. Thus, for example, the results in [40] and [98] were obtained based on 10 subject cases, while the experiments in [137] involved only 5 CC and 4 MLO mammographic images. Thus, from the viewpoint of the statistical consistency of our comparative analysis, the use of 10 cases in the present study seems to be a reasonable choice. It goes without saying that a more comprehensive evaluation of the proposed method requires the use of a large collection of data images. The same comment can be also extended to the use of TRE as a performance metric. In particular, in the current work, the error was computed based on the distance between the centroids of manually delineated lesions and their MRI-based counterparts. Although this definition facilitates straightforward comparison with previously reported results, it is clear that computing the error based on a set of anatomical landmarks could provide a more accurate way to perform a quantitative assessment of MRI to mammogram registration.

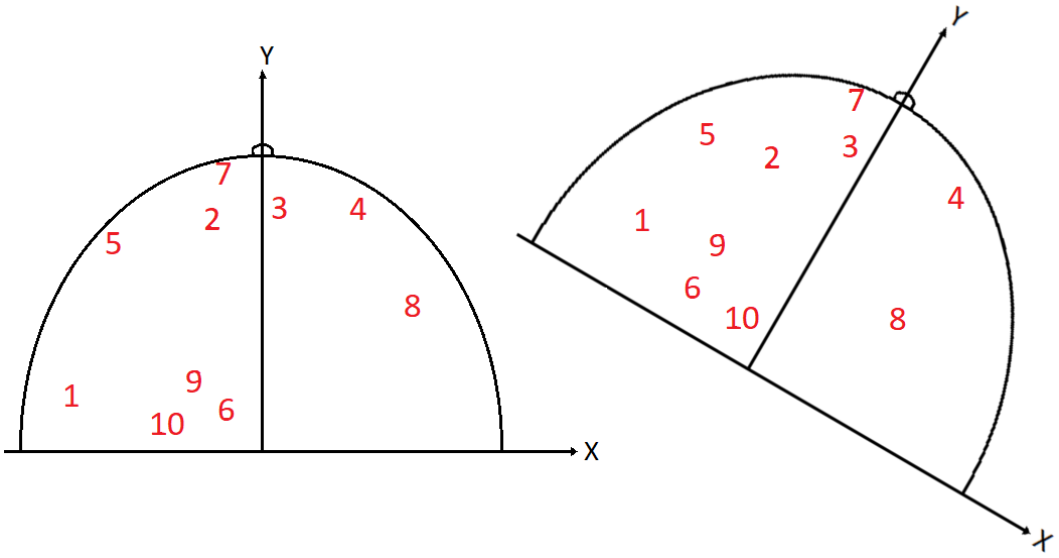


Figure 5.8: Relative positions of breast lesions in studied case: (leftmost) CC projections and (rightmost) MLO projections.

The case of MLO mammograms deserves special attention. In particular, as opposed to CC projections, the acquisition of MLO mammographic scans entails rotation of the breast around two axes (i.e., roll and in-plane). However, while the rotation around the $y$-axis (roll) is registered by the scanner (and, hence, known), the extent of in-plane rotation is rarely available in practice. Following the suggestions in early studies, in the course of our computation of $\tilde{\varphi}_{\text{glb}}$, the value of in-plane rotation was assumed to be fixed and equal to $20^{\circ}$ for all study cases. Needless to say, the above value is rather approximative, which is likely to be a source of sizeable estimation errors. Moreover, for obvious reasons, the effect of gravitational forces on the deformation of breast boundary is much more pronounced in MLO mammograms than in their CC counterparts. This effect, however, is not explicitly accounted by the proposed mechanism of prediction of $\varphi_{\text{glb}}$, which unavoidably affects its accuracy as well. It is for these reasons that the values of TRE in the case of MLO mammograms happen to be notably worse as compared to the case of CC projections. Accordingly, rectifying the adverse effects of the above limitations constitutes a principal direction of our ongoing research.

The computational time of the proposed registration method (including preprocessing, global, and residual deformation estimation) using MATLAB on a CPU (Intel(R) Core (TM) -i7 6500U) is about 50 minutes on average. Roughly, it takes about 5 minutes to complete preprocessing, 25 minutes and 20 minutes to accomplish the global and residual

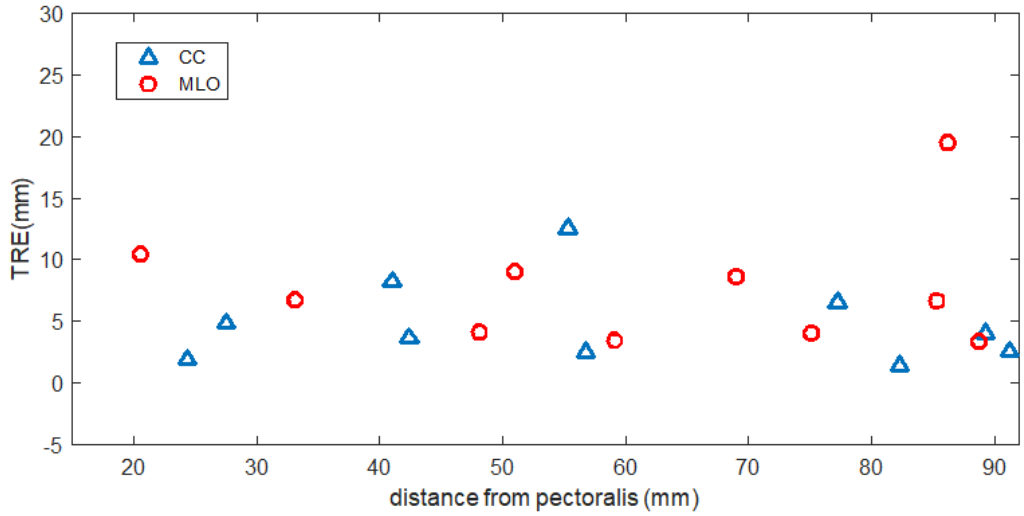


Figure 5.9: TRE as a function of the distance of lesions from the pectoral muscle. Each marker indicates the TRE value in the case of SSD-based registration under TDT intensity model.

deformation estimations, respectively. At the same time, FEM-based methods can only complete a single registration task in an hour or a few hours, even using numerical accelerations by means of GPUs. For instance, the computational time of the method proposed by [40] (after extracting the biomechanical model) is approximately one hour using a GPU with 128 threads. Another point that deserves noting is that the proposed algorithms have been implemented in MATLAB which suggests the possibility of substantial acceleration using a low level programming language like C and/or specialized hardware. Therefore, another important advantage of the proposed method is the ability to be easily integrated in clinics and run in an acceptable time with regular CPUs in hospitals.

# Chapter 6

# Discussion and Conclusion

In this thesis, a general framework for intensity-based registration of breast MRI images with X-ray mammograms was presented. For this purpose, an original and computationally effective approach have been proposed to estimate the breast deformation and, consequently, determine the correspondences between these imaging modalities. The principle idea behind our approach was the notion that the significant part of the breast deformation (which is called global deformation) does not depend on the breasts' properties, and it is almost common among subjects, which makes it predictable. The idea of splitting the total deformation into global and residual components provides an efficient and straightforward solution to the problem. We investigated two different mathematical approaches to predicting the global deformation, in which we constructed a 3-D surface rendering the shape of the deformed breast in its compressed state. In the first approach a superquadratic function was used to represent the surface of the deformed breast tissue and then estimated the global deformation by registering the surface of breast tissue in the MRI volume to this model. On the other hand, our second approach toward estimating the global deformation was by temporal evolving of the breast surface, where the changes of the breast boundary is followed when it is gradually compressed between two imaginary paddles. To refine this prediction, the process of estimating the global deformation was followed by the computation of the residual deformation. The residual deformation is patient-specific, with a significantly smaller magnitude in comparison to the global deformation.

Using visual and quantitative analysis, it was showed that while earlier approaches to this problem depended on complex biomechanical modelling based on FEM formulation, the better registration accuracy can be accomplished by substantially simpler means. It has been demonstrated that both of our proposed solutions, superquadratic model and CAR procedure, for global deformation estimation are efficient in accounting for the major

part of the breast deformation in mammography. In both cases, the registration accuracy is comparable with the state of the art. Also the effect of different intensity transformation models and similarity measures has been investigated, with the best results favouring the use of TDT and SSD, where the average TRE was 4.81 mm ± 3.44 mm for registering MRI volume to CC- mammogram and 7.59 mm ± 4.88 mm for registering MRI volume to the MLO-mammogram. These results, not only, are better than those by FEM-based methods but also they are reproducible as our proposed framework is generic with minimal preprocessing interaction and does not depend on any initialization. In addition, it is fully automated with no interactive steps. Furthermore, from the computational point of view, it is considerably lighter than FEM-based methods, and, as a result, it can be easily integrated in clinics.

The use of the proposed method would not have been possible without investing in preprocessing and data preparation. It was observed that existing solutions toward required preprocessings are inefficient in several ways, therefore it was attempted to address such shortcomings. To this end, two new ways of approaching the problem of whole breast segmentation in MRI and mammography scans were discussed. A breast MRI volume contains much irrelevant information which should be excluded prior to deformation estimation. We introduced a fully automatic and computationally efficient approach to the problem of segmenting breast tissue from the background and other nearby organs existing in MRI images. The performance of the proposed method has been shown to be almost independent of breast type, which represents a considerable advance over previous breast segmentation approaches. On the other hand, to exclude pectoralis major in MLO mammogram, an original solution has been developed by taking advantage of convolutional neural networks and a graph-based search. It has been demonstrated that the proposed two-step approach is advantageous in several ways. First of all, it does not need any analytical assumptions regarding the geometry of pectoral boundary, which are prone to errors due to the effects of inter-subject variability. Second, the subsequent use of graph-based processing allows one to recover the pectoral boundary at a "single-pixel" resolution in a fully automatic way which was an improvement over existing methods. Lastly, our experimental results have demonstrated the superior performance of the proposed solution over the state-of-the-art, especially when it comes to difficult cases of low-contrast mammograms with partially occluded or barely distinguishable pectoral boundaries. In addition to these peprocessings, I came up with a new solution of segmenting the internal structure of the breast tissue in MRI volumes. It has been shown that with a proper formulation one can segment breast tissue in a computationally straightforward manner. Our assessments indicated that, in contrast to other segmentation methods, the proposed solution can remain accurate and stable for a wide range of values SNR as well as the presence of

a sizable bias field.

# Chapter 7

# Summary and Future Research

In summary, we addressed the problem of fusing information from breast MRI and mammography scans. A novel mathematical framework has been developed which can establish spatial correspondences between images from these modalities. One of the main advantages of the proposed method is that it does not rely on a specific model for each patient, which renders it generic. In addition, it does not require initiations by the use, and it is capable of being standardized. In terms of computation complexity, it is much lighter with respect to traditional registration frameworks, which makes it practical and, as a result, it can be potentially easily incorporated into clinical practice.

The proposed approach has been evaluated on a relatively small number of subjects. Also, data acquisition had been done in a specific hospital using a single particular scanner. It is clear that computed registration error and even the correlation between TRE and the positions of lesions may alter with a dataset containing more cases. For a robust validation and to ensure that this method is applicable in clinical use, it should be tested on a wide range of cases. Furthermore, in this work, the registration accuracy is computed based on the distance of the center of the lesions. Computing the TRE with respect to a net of landmarks distributed over the surface of the breast can reflect better accuracy measurement. Therefore, as a future work, the algorithm should be tested on a larger dataset using more landmarks. Another possible future work can be finding the correspondences between the mammograms acquired from different views. Most of the previous CC to MLO registration techniques treat this problem as a 2-D/2-D correspondence task (so assuming one-to-one correspondence), either by mapping texture and intensity measures or by using a distance transform from features such as the pectoral muscle and the nipple position. Any 2-D transformation model is inappropriate for this task because X-ray mammograms are projection images, and a 2-D technique cannot model the 3-D physical transformation

of the tissue. Assuming that an MRI and two mammograms (either CC and MLO, or temporal) of the same patient are available, then one can perform two registration tasks, to relate the MRI to the X-ray mammograms independently. After having acquired the two transformations, one can use them to map coordinates from one X-ray image to the other.

In this dissertation, only the pre-contrast DCE-MRI of the breast for registration have been used. The combination of a post-contrast image and a pre-contrast image may provide precise details about the location and shape of tumors. In future research, the advantage of integrating information from post-contrast images to assign a different attenuation coefficient to tumorous tissue than standard fibroglandular structures (thereby improving contrast and producing more accurate X-ray simulations from the MRI) could be investigated further. Furthermore, in our proposed CAR procedure toward estimation of the global deformation, it has been assumed that the distribution of breast density is uniform. However, for a more realistic deformation, one can use the segmented MRI from preprocessing step and take to account the real distribution of the dense tissue. This can be another research direction for future works. In this work, basically the mammogram using information from MRI has been enhanced. As another future study, one can also consider transferring contrast from mammography to MRI. Even though this sounds straightforward as the map between them has already been computed, it still needs to be explored and discussed more.

The proposed MRI to X-ray mammography registration framework can be used as part of a clinical method to aid radiologists in combining the diagnostic information provided by the two modalities and ultimately enhance breast cancer identification and diagnosis. The radiologists will be able to navigate across the MRI and display the corresponding spot on the CC and MLO view mammograms either as a point position or as a disc with a radius equivalent to the mean registration error derived from a validation test using our proposed algorithm as part of the viewing method. This technique will be especially useful for detecting mammographically occult lesions as well as further evaluating lesions that have been found mammographically. The algorithm needs to executed only once offline, and consequently, the results can be saved as a transition model, which allows for real-time multimodal visualization. Another possible application for our framework is to allow X-ray-driven biopsy for lesions that are not evident or noticeable on ultrasound or X-ray. These patients are currently subjected to MRI-guided biopsy which is costly, time-consuming, and inconvenient for clinical practice. A lesion apparent in the MRI could be detected and projected onto the X-ray mammogram if an MRI to X-ray registration framework with adequate precision was available. This will allow the radiologist to do an X-ray-guided biopsy, which would be a simpler, less invasive, and more readily accessible

technique than an MRI.

# References


[1] Mohamed Abdel-Nasser, Antonio Moreno, and Domenec Puig. Temporal mammogram image registration using optimized curvilinear coordinates. *Computer methods and programs in biomedicine*, 127:1–14, 2016.

[2] Michael Alvarado, Elissa Ozanne, and Laura Esserman. Overdiagnosis and overtreatment of breast cancer. *American Society of Clinical Oncology Educational Book*, 32(1):e40–e45, 2012.

[3] Vincent Arsigny, Xavier Pennec, and Nicholas Ayache. Polyrigid and polyaffine transformations: a novel geometrical tool to deal with non-rigid deformations–application to the registration of histological slices. *Medical image analysis*, 9(6):507–523, 2005.

[4] John Ashburner and Karl J Friston. Nonlinear spatial normalization using basis functions. *Human brain mapping*, 7(4):254–266, 1999.

[5] Vijay Badrinarayanan, Alex Kendall, and Roberto Cipolla. Segnet: A deep convolutional encoder-decoder architecture for image segmentation. *IEEE transactions on pattern analysis and machine intelligence*, 39(12):2481–2495, 2017.

[6] H Baluwala, Duane TK Malcolm, Anthony J Doyle, Poul MF Nielsen, and Martyn P Nash. Breast mri segmentation using supervoxel classification. In *Proc. 3rd MICCAI International Workshop on Breast Image Analysis (MICCAI2015 Workshop)*, pages 113–120, 2015.

[7] Alan H Barr. Superquadrics and angle-preserving transformations. *IEEE Computer graphics and Applications*, 1(1):11–23, 1981.

[8] Jonathan KP Begley, Thomas W Redpath, Patrick J Bolan, and Fiona J Gilbert. In vivo proton magnetic resonance spectroscopy of breast cancer: a review of the literature. *Breast Cancer Research*, 14(2):207, 2012.

[9] Christian P Behrenbruch, Kostas Marias, Paul A Armitage, Margaret Yam, Niall Moore, Ruth E English, Jane Clarke, and Michael Brady. Fusion of contrast-enhanced breast mr and mammographic imaging data. *Medical Image Analysis*, 7(3):311–340, 2003.

[10] Wendie A Berg, Jeffrey D Blume, Jean B Cormack, Ellen B Mendelson, Daniel Lehrer, Marcela Böhm-Vélez, Etta D Pisano, Roberta A Jong, W Phil Evans, Marilyn J Morton, et al. Combined screening with ultrasound and mammography vs mammography alone in women at elevated risk of breast cancer. *Jama*, 299(18):2151–2163, 2008.

[11] RG Blanks, MG Wallis, and RM Given-Wilson. Observer variability in cancer detection during routine repeat (incident) mammographic screening in a study of two versus one view mammography. *Journal of Medical Screening*, 6(3):152–158, 1999.

[12] Fred L. Bookstein. Principal warps: Thin-plate splines and the decomposition of deformations. *IEEE Transactions on pattern analysis and machine intelligence*, 11(6):567–585, 1989.

[13] Vibha Bafna Bora, Ashwin G Kothari, and Avinash G Keskar. Robust automatic pectoral muscle segmentation from mammograms using texture gradient and euclidean distance regression. *Journal of digital imaging*, 29(1):115–125, 2016.

[14] Stephen Boyd, Stephen P Boyd, and Lieven Vandenberghe. *Convex optimization*. Cambridge university press, 2004.

[15] Stephen Boyd, Neal Parikh, and Eric Chu. *Distributed optimization and statistical learning via the alternating direction method of multipliers*. Now Publishers Inc, 2011.

[16] breastcancer. breastcancer.org. https://www.breastcancer.org/. Accessed: 2016.

[17] Wolfgang Buchberger, Andreas Niehoff, Peter Obrist, Petra DeKoekkoek-Doll, and Martina Dünser. Clinically and mammographically occult breast lesions: detection and classification with high-resolution sonography. In *Seminars in Ultrasound, CT and MRI*, volume 21, pages 325–336. Elsevier, 2000.

[18] JW Byng, NF Boyd, L Little, G Lockwood, E Fishell, RA Jong, and MJ Yaffe. Symmetry of projection in the quantitative analysis of mammographic images. *European journal of cancer prevention: the official journal of the European Cancer Prevention Organisation (ECP)*, 5(5):319–327, 1996.

[19] Richard H Byrd, Peihuang Lu, Jorge Nocedal, and Ciyou Zhu. A limited memory algorithm for bound constrained optimization. *SIAM Journal on Scientific Computing*, 16(5):1190–1208, 1995.

[20] K Santle Camilus, VK Govindan, and PS Sathidevi. Computer-aided identification of the pectoral muscle in digitized mammograms. *Journal of digital imaging*, 23(5):562–580, 2010.

[21] Chunxiao Chen, Gao Liu, Jing Wang, and Gail Sudlow. Shape-based automatic detection of pectoral muscle boundary in mammograms. *Journal of medical and biological engineering*, 35(3):315–322, 2015.

[22] Dai-Qiang Chen, Hui Zhang, and Li-Zhi Cheng. A fast fixed point algorithm for total variation deblurring and segmentation. *Journal of Mathematical Imaging and Vision*, 43(3):167–179, 2012.

[23] Zhili Chen and Reyer Zwiggelaar. Segmentation of the breast region with pectoral muscle removal in mammograms. *Medical Image Understanding and Analysis (MIUA)*, pages 71–76, 2010.

[24] Jin-Young Choi, Jeong-Min Lee, and Claude B Sirlin. Ct and mr imaging diagnosis and staging of hepatocellular carcinoma: part ii. extracellular agents, hepatobiliary agents, and ancillary imaging features. *Radiology*, 273(1):30–50, 2014.

[25] Yongchoel Choi and Seungyong Lee. Injectivity conditions of 2d and 3d uniform cubic b-spline functions. *Graphical models*, 62(6):411–427, 2000.

[26] Thomas H Cormen, Charles E Leiserson, Ronald L Rivest, and Clifford Stein. *Introduction to algorithms*. MIT press, 2009.

[27] Arthur P Dempster, Nan M Laird, and Donald B Rubin. Maximum likelihood from incomplete data via the em algorithm. *Journal of the Royal Statistical Society: Series B (Methodological)*, 39(1):1–22, 1977.

[28] J. Deng, W. Dong, R. Socher, L.-J. Li, K. Li, and L. Fei-Fei. ImageNet: A Large-Scale Hierarchical Image Database. In *CVPR09*, 2009.

[29] Yago Diez, Arnau Oliver, Xavier Lladó, Jordi Freixenet, Joan Marti, Joan Carles Vilanova, and Robert Marti. Revisiting intensity-based image registration applied to mammography. *IEEE Transactions on Information Technology in Biomedicine*, 15(5):716–725, 2011.

[30] Nicholas Dowson, Timor Kadir, and Richard Bowden. Estimating the joint statistics of images using nonparametric windows with application to registration using mutual information. *IEEE Transactions on Pattern Analysis and Machine Intelligence*, 30(10):1841–1857, 2008.

[31] Anastasia Dubrovina, Pavel Kisilev, Boris Ginsburg, Sharbell Hashoul, and Ron Kimmel. Computational mammography using deep neural networks. *Computer Methods in Biomechanics and Biomedical Engineering: Imaging & Visualization*, 6(3):243–247, 2018.

[32] Björn Eiben, Lianghao Han, J Hipwell, Thomy Mertzanidou, Sven Kabus, Thomas Bülow, Cristian Lorenz, GM Newstead, Hiroyuki Abe, Mohammed Keshtgar, et al. Biomechanically guided prone-to-supine image registration of breast mri using an estimated reference state. In *2013 IEEE 10th international symposium on biomedical imaging*, pages 214–217. IEEE, 2013.

[33] Gokhan Ertas, Simon J Doran, and Martin O Leach. A computerized volumetric segmentation method applicable to multi-centre mri data to support computer-aided breast tissue analysis, density assessment and lesion localization. *Medical & biological engineering & computing*, 55(1):57–68, 2017.

[34] RJ Ferrari, AF Frere, RM Rangayyan, JEL Desautels, and RA Borges. Identification of the breast boundary in mammograms using active contour models. *Medical and Biological Engineering and Computing*, 42(2):201–208, 2004.

[35] Bernd Fischer and Jan Modersitzki. A unified approach to fast image registration and a new curvature based registration technique. *Linear Algebra and its applications*, 380:107–124, 2004.

[36] J Michael Fitzpatrick and Jay B West. The distribution of target registration error in rigid-body point-based registration. *IEEE transactions on medical imaging*, 20(9):917–927, 2001.

[37] Cristina Gallego and Anne L Martel. Automatic model-based 3d segmentation of the breast in mri. In *Medical Imaging 2011: Image Processing*, volume 7962, page 796215. International Society for Optics and Photonics, 2011.

[38] Rui Gan, Jue Wu, Albert CS Chung, CH Simon, and William M Wells. Multiresolution image registration based on kullback-leibler distance. In *International Conference on Medical Image Computing and Computer-Assisted Intervention*, pages 599–606. Springer, 2004.

[39] Eloy Garcia, Yago Diez, Oliver Diaz, Xavier Llado, Albert Gubern-Mérida, Robert Martí, Joan Martí, and Arnau Oliver. Multimodal breast parenchymal patterns correlation using a patient-specific biomechanical model. *IEEE transactions on medical imaging*, 37(3):712–723, 2018.

[40] Eloy García, Yago Diez, Oliver Diaz, Xavier Lladó, Albert Gubern-Mérida, Robert Martí, Joan Martí, and Arnau Oliver. Breast mri and x-ray mammography registration using gradient values. *Medical image analysis*, 54:76–87, 2019.

[41] Eloy García, Yago Diez, Oliver Diaz, Xavier Lladó, Robert Martí, Joan Martí, and Arnau Oliver. A step-by-step review on patient-specific biomechanical finite element models for breast mri to x-ray mammography registration. *Medical physics*, 45(1):e6–e31, 2018.

[42] D. J. Gavaghan, J. P. Whiteley, S. J. Chapman, J. M. Brady, and P. Pathmanathan. Predicting tumor location by modeling the deformation of the breast. *IEEE Transactions on Biomedical Engineering*, 55(10):2471–2480, 2008.

[43] Anuradha Godavarty, Alan B Thompson, Ranadhir Roy, Mikhail Gurfinkel, Margaret J Eppstein, Chaoyang Zhang, and Eva Marie Sevick-Muraca. Diagnostic imaging of breast cancer using fluorescence-enhanced optical tomography: phantom studies. *Journal of biomedical optics*, 9(3):488–497, 2004.

[44] Paula B Gordon. Ultrasound for breast cancer screening and staging. *Radiologic Clinics*, 40(3):431–441, 2002.

[45] Albert Gubern-Merida, Michiel Kallenberg, Ritse M Mann, Robert Marti, and Nico Karssemeijer. Breast segmentation and density estimation in breast mri: a fully automatic framework. *IEEE journal of biomedical and health informatics*, 19(1):349–357, 2014.

[46] Albert Gubern-Merida, Michiel Kallenberg, Ritse M Mann, Robert Marti, and Nico Karssemeijer. Breast segmentation and density estimation in breast mri: a fully automatic framework. *ieee journal of biomedical and health informatics*, 19(1):349–357, 2015.

[47] Albert Gubern-Mérida, Michiel Kallenberg, R Marti, and Nico Karssemeijer. Fully automatic fibroglandular tissue segmentation in breast mri: atlas-based approach. In *MICCAI Workshop: breast image analysis*, pages 73–80, 2011.

[48] Hákon Gudbjartsson and Samuel Patz. The rician distribution of noisy mri data. *Magnetic resonance in medicine*, 34(6):910–914, 1995.

[49] Régis Guillemaud and Michael Brady. Estimating the bias field of mr images. *IEEE Transactions on Medical imaging*, 16(3):238–251, 1997.

[50] Zhihui Guo, Ling Zhang, Le Lu, Mohammadhadi Bagheri, Ronald M Summers, Milan Sonka, and Jianhua Yao. Deep logismos: deep learning graph-based 3d segmentation of pancreatic tumors on ct scans. In *2018 IEEE 15th international symposium on biomedical imaging (ISBI 2018)*, pages 1230–1233. IEEE, 2018.

[51] Valentin Hamy, Nikolaos Dikaios, Shonit Punwani, Andrew Melbourne, Arash Latifoltojar, Jesica Makanyanga, Manil Chouhan, Emma Helbren, Alex Menys, Stuart Taylor, et al. Respiratory motion correction in dynamic mri using robust data decomposition registration–application to dce-mri. *Medical image analysis*, 18(2):301–313, 2014.

[52] Lianghao Han, John H Hipwell, Björn Eiben, Dean Barratt, Marc Modat, Sebastien Ourselin, and David J Hawkes. A nonlinear biomechanical model based registration method for aligning prone and supine mr breast images. *IEEE transactions on medical imaging*, 33(3):682–694, 2013.

[53] Lianghao Han, John H Hipwell, Björn Eiben, Dean Barratt, Marc Modat, Sebastien Ourselin, and David J Hawkes. A nonlinear biomechanical model based registration method for aligning prone and supine mr breast images. *IEEE transactions on medical imaging*, 33(3):682–694, 2014.

[54] Arthur G Haus. Historical technical developments in mammography. *Technology in cancer research & treatment*, 1(2):119–126, 2002.

[55] Paul Hayton, Michael Brady, Lionel Tarassenko, and Niall Moore. Analysis of dynamic mr breast images using a model of contrast enhancement. *Medical image analysis*, 1(3):207–224, 1997.

[56] Ralph Highnam and J Michael Brady. *Mammographic image analysis*, volume 14. Springer Science & Business Media, 2012.

[57] Ralph Highnam, Michael Brady, Martin J Yaffe, Nico Karssemeijer, and Jennifer Harvey. Robust breast composition measurement-volpara tm. In *International workshop on digital mammography*, pages 342–349. Springer, 2010.

[58] Peter Hogg, Judith Kelly, and Claire Mercer. *Digital mammography: a holistic approach*. Springer, 2015.

[59] Torsten Hopp, Matthias Dietzel, Pascal A Baltzer, P Kreisel, Werner A Kaiser, Hartmut Gemmeke, and Nicole V Ruiter. Automatic multimodal 2d/3d breast image registration using biomechanical fem models and intensity-based optimization. *Medical image analysis*, 17(2):209–218, 2013.

[60] Gerhard Huisken. Asymptotic-behavior for singularities of the mean-curvature flow. *Journal of Differential Geometry*, 31(1):285–299, 1990.

[61] Gerhard Huisken et al. Flow by mean curvature of convex surfaces into spheres. *Journal of Differential Geometry*, 20(1):237–266, 1984.

[62] Debra M Ikeda, Nola M Hylton, Karen Kinkel, Mary G Hochman, Christiane K Kuhl, Werner A Kaiser, Jeffrey C Weinreb, Stanley F Smazal, Hadassah Degani, Petra Viehweg, et al. Development, standardization, and testing of a lexicon for reporting contrast-enhanced breast magnetic resonance imaging studies. *Journal of Magnetic Resonance Imaging: An Official Journal of the International Society for Magnetic Resonance in Medicine*, 13(6):889–895, 2001.

[63] Bonnie N Joe and Edward A Sickles. The evolution of breast imaging: past to present. *Radiology*, 273(2S):S23–S44, 2014.

[64] Paul C Johns and Martin J Yaffe. X-ray characterisation of normal and neoplastic breast tissues. *Physics in Medicine & Biology*, 32(6):675, 1987.

[65] Jaber Juntu, Jan Sijbers, Dirk Van Dyck, and Jan Gielen. Bias field correction for mri images. In *Computer Recognition Systems*, pages 543–551. Springer, 2005.

[66] Prem Kumar Kalra, Nirmal Kumar, et al. An automatic image registration scheme using tsallis entropy. *Biomedical Signal Processing and Control*, 5(4):328–335, 2010.

[67] SR Kannan, S Ramathilagam, and A Sathya. Robust fuzzy c-means in classifying breast tissue regions. In *2009 International Conference on Advances in Recent Technologies in Communication and Computing*, pages 543–545. IEEE, 2009.

[68] Nico Karssemeijer. Automated classification of parenchymal patterns in mammograms. *Physics in medicine & biology*, 43(2):365, 1998.

[69] Michael Khazen, Ruth ML Warren, Caroline RM Boggis, Emilie C Bryant, Sadie Reed, Iqbal Warsi, Linda J Pointon, Gek E Kwan-Lim, Deborah Thompson, Ros Eeles, et al. A pilot study of compositional analysis of the breast and estimation of breast mammographic density using three-dimensional t1-weighted magnetic resonance imaging. *Cancer Epidemiology and Prevention Biomarkers*, 17(9):2268–2274, 2008.

[70] Daniel B Kopans, Cynthia A Swann, George White, Kathreen A McCarthy, Deborah A Hall, Stephen J Belmonte, and William Gallagher. Asymmetric breast tissue. *Radiology*, 171(3):639–643, 1989.

[71] Christiane K Kuhl, Heribert B Bieling, Jurgen Gieseke, Burkhard P Kreft, Torsten Sommer, Gotz Lutterbey, and Hans H Schild. Healthy premenopausal breast parenchyma in dynamic contrast-enhanced mr imaging of the breast: normal contrast medium enhancement and cyclical-phase dependency. *Radiology*, 203(1):137–144, 1997.

[72] Rakesh Kumar, J Charles Asmuth, Keith Hanna, James R Bergen, C Hulka, Daniel B Kopans, R Weisskoff, and Richard H Moore. Application of 3d registration for detecting lesions in magnetic resonance breast scans. In *Medical Imaging 1996: Image Processing*, volume 2710, pages 646–657. International Society for Optics and Photonics, 1996.

[73] Sze Man Kwok, Ramachandran Chandrasekhar, Yianni Attikiouzel, and Mary T Rickard. Automatic pectoral muscle segmentation on mediolateral oblique view mammograms. *IEEE transactions on medical imaging*, 23(9):1129–1140, 2004.

[74] Angela WC Lee, Vijayaraghavan Rajagopal, Thiranja P Babarenda Gamage, Anthony J Doyle, Poul MF Nielsen, and Martyn P Nash. Breast lesion co-localisation between x-ray and mr images using finite element modelling. *Medical image analysis*, 17(8):1256–1264, 2013.

[75] Nancy A Lee, Henry Rusinek, Jeffrey Weinreb, Ramesh Chandra, Hildegard Toth, Cory Singer, and Gillian Newstead. Fatty and fibroglandular tissue volumes in the breasts of women 20-83 years old: comparison of x-ray mammography and computer-assisted mr imaging. *AJR. American journal of roentgenology*, 168(2):501–506, 1997.

[76] Rebecca Sawyer Lee, Francisco Gimenez, Assaf Hoogi, Kanae Kawai Miyake, Mia Gorovoy, and Daniel L Rubin. A curated mammography data set for use in computer-aided detection and diagnosis research. *Scientific data*, 4:170177, 2017.

[77] Christophe Leys, Christophe Ley, Olivier Klein, Philippe Bernard, and Laurent Licata. Detecting outliers: Do not use standard deviation around the mean, use absolute deviation around the median. *Journal of Experimental Social Psychology*, 49(4):764–766, 2013.

[78] Haozhao Li. The volume-preserving mean curvature flow in euclidean space. *Pacific journal of mathematics*, 243(2):331–355, 2009.

[79] Yanfeng Li, Houjin Chen, Yongyi Yang, Lin Cheng, and Lin Cao. A bilateral analysis scheme for false positive reduction in mammogram mass detection. *Computers in biology and medicine*, 57:84–95, 2015.

[80] Y. Liu, M. Cheng, X. Hu, K. Wang, and X. Bai. Richer convolutional features for edge detection. In *2017 IEEE Conference on Computer Vision and Pattern Recognition (CVPR)*, pages 5872–5881, 2017.

[81] Y Liu, MM Cheng, X Hu, JW Bian, L Zhang, X Bai, and J Tang. Richer convolutional features for edge detection. *IEEE transactions on pattern analysis and machine intelligence*, 41(8):1939–1946, 2019.

[82] Dirk Loeckx, Pieter Slagmolen, Frederik Maes, Dirk Vandermeulen, and Paul Suetens. Nonrigid image registration using conditional mutual information. *IEEE transactions on medical imaging*, 29(1):19–29, 2010.

[83] Jonathan Long, Evan Shelhamer, and Trevor Darrell. Fully convolutional networks for semantic segmentation. In *Proceedings of the IEEE conference on computer vision and pattern recognition*, pages 3431–3440, 2015.

[84] SJ Lord, W Lei, P Craft, JN Cawson, I Morris, S Walleser, A Griffiths, S Parker, and N Houssami. A systematic review of the effectiveness of magnetic resonance imaging (mri) as an addition to mammography and ultrasound in screening young women at high risk of breast cancer. *European journal of cancer*, 43(13):1905–1917, 2007.

[85] George G Lorentz. *Bernstein polynomials*. American Mathematical Soc., 2013.

[86] Jianwen Luo and Elisa E Konofagou. A fast normalized cross-correlation calculation method for motion estimation. *IEEE transactions on ultrasonics, ferroelectrics, and frequency control*, 57(6):1347–1357, 2010.

[87] Fei Ma, Limin Yu, Mariusz Bajger, and Murk J Bottema. Incorporation of fuzzy spatial relation in temporal mammogram registration. *Fuzzy Sets and Systems*, 279:87–100, 2015.

[88] Frederik Maes, Andre Collignon, Dirk Vandermeulen, Guy Marchal, and Paul Suetens. Multimodality image registration by maximization of mutual information. *IEEE transactions on Medical Imaging*, 16(2):187–198, 1997.

[89] Sabine Malur, Susanne Wurdinger, Andreas Moritz, Wolfgang Michels, and Achim Schneider. Comparison of written reports of mammography, sonography and magnetic resonance mammography for preoperative evaluation of breast lesions, with special emphasis on magnetic resonance mammography. *Breast Cancer Research*, 3(1):55, 2000.

[90] Kostas Marias, Christian Behrenbruch, Santilal Parbhoo, Alexander Seifalian, and Michael Brady. A registration framework for the comparison of mammogram sequences. *IEEE Transactions on Medical Imaging*, 24(6):782–790, 2005.

[91] Robert Marti, Reyer Zwiggelaar, Caroline ME Rubin, and Erika RE Denton. Two-dimensional–three-dimensional correspondence in mammography. *Cybernetics and Systems: An International Journal*, 35(1):85–105, 2004.

[92] David Mattes, David R Haynor, Hubert Vesselle, Thomas K Lewellen, and William Eubank. Pet-ct image registration in the chest using free-form deformations. *IEEE transactions on medical imaging*, 22(1):120–128, 2003.

[93] A Melbourne, J Hipwell, M Modat, T Mertzanidou, H Huisman, S Ourselin, and DJ Hawkes. The effect of motion correction on pharmacokinetic parameter estimation in dynamic-contrast-enhanced mri. *Physics in Medicine & Biology*, 56(24):7693, 2011.

[94] Kayla Mendel, Hui Li, Nabihah Tayob, Randa El-Zein, Isabelle Bedrosian, and Maryellen Giger. Temporal mammographic registration for evaluation of architecture changes in cancer risk assessment. In *Medical Imaging 2019: Computer-Aided Diagnosis*, volume 10950, page 1095041. International Society for Optics and Photonics, 2019.

[95] T Mertzanidou, J Hipwell, L Han, H Huisman, N Karssemeijer, and D Hawkes. Mri to x-ray mammography registration using an ellipsoidal breast model and biomechanically simulated compressions. In *MICCAI Workshop on Breast Image Analysis*, pages 161–168, 2011.

[96] Thomy Mertzanidou. *Automatic Correspondence between 2D and 3D Images of the Breast*. PhD thesis, UCL (University College London), 2012.

[97] Thomy Mertzanidou, John Hipwell, M Jorge Cardoso, Xiying Zhang, Christine Tanner, Sebastien Ourselin, Ulrich Bick, Henkjan Huisman, Nico Karssemeijer, and David Hawkes. Mri to x-ray mammography registration using a volume-preserving affine transformation. *Medical image analysis*, 16(5):966–975, 2012.

[98] Thomy Mertzanidou, John Hipwell, Stian Johnsen, Lianghao Han, Bjoern Eiben, Zeike Taylor, Sebastien Ourselin, Henkjan Huisman, Ritse Mann, Ulrich Bick, et al. Mri to x-ray mammography intensity-based registration with simultaneous optimisation of pose and biomechanical transformation parameters. *Medical image analysis*, 18(4):674–683, 2014.

[99] MJ Michell and B Batohi. Role of tomosynthesis in breast imaging going forward. *Clinical radiology*, 73(4):358–371, 2018.

[100] F. Milletari, N. Navab, and S. Ahmadi. V-net: Fully convolutional neural networks for volumetric medical image segmentation. In *2016 Fourth International Conference on 3D Vision (3DV)*, pages 565–571, 2016.

[101] Jan Modersitzki. *Numerical methods for image registration*. Oxford University Press on Demand, 2004.

[102] Pim Moeskops, Jelmer M Wolterink, Bas HM van der Velden, Kenneth GA Gilhuijs, Tim Leiner, Max A Viergever, and Ivana Išgum. Deep learning for multi-task medical image segmentation in multiple modalities. In *International Conference on Medical Image Computing and Computer-Assisted Intervention*, pages 478–486. Springer, 2016.

[103] Debra L Monticciolo, Mary S Newell, Linda Moy, Bethany Niell, Barbara Monsees, and Edward A Sickles. Breast cancer screening in women at higher-than-average risk: recommendations from the acr. *Journal of the American College of Radiology*, 15(3):408–414, 2018.

[104] Inês C Moreira, Igor Amaral, Inês Domingues, António Cardoso, Maria Joao Cardoso, and Jaime S Cardoso. Inbreast: toward a full-field digital mammographic database. *Academic radiology*, 19(2):236–248, 2012.

[105] Benoit Mory, Roberto Ardon, and Jean-Philippe Thiran. Variational segmentation using fuzzy region competition and local non-parametric probability density functions. In *2007 IEEE 11th International Conference on Computer Vision*, pages 1–8. IEEE, 2007.

[106] Olivier Musse, Fabrice Heitz, and Jean-Paul Armspach. Topology preserving deformable image matching using constrained hierarchical parametric models. *IEEE transactions on image processing*, 10(7):1081–1093, 2001.

[107] Mario Mustra and Mislav Grgic. Robust automatic breast and pectoral muscle segmentation from scanned mammograms. *Signal processing*, 93(10):2817–2827, 2013.

[108] Andriy Myronenko and Xubo Song. Point set registration: Coherent point drift. *IEEE transactions on pattern analysis and machine intelligence*, 32(12):2262–2275, 2010.

[109] D Nicholas, K Timor, and B Richard. Estimating the joint statistics of images using nonparametric windows with application to registration using mutual information. *IEEE transaction on pattern analisiss and machineintelegence*, 30(10), 2008.

[110] Ke Nie, Jeon-Hor Chen, Siwa Chan, Man-Kwun I Chau, Hon J Yu, Shadfar Bahri, Tiffany Tseng, Orhan Nalcioglu, and Min-Ying Su. Development of a quantitative method for analysis of breast density based on three-dimensional breast mri. *Medical physics*, 35(12):5253–5262, 2008.

[111] Anton Niukkanen, Otso Arponen, Aki Nykänen, Amro Masarwah, Anna Sutela, Timo Liimatainen, Ritva Vanninen, and Mazen Sudah. Quantitative volumetric k-means cluster segmentation of fibroglandular tissue and skin in breast mri. *Journal of digital imaging*, 31(4):425–434, 2018.

[112] Stanley Osher and Ronald Fedkiw. Signed distance functions. In *Level set methods and dynamic implicit surfaces*, pages 17–22. Springer, 2003.

[113] Bernard J Ostrum, Warren Becker, and Harold J Isard. Low-dose mammography. *Radiology*, 109(2):323–326, 1973.

[114] Nobuyuki Otsu. A threshold selection method from gray-level histograms. *IEEE transactions on systems, man, and cybernetics*, 9(1):62–66, 1979.

[115] Amit M Oza and Norman F Boyd. Mammographic parenchymal patterns: a marker of breast cancer risk. *Epidemiologic reviews*, 15(1):196–208, 1993.

[116] Emanuel Parzen. On estimation of a probability density function and mode. *The annals of mathematical statistics*, 33(3):1065–1076, 1962.

[117] Prasanna Pathmanathan. *Predicting tumour location by simulating the deformation of the breast using nonlinear elasticity and the finite element method*. PhD thesis, University of Oxford, 2006.

[118] Gabriele Piantadosi, Mario Sansone, Roberta Fusco, and Carlo Sansone. Multi-planar 3d breast segmentation in mri via deep convolutional neural networks. *Artificial Intelligence in Medicine*, 103:101781, 2020.

[119] Snehal M Pinto Pereira, John H Hipwell, Valerie A McCormack, Christine Tanner, Sue M Moss, Louise S Wilkinson, Lisanne AL Khoo, Catriona Pagliari, Pippa L Skippage, Carole J Kliger, et al. Automated registration of diagnostic to prediagnostic x-ray mammograms: Evaluation and comparison to radiologists' accuracy. *Medical physics*, 37(9):4530–4539, 2010.

[120] María Nieves Plana, Carmen Carreira, Alfonso Muriel, Miguel Chiva, Víctor Abraira, Jose Ignacio Emparanza, Xavier Bonfill, and Javier Zamora. Magnetic resonance imaging in the preoperative assessment of patients with primary breast cancer: systematic review of diagnostic accuracy and meta-analysis. *European radiology*, 22(1):26–38, 2012.

[121] Josien PW Pluim, JB Antoine Maintz, and Max A Viergever. F-information measures in medical image registration. *IEEE transactions on medical imaging*, 23(12):1508–1516, 2004.

[122] Xavier Soria Poma, Edgar Riba, and Angel Sappa. Dense extreme inception network: Towards a robust cnn model for edge detection. In *The IEEE Winter Conference on Applications of Computer Vision*, pages 1923–1932, 2020.

[123] William H Press, Saul A Teukolsky, William T Vetterling, and Brian P Flannery. *Numerical recipes 3rd edition: The art of scientific computing*. Cambridge university press, 2007.

[124] Wang Qi, Ding Hui, and Wang Guang-zhi. A multistage processing procedure for 4d breast mri segmentation. In *2008 30th Annual International Conference of the IEEE Engineering in Medicine and Biology Society*, pages 3036–3039. IEEE, 2008.

[125] Yan Qiu, Xuejun Sun, Vasant Manohar, and Dmitry Goldgof. Towards registration of temporal mammograms by finite element simulation of mr breast volumes. In *Medical Imaging 2008: Visualization, Image-Guided Procedures, and Modeling*, volume 6918, page 69182F. International Society for Optics and Photonics, 2008.

[126] David Raba, Arnau Oliver, Joan Martí, Marta Peracaula, and Joan Espunya. Breast segmentation with pectoral muscle suppression on digital mammograms. In *Iberian conference on pattern recognition and image analysis*, pages 471–478. Springer, 2005.

[127] Vijay Rajagopal, Jae-Hoon Chung, Ralph P Highnam, Ruth Warren, Poul MF Nielsen, and Martyn P Nash. Mapping microcalcifications between 2d mammograms and 3d mri using a biomechanical model of the breast. In *Computational Biomechanics for Medicine*, pages 17–28. Springer, 2010.

[128] Andrik Rampun, Karen López-Linares, Philip J Morrow, Bryan W Scotney, Hui Wang, Inmaculada Garcia Ocaña, Grégory Maclair, Reyer Zwiggelaar, Miguel A González Ballester, and Iván Macía. Breast pectoral muscle segmentation in mammograms using a modified holistically-nested edge detection network. *Medical image analysis*, 57:1–17, 2019.

[129] Ravipudi V Rao, Vimal J Savsani, and DP Vakharia. Teaching–learning-based optimization: a novel method for constrained mechanical design optimization problems. *Computer-Aided Design*, 43(3):303–315, 2011.

[130] Mohammad Razavi, Lei Wang, Albert Gubern-Mérida, Tatyana Ivanovska, Hendrik Laue, Nico Karssemeijer, and Horst K Hahn. Towards accurate segmentation of fibroglandular tissue in breast mri using fuzzy c-means and skin-folds removal. In *International Conference on Image Analysis and Processing*, pages 528–536. Springer, 2015.

[131] Jose Rincon. Facilitating breast conserving surgery using preoperative mri. Master's thesis, University of Waterloo, 2018.

[132] David A Bluemke Rohlfing Torsten, Calvin R Maurer and Michael A Jacobs. Volume-preserving nonrigid registration of mr breast images using free-form deformation with an incompressibility constraint. *IEEE transactions on medical imaging*, 22(6):730–741, 2003.

[133] Olaf Ronneberger, Philipp Fischer, and Thomas Brox. U-net: Convolutional networks for biomedical image segmentation. In *International Conference on Medical image computing and computer-assisted intervention*, pages 234–241. Springer, 2015.

[134] Sebastian Ruder. An overview of gradient descent optimization algorithms. *arXiv preprint arXiv:1609.04747*, 2016.

[135] Leonid I Rudin, Stanley Osher, and Emad Fatemi. Nonlinear total variation based noise removal algorithms. *Physica D: nonlinear phenomena*, 60(1-4):259–268, 1992.

[136] Daniel Rueckert, Luke I Sonoda, Carmel Hayes, Derek LG Hill, Martin O Leach, and David J Hawkes. Nonrigid registration using free-form deformations: application to breast mr images. *IEEE transactions on medical imaging*, 18(8):712–721, 1999.

[137] Nicole V Ruiter, Rainer Stotzka, T-O Muller, Hartmut Gemmeke, Jürgen R Reichenbach, and Werner A Kaiser. Model-based registration of x-ray mammograms and mr images of the female breast. *IEEE Transactions on Nuclear Science*, 53(1):204–211, 2006.

[138] Amira Šerifović-Trbalić, Damir Demirović, Nasr Prljača, Gabor Szekely, and Philippe C Cattin. Intensity-based elastic registration incorporating anisotropic landmark errors and rotational information. *International journal of computer assisted radiology and surgery*, 4(5):463–468, 2009.

[139] Claude Elwood Shannon. A mathematical theory of communication. *Bell system technical journal*, 27(3):379–423, 1948.

[140] Connor Shorten and Taghi M Khoshgoftaar. A survey on image data augmentation for deep learning. *Journal of Big Data*, 6(1):60, 2019.

[141] Karen Simonyan and Andrew Zisserman. Very deep convolutional networks for large-scale image recognition. *arXiv preprint arXiv:1409.1556*, 2014.

[142] P Cotic Smole, Nicole V Ruiter, C Kaiser, J Krammer, and Torsten Hopp. Bundling 3d-and 2d-based registration of mri to x-ray breast tomosynthesis. In *Medical Imaging 2018: Image-Guided Procedures, Robotic Interventions, and Modeling*, volume 10576, page 105762X. International Society for Optics and Photonics, 2018.

[143] Hossein Soleimani, George Poothicottu Jacob, and Oleg V Michailovich. Fitting smooth manifolds to point clouds in a level set formulation. In *International Conference on Image Analysis and Recognition*, pages 139–149. Springer, 2019.

[144] Hossein Soleimani and MA Khosravifard. Reducing interpolation artifacts for mutual information based image registration. *Journal of medical signals and sensors*, 1(3):177, 2011.

[145] Hossein Soleimani and Mohammadali Khosravifard. Mutual information-based image template matching with small template size. In *2011 7th Iranian Conference on Machine Vision and Image Processing*, pages 1–5. IEEE, 2011.

[146] Hossein Soleimani and Oleg V Michailovich. Automatic breast tissue segmentation in mri scans. In *2020 IEEE International Conference on Systems, Man, and Cybernetics (SMC)*, pages 1572–1577. IEEE, 2020.

[147] Hossein Soleimani, Jose Rincon, and Oleg V Michailovich. Segmentation of breast mri scans in the presence of bias fields. In *International Conference on Image Analysis and Recognition*, pages 376–387. Springer, 2019.

[148] Juan Antonio Solves-Llorens, MJ Rupérez, C Monserrat, E Feliu, M García, and M Lloret. A complete software application for automatic registration of x-ray mammography and magnetic resonance images. *Medical physics*, 41(8Part1), 2014.

[149] Subashini Srinivasan, Brian A Hargreaves, and Bruce L Daniel. Fat-based registration of breast dynamic contrast enhanced water images. *Magnetic resonance in medicine*, 79(4):2408–2414, 2018.

[150] Colin Studholme, Derek LG Hill, and David J Hawkes. Multiresolution voxel similarity measures for mr-pet registration. In *Information processing in medical imaging*, volume 3, pages 287–298. Dordrecht, The Netherlands: Kluwer, 1995.

[151] Colin Studholme, Derek LG Hill, and David J Hawkes. An overlap invariant entropy measure of 3d medical image alignment. *Pattern recognition*, 32(1):71–86, 1999.

[152] P SUCKLING J. The mammographic image analysis society digital mammogram database. *Digital Mammo*, pages 375–386, 1994.

[153] Christine Tanner, Guido van Schie, Jan M Lesniak, Nico Karssemeijer, and Gábor Székely. Improved location features for linkage of regions across ipsilateral mammograms. *Medical image analysis*, 17(8):1265–1272, 2013.

[154] Snekha Thakran, Subhajit Chatterjee, Meenakshi Singhal, Rakesh Kumar Gupta, and Anup Singh. Automatic outer and inner breast tissue segmentation using multiparametric mri images of breast tumor patients. *PloS one*, 13(1):e0190348, 2018.

[155] Philippe Thevenaz and Michael Unser. Optimization of mutual information for multiresolution image registration. *IEEE transactions on image processing*, 9(12):2083–2099, 2000.

[156] Philippe Thevenaz and Michael A Unser. Spline pyramids for intermodal image registration using mutual information. In *Wavelet Applications in Signal and Image Processing V*, volume 3169, pages 236–247. International Society for Optics and Photonics, 1997.

[157] Saskia van Engeland, Peter Snoeren, JHCL Hendriks, and Nico Karssemeijer. A comparison of methods for mammogram registration. *IEEE Transactions on Medical Imaging*, 22(11):1436–1444, 2003.

[158] Saskia van Engeland, Peter R Snoeren, Henkjan Huisman, Carla Boetes, and Nico Karssemeijer. Volumetric breast density estimation from full-field digital mammograms. *IEEE transactions on medical imaging*, 25(3):273–282, 2006.

[159] Marina Velikova, Peter JF Lucas, Maurice Samulski, and Nico Karssemeijer. A probabilistic framework for image information fusion with an application to mammographic analysis. *Medical Image Analysis*, 16(4):865–875, 2012.

[160] Tom Vercauteren, Xavier Pennec, Aymeric Perchant, and Nicholas Ayache. Diffeomorphic demons: Efficient non-parametric image registration. *NeuroImage*, 45(1):S61–S72, 2009.

[161] PS Vikhe and VR Thool. Detection and segmentation of pectoral muscle on mlo-view mammogram using enhancement filter. *Journal of medical systems*, 41(12):190, 2017.

[162] Paul Viola and William M Wells III. Alignment by maximization of mutual information. *International journal of computer vision*, 24(2):137–154, 1997.

[163] Christian Wachinger and Nassir Navab. Simultaneous registration of multiple images: Similarity metrics and efficient optimization. *IEEE transactions on pattern analysis and machine intelligence*, 35(5):1221–1233, 2012.

[164] Lei Wang, Konstantinos Filippatos, Ola Friman, and Horst K Hahn. Fully automated segmentation of the pectoralis muscle boundary in breast mr images. In *Medical Imaging 2011: Computer-Aided Diagnosis*, volume 7963, page 796309. International Society for Optics and Photonics, 2011.

[165] Noel Weidner. Current pathologic methods for measuring intratumoral microvessel density within breast carcinoma and other solid tumors. *Breast cancer research and treatment*, 36(2):169–180, 1995.

[166] Douglas E Wood. National comprehensive cancer network (nccn) clinical practice guidelines for lung cancer screening. *Thoracic surgery clinics*, 25(2):185–197, 2015.

[167] Chen Xiaohua, Michael Brady, Jonathan Lok-Chuen Lo, and Niall Moore. Simultaneous segmentation and registration of contrast-enhanced breast mri. In *Biennial*

*International Conference on Information Processing in Medical Imaging*, pages 126–137. Springer, 2005.

[168] Saining Xie and Zhuowen Tu. Holistically-nested edge detection. In *Proceedings of the IEEE international conference on computer vision*, pages 1395–1403, 2015.

[169] Sheng-Chih Yang, Hsian-He Hsu, Giu-Cheng Hsu, Pau-Choo Chung, Shu-Mei Guo, Chien-Shen Lo, Ching-Wen Yang, San-Kan Lee, and Chein-I Chang. 3d localization of clustered microcalcifications using cranio-caudal and medio-lateral oblique views. *Computerized Medical Imaging and Graphics*, 29(7):521–532, 2005.

[170] Bonnie C Yankaskas, Ryan C May, Jeanine Matuszewski, J Michael Bowling, Molly P Jarman, and Bruce F Schroeder. Effect of observing change from comparison mammograms on performance of screening mammography in a large community-based population. *Radiology*, 261(3):762–770, 2011.

[171] Jianhua Yao, Jo Anne Zujewski, Jennifer Orzano, Sheila Prindiville, and Catherine Chow. Classification and calculation of breast fibroglandular tissue volume on spgr fat suppressed mri. In *Medical Imaging 2005: Image Processing*, volume 5747, pages 1942–1949. International Society for Optics and Photonics, 2005.

[172] Kaiming Yin, Shiju Yan, Chengli Song, and Bin Zheng. A robust method for segmenting pectoral muscle in mediolateral oblique (mlo) mammograms. *International journal of computer assisted radiology and surgery*, 14(2):237–248, 2019.

[173] Woong Bae Yoon, Ji Eun Oh, Eun Young Chae, Hak Hee Kim, Soo Yeul Lee, and Kwang Gi Kim. Automatic detection of pectoral muscle region for computer-aided diagnosis using mias mammograms. *BioMed research international*, 2016, 2016.

[174] Xiahai Zhuang, Simon Arridge, David J Hawkes, and Sebastien Ourselin. A nonrigid registration framework using spatially encoded mutual information and free-form deformations. *IEEE transactions on medical imaging*, 30(10):1819–1828, 2011.

[175] Xiahai Zhuang, David J Hawkes, and Sebastien Ourselin. Spatial information encoded mutual information for nonrigid registration. In *International Workshop on Biomedical Image Registration*, pages 246–257. Springer, 2010.

[176] Barbara Zitova and Jan Flusser. Image registration methods: a survey. *Image and vision computing*, 21(11):977–1000, 2003.

# APPENDICES

# Appendix A

# Pectoralis Segmentation in MLO Mammograms

This section provides the details of proposed method toward the detecting the boundary between the breast tissue and pectoralis major (Section 3.2).

## A.1 Training the Network

Assuming $W$ as the array of network parameters, the objective function used for training the proposed CNN can then be expressed as

$$\mathfrak{L}(W) = \mathfrak{L}_1(X^1, W) + \mathfrak{L}_2(X^2, W) \tag{A.1}$$

where $X^1$ and $X^2$ are the activation values (feature maps) produced by stages 2 and 4 of the network. In this formulation, $\mathfrak{L}_1(X^1, W)$ and $\mathfrak{L}_2(X^2, W)$ represent the lost functions of the two stages, respectively. Each lost function is computed over all pixels of a training image and its reference edge map $Y$. The latter has the form of a binary mask which assumes the value of one at the location of the true boundary, while being equal to zero for other pixels, i.e., $Y_i \in \{0, 1\}$, $i = 1, 2, \ldots, |Y|$. For obvious reasons, the majority of these labels always correspond to non-contour pixels, which introduces a considerable bias towards the "out-of-boundary" pixels. To compensate for this undesirable effect, the loss for each pixel $X_i$ in activation $X$ with respect to its label $Y_i$ is computed as

$$l(x_i) = \begin{cases} \alpha \cdot \log(1 - \mathrm{sgm}(x_i)) & \text{if } y_i = 0 \\ \beta \cdot \log(\mathrm{sgm}(x_i)) & \text{if } y_i = 1 \end{cases} \tag{A.2}$$

where sgm stands for the standard sigmoid function, and

$$\alpha = \lambda \frac{|Y^+|}{|Y^+| + |Y^-|} \ , \ \beta = \frac{|Y^-|}{|Y^+| + |Y^-|}, \tag{A.3}$$

with $\lambda$ being a positive tuning parameter used to balance the discrepancy in the number of "out-of-boundary" pixels ($|Y^-|$) and "on-boundary" pixels ($|Y^+|$).

The availability of three different datasets has allowed us to employ a "2 + 1" validation strategy, in which two datasets (e.g., InBreast and CBIS-DDSM) were used fo the purpose of network training, followed by predicting the labels of the the third "unseen" dataset (e.g., MIAS). Note that, in addition to fair assessment of validation errors, the above strategy has an important advantage of providing a useful insight into the effects of between-scanner variability. To minimize the effects of overfitting, the experimental dataset was extended by means of data augmentation, which is a standard practice in DL [140]. To this end, each training image was resized by factors 0.9 and 1.1, followed by either cropping or zero-padding of the results thus obtained to the target size of $256 \times 256$ pixels. Additional training images were obtained from the original mammograms through the process of vertical, horizontal, and diagonal flipping. In this way, the size of the training set was increased by a factor of 10.

To initiate training, we used the VGG16 weights optimized over the ImageNet dataset [28]. The learning rate and the batch size were set to 0.0001 and 2, respectively. The training was performed by means of stochastic gradient descent optimization [134], with the number of epochs set to 30.

## A.2 Locating the Pectoralis Boundary as the Shortest Path Between Two Nodes of the Graph

The connectivity structure of the computed graph $\mathcal{G}$ (Section 3.2.1) can be alternatively defined in terms of its associated matrix of (edge) weights $\mathcal{W}$, which quantifies a degree of affinity between any two nodes of the graph. In this case, lower values of $\mathcal{W}$ indicate "stronger" connections, with $\mathcal{W}(\mathbf{p}, \mathbf{q}) = \infty$ representing the situation when nodes $\mathbf{p}$ and $\mathbf{q}$ are considered to be disconnected.

To facilitate the definition of $\mathcal{W}$, we associate the nodes $\mathcal{V}$ of $\mathcal{G}$ with *all* the pixels within the image domain, in which case $\mathcal{V}$ becomes a uniform rectangular lattice. For each $\mathbf{p} \in \mathcal{V}$, let $\mathcal{N}(\mathbf{p})$ denotes its 8-connected neighbourhood and, with a slight abuse of notations, let

the modified binary mask $B$ embody the subset of $\mathcal{V}$ over which its values are equal to 1 (see Subplots A5 and B5 of Figure 3.8). Then, for each $\mathbf{p} \in \mathcal{V}$, the $(\mathbf{p}, \mathbf{q})$-th element $\mathcal{W}$ can be defined as

$$\mathcal{W}(\mathbf{p}, \mathbf{q}) = \begin{cases} \frac{2}{M(\mathbf{p})+M(\mathbf{q})}, & \text{if } \mathbf{q} \in \mathcal{N}(\mathbf{p}) \cap B \\ \infty, & \text{otherwise} \end{cases}, \tag{A.4}$$

where $\cap$ stands for set intersection. The above definition of edge weights is based on the values of edge probability map $M$. It is worthwhile noting that $M$ "inherits" the best characteristics of both OUT 1 and OUT 2. In particular, similarly to OUT 1, the non-trivial values of $M$ are localized in close proximity of the true pectoral boundary. At the same time, similarly to OUT 2, $M$ remains immune to the effects of clutter noise. Thus, for any $\mathbf{p} \in B$ and $\mathbf{q} \in \mathcal{N}(\mathbf{p}) \cap B$, the value of $W(\mathbf{p}, \mathbf{q})$ is bound to decrease *pro rata* with an increase in the empirical probability of nodes $\mathbf{p}$ and $\mathbf{q}$ to lie near the true pectoral boundary. It is, therefore, not unreasonable to assume the latter to be associated with an *open path* on $\mathcal{G}$ formed by its most "connected" nodes. More specifically, given two points $S$ (for "start") and $E$ (for "end") on the opposite sides of pectoralis, its boundary can be closely approximated by the *shortest path* on $\mathcal{G}$ that connects $S$ and $E$.

Computation of shortest paths over weighted graphs is a well-studied problem which, in practical scenarios, is usually implemented by means of Dijkstra's algorithm or one of its many variations [26]. We used a modified version of Dijkstra's algorithm which is represented by the pseudocode in Figure A.1.

At its input, the algorithm in Figure A.1 receives the nodes $\mathcal{V}$, binary map $B$ as well as points $S$ and $E$, while returning a set of nodes $\mathcal{P}$ which form the shortest path on $\mathcal{G}$. To simplify the notations, the pseudocode uses two "hash functions", dist and parent. For any $\mathbf{p} \in \mathcal{V}$, the functions either set or get its distance to the source node $S$ (using dist) and its respective parent (using parent). In particular, during initialization, the distance from $S$ to itself is set to zero (line 2), while the distances to all other nodes are set to infinity (line 3). The parental relations between the nodes, at the same time, are assume to be undefined (line 4).

While the algorithm in Figure A.1 follows the principal structure of Dijkstra's procedure, it incorporates a few important modifications intended to maximize its numerical efficiency. In particular, the update of nodal distances to the source (lines 9-16) as well as establishing the parental relations (lines 19-25) are carried out over the 8-connected neighbourhood of each queried node $\mathbf{q}$, while excluding those elements of $\mathcal{N}$ which lie outside $B$ (lines 10 and 19). As a result, the updates involves only the nodes (pixels) which are located in a close proximity of pectoralis, which substantially speeds up the computation of $\mathcal{P}$. Moreover, the updates are terminated once the end node $E$ is reached, at which point

```
1: procedure DIJKSTRA(𝒱, B, S, E)
2:     dist(S) ← 0
3:     dist(p) ← ∞, ∀p ∈ 𝒱\{S}
4:     parent(p) ← NIL, ∀p ∈ 𝒱
5:     𝒜 ← {S}
6:     u ← S
7:     while u ≠ E do
8:         ℬ = ∅
9:         for p ∈ 𝒜 do
10:            for q ∈ (𝒩{p} ∩ B)\𝒜 do
11:                if dist(q) > dist(p) + 𝒲(q, p) then
12:                    dist(q) ← dist(p) + 𝒲(q, p)
13:                    ℬ ← ℬ ∪ {q}
14:                end if
15:            end for
16:        end for
17:        u = arg min_{q∈ℬ} dist(q)
18:        𝒜 ← 𝒜 ∪ {u}
19:        for q ∈ (𝒩{u} ∩ B) do
20:            if dist(q) > dist(u) + 𝒲(q, u) then
21:                dist(q) ← dist(u) + 𝒲(q, u)
22:                parent(q) ← u
23:            end if
24:        end for
25:    end while
26:    𝒫 ← {E}
27:    p ← E
28:    while p ≠ S do
29:        p = parent(p)
30:        𝒫 ← 𝒫 ∪ {p}
31:    end while
32: return 𝒫
33: end procedure
```

Figure A.1: Modified Dijkstra's algorithm with backtracking

the algorithm proceeds to recovering the shortest path $\mathcal{P}$ via backtracking the parental

```
1: procedure BOUNDARY(OUT1, OUT2)
2:     Compute B from OUT2 via thresholding
3:     if B is disconnected then
4:         Complete B via linear extrapolation
5:     end if
6:     Compute M = B ⊙ OUT 1
7:     Construct G; define S and E.
8:     Compute P = DIJKSTRA(V, B, S, E)
9: return P
10: end procedure
```

Figure A.2: Pectoral boundary reconstruction

dependencies stored by parent (lines 28-31 of Figure A.1).

Our experiments revealed that the binary mask $B$ computed from OUT 2 is connected in more than 90% of the cases, and as a results, it does not need to be extrapolated. Subplots A7 and B7 of Figure 3.8 depict the pectoral boundaries recovered by means of the proposed method for the input MLO mammograms shown in Subplots A1 and B1 of the same figure, respectively. In this case, $S$ and $E$ have been identified with the end points of the morphological skeleton of $B$, which has been observed to provide simple and stable initialization throughout all our experiments. All the principal algorithmic steps involved in the above estimation process are summarized in Figure A.2.

## A.3 More Experimental Results on Pectorlais Boundary Detection in Mammograms

Unfortunately, direct comparison of the proposed method with available alternative approaches is problematic due to the lack of standardized ground truth segmentation. With this proviso in mind, Table A.1 summarizes the performance metrics obtained using a recent method for breast segmentation proposed by Rampun *et al* [128]. Comparing these results with those in Table 3.3, one can see that the proposed method outperforms the reference one in most of the cases. Not less important is the fact that the proposed algorithm yields considerably smaller values of the standard deviations, which suggests that it is capable of providing more consistent estimation.

Additional comparative results are shown in Table A.2. In particular, the table sum-

Table A.1: Comparison results for three database by Rampun *et al* [128]. All metrics are presented in % by their mean value ± one standard deviation.

| Metric | MIAS | CBIS-DDSM | InBreast |
|---|---|---|---|
| DSC | 97.5±7.5 | 98.1 ± 7.1 | 95.60 ± 8.4 |
| JAC | 94.6±9.8 | 95.1 ± 9.4 | 92.6 ± 10.6 |
| SPE | 99.5 ±1.2 | 99.6 ±1.4 | 99.8 ±1.8 |
| SEN | 98.2±7.6 | 98.3 ± 7.6 | 95.2 ± 8.6 |
| ACC | 99.3 ±1.4 | 99.5±1.3 | 99.6±2.2 |
| FPR | 0.6 ± 1.8 | 0.4 ± 0.6 | 0.3 ± 2.1 |
| FNR | 3.2 ± 2.9 | 3.8 ± 2.5 | 5.7 ± 6.5 |

Table A.2: FPR and FNR (in %) of reference algorithms for the MIAS dataset.

| Method | Dataset | FPR | FNR |
|---|---|---|---|
| Ours | MIAS(all) | 0.16 | 2.23 |
| Rampun et al. [128] | MIAS | 0.6 | 3.2 |
| Vikhe and Thool [161] | miniMIAS | 0.93 | 5.7 |
| Chen et al. [21] | miniMIAS | 1.02 | 5.63 |
| Yoon et al. [173] | miniMIAS | 4.51 | 5.68 |
| Bora et al. [13] | miniMIAS | 1.56 | 2.83 |
| Ferrai et al. [34] | miniMIAS | 0.58 | 5.77 |
| Camilus et al. [20] | MIAS | 0.64 | 5.58 |
| U-net [133] | MIAS | 7.1 | 12.2 |

marizes the values of FPR and FNR produced by a number of existing approaches applied to the MIAS dataset as well as to the miniMIAS dataset (which is identical to MIAS aside for the size of data images that have a dimension of $1024 \times 1024$ pixels). Note that we retrained the U-net [133] by our own annotated data and computed its performance on MIAS dataset. Once again, the results indicate that the proposed method results in more accurate reconstruction in terms of FPR and FNR (which are equal to 0.16% and 2.23%, respectively, for the MIAS dataset).

As mentioned earlier, thresholding OUT2 occasionally produces a binary mask with a fragmented longest connected component (about 10% of all cases), as exemplified in Subplot B4 of Figure 3.8. In such cases, the masks have been extended via linear extrapolation, the accuracy of which, in turn, depends on the extent of the initial mask. One of the worst-case scenarios is shown in Figure A.3 which depicts an input mammogram

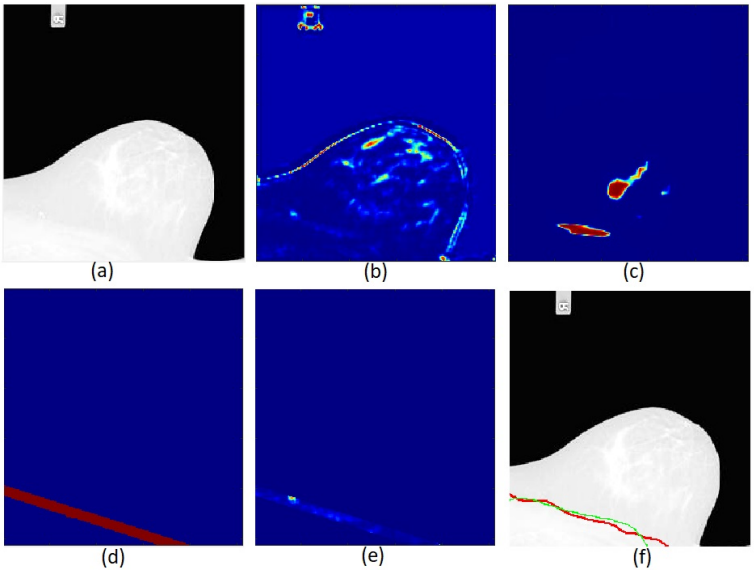


Figure A.3: Detection of pectoral boundary in a low-contrast mammogram: (a) Input image; (b) OUT 1; (c) OUT 2; (d) Modified binary mask $B$; (e) Final edge probability map $M$; and (f) Detected boundary (red) and the ground truth (green).

(Subplot (a)) along with its related OUT1 (Subplot (b)) and OUT2 (Subplot (c)). One can see that, in this case, the longest connected component of binarized OUT2 is markedly shorter than the true pectoral boundary, being disconnected both on its left and right. It would therefore be reasonable to expect that the linearly extrapolated mask $B$ (Subplot (d)) and the final edge probability map $M$ (Subplot (e)) might provide inadequate initialization for the Dijkstra procedure in Figure A.1 . However, despite the problematic data, the final result of reconstruction of the pectoral boundary shown in Subplot (f) of Figure A.3 (red curve) appears to be in a good agreement with the ground truth (green curve), with DSC=93.85 % and JAC=88.42%. Thus, even though the resulting metrics are objectively lower in comparison to their mean values in Table 3.3, the proposed algorithm is still capable of producing meaningful and useful results.

# Appendix B

# Numerical Solution for Two-class Segmentation Model

While much more tractable compared with its original version, the optimization problem (3.8) can still benefit further simplifications. One can first split the (optimization) variables to yield an equivalent problem of the form

$$\min_{\xi,\mu_d,\mu_f,c} \Big\{ \lambda_d \sum_{\mathbf{r}\in\Omega} \xi(\mathbf{r})|g(\mathbf{r}) - \mu_d - \Phi(\mathbf{r})c|^2 + \lambda_f \sum_{\mathbf{r}\in\Omega} (1-\xi(\mathbf{r}))|g(\mathbf{r}) - \mu_f - \Phi(\mathbf{r})c|^2 + \\ + \|\eta\|_{\mathrm{TV}} + I_{[0,1]}(\xi) \Big\}, \quad \text{s.t. } \xi = \eta. \tag{B.1}$$

In this case, the augmented Lagrangian of the new problem can be defined as

$$\mathcal{L}(\xi,\eta,\mu_d,\mu_f,c,y) = \\ = \lambda_d \sum_{\mathbf{r}\in\Omega} \xi(\mathbf{r})|g(\mathbf{r}) - \mu_d - \Phi(\mathbf{r})c|^2 + \lambda_f \sum_{\mathbf{r}\in\Omega} (1-\xi(\mathbf{r}))|g(\mathbf{r}) - \mu_f - \Phi(\mathbf{r})c|^2 + \\ + \|\eta\|_{\mathrm{TV}} + I_{[0,1]}(\xi) + \frac{\delta}{2} \sum_{\mathbf{r}\in\Omega} |\xi(\mathbf{r}) - \eta(\mathbf{r}) + y(\mathbf{r})|^2, \tag{B.2}$$

where $y$ denotes a scaled version of the vector of Lagrange multipliers and $\delta > 0$ is a smoothing parameter (e.g., $\delta = 0.5$).

At this point, one can use the Alternating Directions Method of Multipliers (ADMM) [15] to minimize $\mathcal{L}(\xi,\eta,\mu_d,\mu_f,c,y)$ with respect to the primal variables (i.e., w.r.t. $\xi$, $\eta$, $\mu_d$, $\mu_f$, and $c$) *iteratively* using the following steps.

- Step 1: $\xi^{t+1} = \arg\min_{\xi} \mathcal{L}(\xi, \eta^t, \mu_d^t, \mu_f^t, c^t, y^t)$
- Step 2: $\eta^{t+1} = \arg\min_{\eta} \mathcal{L}(\xi^{t+1}, \eta, \mu_d^t, \mu_f^t, c^t, y^t)$
- Step 3: $(\mu_d^{t+1}, \mu_f^{t+1}, c^{t+1}) = \arg\min_{\mu_d, \mu_f, c} \mathcal{L}(\xi^{t+1}, \eta^{t+1}, \mu_d, \mu_f, c, y^t)$

Once the primary variables have been updated, the dual variable $y$ is updated according to

$$y^{t+1}(\mathbf{r}) = y^t(\mathbf{r}) + \xi^{t+1}(\mathbf{r}) - \eta^{t+1}(\mathbf{r}), \quad \forall \mathbf{r} \in \Omega.$$

Although the number of update steps above could look prohibitively large at the first glance, they all admit either closed-form or efficiently solutions, which considerably reduces the cost of each ADMM iteration. Specifically, the updates can be performed as follows.

**Solution to Step 1:**

The update in $\xi$ requires solving a simple quadratic minimization problem, followed by orthogonally projecting its solution onto the interval $[0, 1]$. Moreover, the update can be performed separately at each $\mathbf{r}$ according to

$$\xi(\mathbf{r})^{t+1} = \Pi_{[0,1]}\left\{\eta^t(\mathbf{r}) - y^t(\mathbf{r}) + \frac{\lambda_f - \lambda_d}{\delta}\Big(g(\mathbf{r}) - (\mu_f^t - \mu_d^t) - \Phi(\mathbf{r})c^t\Big)\right\},$$

where $\Pi_{[0,1]}(z) = \max\{\min\{z, 1\}, 0\}$ denotes the operator of orthogonal projection onto $[0, 1]$.

**Solution to Step 2:**

The update in $\eta$ requires solving a norm minimization problem of the form

$$\eta^{t+1} = \arg\min_{\eta}\left\{\frac{1}{2}\sum_{\mathbf{r}\in\Omega}|\eta(\mathbf{r}) - (\xi^{t+1}(\mathbf{r}) + y^t(\mathbf{r}))|^2 + \frac{1}{\delta}\|\eta\|_{\mathrm{TV}}\right\}.$$

This problem has the format of well-known *TV de-noising* [135], which can be efficiently solved by a number of numerical methods. In this work, to solve this problem, the fixed-point algorithm of [22] has been used.

**Solution to Steps 3:**

To derive an equation for the update of $\mu_d$, $\mu_f$ and $c$, it is convenient to think of $\Phi(\mathbf{r})$ as an $N \times M$ matrix, with $N$ equal to the number of voxels in $\Omega$ and $M = (K+1)^3$ being the total number of polynomial coefficients used for representation of $b$. In an analogous manner, both $g$ and $\xi^{t+1}$ can be also thought of as column vectors of length $N$, with a similar interpretation of $c$ as a length $M$ (column) vector.

Using the notational simplifications above, let $\theta \in \mathbb{R}^{M+2}$ be a new vector obtained via concatenation of $\mu_d$, $\mu_f$ and $c$, namely $\theta = [\mu_d, \mu_f, c^T]^T$. Also, let $A_d$ and $A_f$ be two $N \times (M+2)$ matrices obtained by augmenting $\Phi$ with a zero $\mathbf{0}$ and a unit $\mathbf{1}$ column as $A_d = [\mathbf{1}\,\mathbf{0}\,\Phi]$ and $A_f = [\mathbf{0}\,\mathbf{1}\,\Phi]$, respectively. Finally, let $W_d$ and $W_f$ be two diagonal matrices defined by vectors $\lambda_d \xi^{t+1}$ and $\lambda_d (1 - \xi^{t+1})$, correspondingly, as well. Then, with

$$B = A_d^T W_d A_d + A_f^T W_f A_f \quad \text{and} \quad \beta = (A_d^T W_d + A_f^T W_f) g,$$

the optimal value of $\theta$ can be shown to be a solution to the linearly constrained quadratic program given by

$$\arg\min_{\theta} \; \theta^T B \theta - 2\beta^T \theta, \quad \text{s.t. } e^T \theta = 0, \tag{B.3}$$

with $e \in \mathbb{R}^{M+2}$ of the form $e = [1, 1, 0, 0, \ldots, 0]^T$. Note that the constraint $\nu^T \theta = 0$ is added to guarantee the attainment of a solution with $\mu_d \neq \mu_f$, thus enforcing the photometric discrepancy between the dense and fat tissues.

When applied to the constrained problem in (B.3), the Karush-Kuhn-Tucker optimality conditions result in a system of linear equations in the primal optimal $\theta^*$ and the dual optimal $\nu^*$ variables that is given by [14]

$$\begin{bmatrix} B & e \\ e^T & 0 \end{bmatrix} \begin{bmatrix} \theta^* \\ \nu^* \end{bmatrix} = \begin{bmatrix} \beta \\ 0 \end{bmatrix}. \tag{B.4}$$

The above system of equation is straightforward to solve to find $\theta^*$, from which the values of $\mu_d^{t+1}$, $\mu_f^{t+1}$, and $c^{t+1}$ can be extracted.

In a series of both computer simulations and experiments with real-life breast MRI data, the proposed algorithm has demonstrated stable and consistent convergence in less than 20 iterations, using $\lambda_d = \lambda_f = 0.1$ and $\delta = 0.5$. Once the optimal $\xi^*$ was computed, its corresponding domain partition/segmentation was defined as

$$\Omega_d = \{\mathbf{r} \in \Omega \mid \xi^*(\mathbf{r}) \geq 0.5\} \quad \text{and} \quad \Omega_f = \{\mathbf{r} \in \Omega \mid \xi^*(\mathbf{r}) < 0.5\}.$$

# Appendix C

# Publications During Ph.D. Studies

1. H. Soleimani and O. V. Michailovich, "A novel approach to contrast transfer between breast MRI and X-ray mammography." Medical Image Analysis, under review (first revision).

2. H. Soleimani and O. V. Michailovich, "On Segmentation of Pectoral Muscle in Digital Mammograms by means of Deep Learning." IEEE Access (2020).

3. H. Soleimani and O. V. Michailovich, "2D X-Ray Mammogram and 3D Breast MRI Registration." In International Conference on MICCAI, pp. 150-159. Springer, Cham, 2020.

4. H. Soleimani and O. V. Michailovich, "Automatic Breast Tissue Segmentation in MRI Scans," 2020 IEEE International Conference on Systems, Man, and Cybernetics (SMC), Toronto, ON, Canada.

5. H. Soleimani, J. Rincon, and O. V. Michailovich, " Segmentation of Breast MRI Scans in the Presence of Bias Fields." In International Conference on Image Analysis and Recognition, pp. 376-387. Springer, Cham, 2019.

6. H. Soleimani, G. P. Jacob and O. V. Michailovich, " Fitting Smooth Manifolds to Point Clouds in a Level Set Formulation." In International Conference on Image Analysis and Recognition, pp. 139-149. Springer, Cham, 2019.